

AD-A149 283

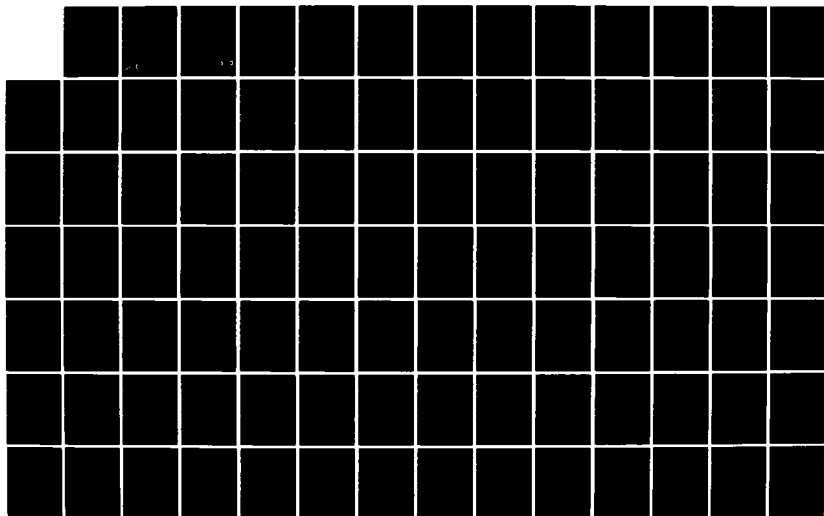
LARGE EDDY SIMULATION OF TURBULENT FLOW IN CHANNELS  
WITH WAVY WALLS INCLU. (U) NIELSEN ENGINEERING AND  
RESEARCH INC MOUNTAIN VIEW CA G D KUHN ET AL JUL 84  
NEAR-TR-325 N00014-81-C-0506

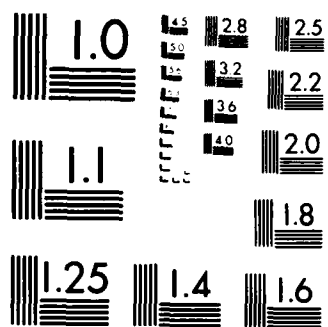
1/2

UNCLASSIFIED

F/G 20/4

NL





MICROCOPY RESOLUTION TEST CHART  
NATIONAL BUREAU OF STANDARDS 1963-A

12

LARGE EDDY SIMULATION OF TURBULENT FLOW  
IN CHANNELS WITH WAVY WALLS  
INCLUDING BOTH COMPLIANT WALLS  
AND WALLS WITH PRESCRIBED MOTION

by

G.D. Kuhn, J.H. Ferziger, P. Moin, and J. Kim

AD A 149203

DTIC FILE COPY

DTIC  
ELECTE  
JAN 14 1985  
S B

DISTRIBUTION STATEMENT A  
Approved for public release;  
Distribution Unlimited

EAR

NIELSEN ENGINEERING  
AND RESEARCH, INC.

OFFICES: 510 CLYDE AVENUE / MOUNTAIN VIEW, CALIFORNIA 94043 / TELEPHONE (415) 968-9457

NOT TO BE RELEASED TO THE PUBLIC

COPY NO. \_\_\_\_\_

LARGE EDDY SIMULATION OF TURBULENT FLOW  
IN CHANNELS WITH WAVY WALLS  
INCLUDING BOTH COMPLIANT WALLS  
AND WALLS WITH PRESCRIBED MOTION

by

G.D. Kuhn, J.H. Ferziger, P. Moin, and J. Kim

NEAR TR 325  
July 1984

Prepared Under Contract No. N00014-81-C-0506

For

OFFICE OF NAVAL RESEARCH  
Arlington, Virginia 22217

by

NIELSEN ENGINEERING & RESEARCH, INC.  
510 Clyde Avenue, Mountain View, CA 94040  
Telephone (415) 968-9457

DTIC  
ELECTE  
JAN 14 1985  
S D B

**DISTRIBUTION STATEMENT A**

Approved for public release  
Distribution Unlimited

REPORT DOCUMENTATION PAGE		READ INSTRUCTIONS BEFORE COMPLETING FORM
1. REPORT NUMBER	2. GOVT ACCESSION NO.	3. RECIPIENT'S CATALOG NUMBER
4. TITLE (and Subtitle) LARGE EDDY SIMULATION OF TURBULENT FLOW IN CHANNELS WITH WAVY WALLS INCLUDING BOTH COMPLIANT WALLS AND WALLS WITH PRESCRIBED MOTION		5. TYPE OF REPORT & PERIOD COVERED FINAL REPORT
7. AUTHOR(s) G.D. Kuhn, J.H. Ferziger, P. Moin, and J. Kim		6. PERFORMING ORG. REPORT NUMBER NEAR TR 325
9. PERFORMING ORGANIZATION NAME AND ADDRESS Nielsen Engineering & Research, Inc. 510 Clyde Avenue Mountain View, CA 94043		8. CONTRACT OR GRANT NUMBER(s) N00014-81-C-0506
11. CONTROLLING OFFICE NAME AND ADDRESS Office of Naval Research Arlington, VA 22217		10. PROGRAM ELEMENT, PROJECT, TASK AREA & WORK UNIT NUMBERS
14. MONITORING AGENCY NAME & ADDRESS (if different from Controlling Office)		12. REPORT DATE July 1984
		13. NUMBER OF PAGES 126
		15. SECURITY CLASS. (of this report) Unclassified
		15a. DECLASSIFICATION/DOWNGRADING SCHEDULE
16. DISTRIBUTION STATEMENT (of this Report)  Approved for public release. Distribution unlimited		
17. DISTRIBUTION STATEMENT (of the abstract entered in Block 20, if different from Report)		
18. SUPPLEMENTARY NOTES		
19. KEY WORDS (Continue on reverse side if necessary and identify by block number)  Large Eddy Simulation, Compliant Walls, Wavy Walls		
20. ABSTRACT (Continue on reverse side if necessary and identify by block number)  The effects of prescribed wall motion on turbulent channel flow were examined with the objective of understanding the drag mechanisms and obtaining a possible means for drag reduction. A computer program for large-eddy simulation (LES) of turbulent flow in a channel was modified to treat the case of time-varying wall motion using linearized boundary conditions. The code was applied to flow in a channel with prescribed wall motion on one wall. It was		

Unclassified

SECURITY CLASSIFICATION OF THIS PAGE(When Data Entered)

found that the results can be qualitatively explained by a model based on a Stokes-like layer near the moving wall. This provides a theory which can be used to guide the selection of parameters. Considering both viscous and pressure drag components, it was found that drag reduction is possible under certain conditions of wall motion. However, work is required to drive the wall motion to produce this effect and the effort expended can be a considerable fraction of the reduced through-flow energy requirements. The major effects of the wall motion are restricted to the viscous sublayer of the turbulent flow.

Unclassified

SECURITY CLASSIFICATION OF THIS PAGE(When Data Entered)

# ABSTRACT

The effects of prescribed wall motion on turbulent channel flow were examined with the objective of understanding the drag mechanisms and obtaining a possible means for drag reduction. A computer program for large-eddy simulation (LES) of turbulent flow in a channel was modified to treat the case of time-varying wall motion using linearized boundary conditions. The code was applied to flow in a channel with prescribed wall motion on one wall. It was found that the results can be qualitatively explained by a model based on a Stokes-like layer near the moving wall. This provides a theory which can be used to guide the selection of parameters. Considering both viscous and pressure drag components, it was found that drag reduction is possible under certain conditions of wall motion. However, work is required to drive the wall motion to produce this effect and the effort expended can be a considerable fraction of the reduced through-flow energy requirements. The major effects of the wall motion are restricted to the viscous sublayer of the turbulent flow.



DTIC TAB		<input checked="checked" type="checkbox"/>
Unannounced		<input type="checkbox"/>
Justification		
By <b>PER CALL JC</b>		
Distribution/		
Availability Codes		
Dist	Avail and/or	Special
<b>A-1</b>		

## CONTENTS

NOMENCLATURE .....	IV.
1. INTRODUCTION .....	1
2. BOUNDARY CONDITIONS FOR FLEXIBLE MOVING WALLS.....	3
2.1 Approximations.....	3
2.2 Parameters.....	7
3. ANALYTICAL STUDIES.....	9
3.1 The Linearized Stokes Layer Solution.....	10
3.2 Numerical Solutions for Nonlinear Stokes Layer....	14
3.3 Estimate of Effect of Stokes Layer on Mean Pressure Gradient.....	16
3.3.1 Mixing Length Analysis.....	16
3.3.2 Momentum Balance.....	19
3.3.3 Results.....	20
3.4 Energy Balance.....	22
3.5 Extension to Compliant Walls.....	26
3.6 Pressure Drag.....	28
4. COMPLIANT WALL DYNAMICS.....	29
5. LARGE-EDDY SIMULATION.....	35
5.1 LES Results for Prescribed Wall Motion.....	37
5.1.1 Effect of Wall Motion on Pressure Gradient.....	38
5.1.2 Effect of Wall Motion on Turbulence.....	39
5.1.3 Energy Balance.....	43
5.1.4 Pressure Drag.....	44



## CONTENTS (Concluded)

5.2	LES Results for Compliant Wall Motion.....	45
5.2.1	Effects of Turbulence on Wall Motion.....	45
5.2.2	Wall Motion Effects on Turbulence.....	53
5.3	LES Results for Other Types of Wall Conditions.....	55
5.3.1	"Smart Wall" Experiments.....	55
5.3.2	Distributed Suction/Blowing.....	55
5.3.3	Longitudinal Grooves.....	56
6.	LES IN GENERALIZED COORDINATES.....	57
6.1	Governing Equations.....	58
6.2	Boundary Conditions.....	59
6.3	Coordinate Transformation.....	59
6.4	Filtering.....	62
6.5	Generalized Equations.....	63
6.6	Discretization of the Generalized Equations.....	69
6.6.1	Transformation for a Wavy Wall.....	69
6.6.2	Conservation Properties.....	69
6.6.3	Solution Algorithm.....	75
7.	CONCLUDING REMARKS.....	75
8.	ACKNOWLEDGMENTS.....	77
	REFERENCES .....	78
	TABLES 1-5 .....	81
	FIGURES 1-28 .....	86

# NOMENCLATURE

$a, b$	dimensions of computational region, Eqs. (53), (54)
$a_0$	wave velocity, Eq. (42)
$A$	$(\alpha U'_w - \sigma \omega) / (\sigma - \omega/c)$ , Eq. (25)
$c$	wave propagation speed normalized by $u_\tau$
$C$	damping coefficient, Eqs. (42), (43), (44), and (47)
$C_D$	unperturbed channel drag coefficient
$C_{D_p}$	pressure drag coefficient, Eq. (38)
$D$	bending rigidity, Eq. (46), also generalized vector, Eq. (58)
$E$	spectral density, also modulus of elasticity
$E_j$	generalized vector in Eq. (58)
$\bar{f}$	a function defining the LES filter, Eq. (71)
$F$	velocity vector, Eq. (58)
$G$	filter kernel function, Eqs. (72) and (73)
$h$	value of vertical coordinate, $x_2$ at the flexible surface (Fig. 1) normalized by $\bar{\delta}$ also thickness of wall material
$J$	Jacobian of coordinate transformation
$k$	spatial wavenumber in Fourier transform space; also spring constant
$m$	mass per unit surface area, Eq. (42)
$\dot{m}$	mass flux

# NOMENCLATURE (continued)

$M_1, M_2$	mass terms, Eqs. (43) and (44)
$\bar{M}_1$	$M_1/\rho\delta$
$n$	denotes a time step in a numerical scheme
$N_x, N_z$	membrane tension in x and z directions
$p$	pressure fluctuation normalized by $\rho u_\tau^2$
$P$	mean pressure normalized by $\rho u_\tau^2$
$\bar{P}$	resolvable pressure in LES
$P'_w$	pressure fluctuation at wall
$Q_j$	transformed velocity, Eq. (84)
$Re_\tau$	$u_\tau \rho / \nu$
$R_{ii}$	two-point correlation, Eqs. (50) and (51)
$S_{ij}$	velocity gradients, Eq. (91)
$t$	time normalized by $\delta/u_\tau$
$u_i, i=1,2,3$	velocity component (Fig. 1) normalized by $u_\tau$
$(u_i'')'$	$\langle (u_i'')^2 \rangle^{1/2}$
$u_\tau$	friction velocity, $\sqrt{\tau_w/\rho}$ of flow in a rigid wall channel
$u_m$	mass average velocity of channel flow
$U_m$	$u_m/u_\tau$
$U'_w$	$(\partial \langle u_1 \rangle / \partial x_2) \big _{\text{wall}}$
$x_i, i=1,2,3$	coordinate (Fig. 1) normalized by $\delta$
$\underline{x}$	the vector $(x_1, x_2, x_3)$

# NOMENCLATURE (continued)

$x, y$	coordinates for analysis of solid wall elastic behavior, Eqs. (42) thru (47) and associated sketch
$y_w$	distance from a wall
$\alpha$	wave number in $x_1$ direction of prescribed wall shape normalized by $1/\bar{\delta}$
$\beta$	wave number in $x_3$ direction of prescribed wall shape normalized by $1/\bar{\delta}$
$\bar{\delta}$	mean channel half-width
$\delta_{ij}$	Kronecker delta
$\Delta E$	ratio of change in flow energy to energy of flow through unperturbed channel
$\Delta_i$	numerical interval, Eqs. (74) and (75)
$\epsilon_{ijk}$	antisymmetric tensor
$\eta$	displacement of wall from undisturbed plane (Fig. 1) normalized by $\bar{\delta}$
$\eta_0$	amplitude of prescribed wall displacement normalized by $\bar{\delta}$
$\theta$	direction of travel of wall wave relative to the $x_1$ axis
$\lambda$	wavelength of wall shape, normalized by $\bar{\delta}$
$\nu$	fluid viscosity
$\xi$	$1 - x_2$ , Eqs. (19) thru (22); also generalized coordinate, Eqs. (48) and (49), Eqs. (61), etc.
$\rho$	fluid density
$\sigma$	$[(\omega/c)^2 - i(\omega Re_\tau)]^{1/2}$ , Eq. (24)

## NOMENCLATURE (concluded)

$\tau_w$	fluid shear stress at wall
$\tau$	transformed time variable, Eq. (61)
$\omega$	frequency of wall motion normalized by $u_\tau/\delta$

### Special Notations

$\langle \rangle$	denotes an average over an horizontal ( $x_1, x_3$ ) plane for LES calculations plus an average over time for other calculations
$(\sim)$	denotes a periodically varying quantity
R	denotes a real part of a complex variable
I	denotes the imaginary part of a complex variable
$\partial/\partial x$	denotes a partial spatial derivative
$\delta/\delta x$	denotes a finite difference approximation of a partial derivative
$\Delta/\Delta \tau$	denotes a finite difference approximation of a partial time derivative

### Superscripts

'	denotes the nonperiodic part of a fluctuating turbulence quantity
"	denotes a fluctuating turbulence quantity
+	denotes a length in "wall units,"- e.g., $u_\tau x/\nu$
*	denotes a dimensional quantity

### Subscripts

r, i	denote real and imaginary parts when used with the quantities A and $\sigma$
------	--

## 1. INTRODUCTION

Kramer (references 1 and 2) showed that the application of a compliant coating to a wall could lead to a considerable reduction in the skin friction. He focused on reducing the drag by delaying the onset of transition to turbulent flow. Subsequent attempts to replicate his work and to determine the causal mechanisms have been only partially successful.

A number of studies of the interaction between a flow and a moving wavy surface have been made; these have been principally motivated by the air-sea interaction problem. Benjamin (reference 3), among others, showed that the pressure distribution over such a surface is not in phase with the shape of the surface; this gives rise to a momentum transfer between the fluid and the surface, the pressure drag. Although these studies employed an inviscid theory, they have played an important role in the studies of the air-sea problem.

Kendall (reference 4) investigated the turbulent flow over a wavy surface experimentally and verified some of the predictions of the inviscid theory but also found some differences.

Ffowcs-Williams (reference 5) and Blick (reference 6) studied the possibility of drag reduction by the introduction of wavy motion in the wall by means of a theory similar to the one that will be presented in this report and came to the conclusion that significant reductions in the drag should indeed be possible.

Hanratty and his co-workers at the University of Illinois have conducted a number of studies of turbulent flow close to wavy walls to obtain insight into the influence of a compliant surface on a turbulent flow field. Progress has been made in calculations of turbulent flow over small-amplitude stationary waves for which no flow separation occurs (reference 7) as well as for large-amplitude waves (reference 8). A critical issue in both cases is the specification of the wave induced variation of the properties of the turbulence.

The work reported herein was motivated by the possibility of using deliberately introduced wall waviness to reduce the drag on a surface underlying a turbulent flow. The tool used in this study is a computational one--large eddy simulation (LES)--in which the large-scale motions of the flow are explicitly computed while the small-scale motions are simulated through a model. The method has been shown to capture most of the important features of turbulent flow over flat rigid walls including the structural features that are responsible for most of the turbulence dynamics in the near-wall region (reference 9).

In this report, large eddy simulations of turbulent flow over a prescribed travelling wavy wall will be presented. The simulations were carried out with linearized boundary conditions. The results indicate that significant reduction in the pressure gradient needed to drive the flow through the channel are indeed possible. However, additional work is required to drive the wall to produce this effect and the effort expended is a considerable fraction of the reduction

in the work needed to drive the through flow. A linear analysis explaining the principal features of the effects observed will also be presented.

In the following section, the principal approximations used in this work will be introduced; these include the linearizations of the boundary conditions on which the remainder of the work was based. This is followed by two sections in which the analysis is presented. The first gives an analysis of the Stokes layer which was found to exist near the wall by Ffowcs-Williams (reference 5) and was also observed in the LES results. This is followed by an analysis of the effect of the Stokes layer on the pressure gradient and an estimate of the work done by the wall. Then the results of the large eddy simulations are presented and shown to be in substantial agreement with the predictions of the analysis. Finally, conclusions relating to the possibility of drag reduction are discussed and directions for future work are given.

## 2. BOUNDARY CONDITIONS FOR FLEXIBLE MOVING WALLS

### 2.1 Approximations

Consider flow over a surface which is able to stretch and move in the direction normal to itself. The surface is described by the displacement  $\eta(x_1, x_3, t)$  from its undisturbed plane shape, where  $x_1$  and  $x_3$  are the horizontal coordinates in the streamwise and transverse directions, and  $t$  is the time. The exact boundary conditions for the viscous flow at the surface are that the fluid



velocity relative to the surface vanishes. For small amplitude of the wall motion, a convenient approximation is to expand the velocity boundary condition in a Taylor series about the undisturbed wall plane and apply the boundary conditions on that plane. The calculations can then be performed in a channel with parallel walls and complicated time-dependent coordinate transformations can be avoided.

The process of simplification is begun by approximating the velocity at the flexible wall, whose undisturbed position is  $x_2 = 1$ , by two terms of a Taylor series.

$$u_i(x_1, h, x_3, t) = u_i(x_1, 1, x_3, t) + \eta(x_1, x_3, t) \left( \frac{\partial u_i}{\partial x_2} \right) \bigg|_{x_2=1} \quad (1)$$

where  $i=1,2,3$  and the coordinates and velocity components are defined in Figure 1. The coordinates are normalized by the mean channel half-width.

The condition of zero velocity relative to the surface at  $x_2 = h = 1 + \eta$ , yields the exact boundary condition:

$$u_i(x_1, h, x_3, t) = 0; \quad i = 1 \text{ and } 3 \quad (2)$$

$$u_2(x_1, h, x_3, t) = \partial \eta / \partial t \quad (3)$$

where tangential motion due to stretching has been neglected.

To obtain the required approximate conditions at  $x_2 = +1$  Equation (1) is substituted into Equations (2) and (3) to get:

$$u_i(x_1, 1, x_3, t) = -\eta \left( \frac{\partial u_i}{\partial x_2} \right) \bigg|_{x_2=1} ; i = 1 \text{ and } 3 \quad (4)$$

and

$$u_2(x_1, 1, x_3, t) = \frac{\partial \eta}{\partial t} - \eta \left( \frac{\partial u_2}{\partial x_2} \right) \bigg|_{x_2=1} \quad (5)$$

To simplify the boundary conditions, the velocity is considered as a combination of the time and horizontal mean value and a perturbation about that mean:

$$u_i(x_1, x_2, x_3, t) = \langle u_i(x_2) \rangle + u_i'(x_1, x_2, x_3, t); i = 1, 2, 3 \quad (6)$$

where  $\langle \rangle$  denotes the horizontal and time average. Then

$$\frac{\partial u_i}{\partial x_2} = \frac{\partial \langle u_i \rangle}{\partial x_2} + \frac{\partial u_i'}{\partial x_2} \quad (7)$$

It is assumed that  $\eta \ll \delta$  and

$$\frac{\partial u_i'}{\partial x_2} = O(\eta) \quad (8)$$

Therefore, to first order in  $\eta$

$$u_i = - \eta \left( \frac{\partial \langle u_i \rangle}{\partial x_2} \right) \Big|_{x_2=1} ; i = 1, 3 \quad (9)$$

and

$$u_2 = \frac{\partial \eta}{\partial t} \quad (10)$$

The assumption that  $\partial u_i' / \partial x_2$  is small may be a severe approximation and its validity should be checked by calculations which do not use it. It should be noted that experimental data for flow over flat plates show that the rms value of

$\partial u_i' / \partial x_2$  ( $\langle (\partial u_i' / \partial x_2)^2 \rangle^{1/2}$ ) is about 25% of  $\partial \langle u_1 \rangle / \partial x_2$  (reference 10).

The non-zero horizontal velocity component at the wall replaces the actual surface by one which is being stretched and compressed. It is important to determine whether such a condition accurately models the wavy wall. As the flow moves along the actual wall, it is displaced vertically, while remaining attached to the wall. The vertical component given by Equation (10) approximates the vertical

motion of the wall. The displacement effect is approximated by Equation (9) which indicates that the velocity at  $x_2 = 1$  is the linear extrapolation (or interpolation) of the velocity from  $x_2 = 1 + \eta$  to  $x_2 = 1$ . However, Equation (9) produces locally reversed flow for  $u_1$  where  $(1-x_2)$  is positive.

## 2.2 PARAMETERS

The calculations performed in this work used the boundary conditions (9), and (10) with the wall motion prescribed to be a progressive wave:

$$\eta(x_1, x_3, t) = \eta_0 \cos (\alpha x_1 + \beta x_3 - \omega t) \quad (11)$$

where the wavenumbers  $\alpha$  and  $\beta$  and the frequency,  $\omega$  are related to wavelength,  $\lambda$ , wave speed,  $c$ , and angle,  $\theta$ , by:

$$\omega = 2\pi c / \lambda$$

$$\alpha = (2\pi / \lambda) \cos \theta$$

$$\beta = (2\pi / \lambda) \sin \theta$$

Previous studies, e.g., Norris and Reynolds (reference 11), Hanratty et al (reference 12), Thorsness et al (reference 7), and Kelleher and Balasubramanian (reference 13) have shown that under certain conditions the use of these linearized boundary conditions may be a poor approximation. However, Norris and Reynolds' work involved wavelengths and amplitudes much larger than the ones to be considered here and the other work involved stationary wavy walls so that generalization should be made with caution. The linearization of the boundary conditions is the most significant approximation in this work.

The results of reference 13 indicate that, for calculations of laminar flow over a stationary wave, using linearized boundary conditions gives a larger amplitude in the surface shear stress variation than for calculations using the nonlinear boundary conditions. As the wave amplitude is increased, the amplitude of the shear stress variation also increases. The linearized boundary conditions predict regions of negative surface shear, indicating separation, for amplitudes for which the nonlinear boundary conditions indicate that the flow is still attached. At the same time, the use of the linearized boundary conditions appears to have little effect on the phase angle of the predicted surface shear variation. These results are only qualitative and cautionary with regard to the present study since the effects of flow turbulence and wall motion are not accounted for.

The question of the validity of the linearized boundary conditions deserves further attention. In deriving equation (9) it was assumed that  $\partial \langle u_1 \rangle / \partial x_2$  is of zero order in  $\eta$  while

$\partial u_1' / \partial x_2$  is of first order so that  $\eta(\partial u_1' / \partial x_2)$  is of second order. This assumption was based on the observation that experimental data for flat plates show that the rms value of  $\partial u_1' / \partial x_2$  is about 25% of  $\partial \langle u_1 \rangle / \partial x_2$ . The relative magnitude of  $\partial u_1' / \partial x_2$  cannot be determined a priori; therefore, the assumption that it makes a second-order contribution to the boundary condition can be evaluated only by direct comparison with a solution with exact, nonlinear boundary conditions. This evaluation is essential but could not be carried out within the scope of the present work.

### 3. ANALYTICAL STUDIES

Preliminary numerical simulations indicated that the principal effects of the wall motion are confined to a thin region near the wall; this will be demonstrated later. On this basis, it was decided to develop a simplified analysis for the near-wall region. This analysis was a valuable aid in determining values of the parameters which could yield effective alteration of the flow and viscous drag. Although the study began with numerical simulations, it is useful for the purposes of this presentation to begin with the linear analysis.

The analysis consists of two parts. First, the effect of the wall motion on the fluid near the wall was found to produce a Stokes-like layer. The Stokes-like solution was then used to estimate the change in the mean flow and the drag reduction. An energy balance was then used to estimate the benefits and costs of the wavy wall. Finally, the results of the analysis were used to choose cases for LES calculations.

### 3.1 The Linearized Stokes Layer Solution

Solutions to the linearized Navier-Stokes equations with the boundary conditions eqs. (9) - (11) will be derived here. The linearized Navier Stokes equations are:

$$\frac{\partial \tilde{u}_i}{\partial t} = - \frac{\partial \tilde{p}}{\partial x_i} - \frac{1}{Re_\tau} \nabla^2 \tilde{u}_i \quad (12)$$

$$\frac{\partial \tilde{u}_i}{\partial x_i} = 0 \text{ (summation implied)} \quad (13)$$

where the velocities are normalized by  $u_\tau$ , the friction velocity of a rigid-walled channel, pressure is normalized by  $\rho u_\tau^2$  and the symbol  $(\sim)$  denotes the periodic solution of the linearized problem. The problem is solved by the complex imbedding technique, that is, the velocity components and the pressure are treated as complex and are assumed to have the form:

$$\tilde{f}(x_1, x_2, x_3, t) = \hat{f}(x_2) e^{i(\alpha x_1 + \beta x_3 - \omega t)} \quad (14)$$

with the wall motion given by

$$\eta(x_1, x_3, t) = \eta_0 e^{i(\alpha x_1 + \beta x_3 - \omega t)} \quad (15)$$

The actual solution is the real part of the result.

For the purpose of this analysis, the moving wall is the upper wall of the channel ( $x_2=1$ ) and the lower wall is considered to be at  $-\infty$ . Substitution of eqs. (14) and (15) into eqs. (12) and (13) and the boundary conditions:

$$\tilde{u}_1(x_1, 1, x_3, t) = -\eta U'_w \quad (16)$$

$$\tilde{u}_2(x_1, 1, x_3, t) = \frac{\partial \eta}{\partial t} \quad (17)$$

$$\tilde{u}_3(x_1, 1, x_3, t) = 0 \quad (18)$$



yields

$$\hat{p}(x_2) = \eta_0 c A e^{-(\omega/c)\xi} \quad (19)$$

$$\hat{u}_1(x_2) = -\eta_0 (U'_w + \frac{\alpha c}{\omega} A) e^{-\sigma \xi} + \eta_0 \frac{\alpha c}{\omega} A e^{-(\omega/c)\xi} \quad (20)$$

$$\hat{u}_2(x_2) = -i\eta_0 (\omega - A) e^{-\sigma \xi} - i\eta_0 A e^{-(\omega/c)\xi} \quad (21)$$

$$\hat{u}_3(x_2) = \frac{\beta \eta_0 c}{\omega} A (e^{-(\omega/c)\xi} - e^{-\sigma \xi}) \quad (22)$$

where

$$\xi = 1 - x_2$$

$$\frac{\omega}{c} = (\alpha^2 + \beta^2)^{1/2} \quad (23)$$

$$\sigma = [(\omega/c)^2 - i(\omega \text{Re}_T)]^{1/2} \quad (24)$$

and

$$A = \frac{\alpha U'_w - \sigma \omega}{\sigma - \omega/c} \quad (25)$$

The velocity  $\tilde{u}_i$  is given by

$$\begin{aligned}\tilde{u}_i(x_1, x_2, x_3, t) &= R[\hat{u}_i(x_2)] e^{i(\alpha x_1 + \beta x_3 - \omega t)} \\ &= R[\hat{u}_i(x_2)] \cos(\alpha x_1 + \beta x_3 - \omega t) \\ &\quad - I[\hat{u}_i(x_2)] \sin(\alpha x_1 + \beta x_3 - \omega t)\end{aligned}\quad (26)$$

where  $R$  indicates the real part and  $I$  indicates the imaginary part. The Reynolds stress is the average over time and  $x_1$  and  $x_3$  of the product  $\tilde{u}_1 \tilde{u}_2$  and will be shown later to be the agent of the principal effect of wall motion on the turbulent flow. From the above results

$$\begin{aligned}\langle \tilde{u}_1 \tilde{u}_2 \rangle &= \frac{1}{2} [R(\hat{u}_1)R(\hat{u}_2) + I(\hat{u}_1)I(\hat{u}_2)] \\ &= \frac{1}{2} \eta_0^2 (\alpha c + U_w') [A_i e^{-2\sigma_r \xi} - (A_i \cos \sigma_i \xi + A_r \sin \sigma_i \xi) e^{-(\sigma_r + \omega/c)\xi}]\end{aligned}\quad (27)$$

where  $A_r$  and  $A_i$ ,  $\sigma_r$  and  $\sigma_i$  denote real and imaginary parts of  $A$  and  $\sigma$ , respectively. This Reynolds stress is plotted in Figure 2. Note that it undergoes a damped oscillation and in the region nearest the wall is opposite in sign to the unperturbed Reynolds stress.

### 3.2 Numerical Solutions for Nonlinear Stokes Layer

In order to evaluate the effect of neglecting the convective terms of the Navier-Stokes equations in the Stokes layer analysis, a numerical solution of the problem was obtained using a computer code for unsteady viscous incompressible flows (reference 14). The code uses a factored semi-implicit solution algorithm that is explicit in convective terms, and implicit in viscous terms. The method is second-order accurate in both space and time. For the present calculations, the code solved the two-dimensional incompressible Navier-Stokes equations in a channel with the lower wall rigid, and periodicity assumed for the inflow and outflow boundaries. The boundary conditions, Eqs. (9) - (11) were applied to the upper wall of the channel; calculations were performed both with the complete nonlinear Navier-Stokes equations and with the convection terms omitted. All quantities were nondimensionalized in "wall units," i.e., in terms of friction velocity,  $u_\tau$  and viscosity,  $\nu$ . The reference values were

$$U_m = 18.848$$

$$c = .78 U_m$$

$$\eta_O^+ = \eta_O u_\tau / \nu = 5$$

$$\lambda^+ = \lambda u_\tau / \nu = 200$$

$$\theta = 0$$

$$\delta^+ = Re_\tau = 640$$

The results for the wall motion-induced Reynolds stress near the moving wall are shown in Figure 3 for three different computational mesh sizes and the analytical solution [equation (27)]. The symbols are located at the computational mesh points. Symbols + and x represent the finest mesh, open symbols the coarsest mesh. Some discrepancy between the analytical and numerical solutions results from truncation error in the finite difference formulation. However, a more significant effect is produced by the neglect of the convective terms in the linear solutions. The nonlinearities reduce the amplitude of the response of the fluid in the Stokes layer. It is important to note that in the cases shown in Figure 3, the results are entirely due to the interaction of the wall motion with the adjacent viscous fluid. No turbulence is included in the computation.

### 3.3 Estimate of Effect of Stokes Layer on Mean Pressure Gradient

#### 3.3.1 Mixing Length Analysis

The second step in the analysis is to obtain an estimate of the drag reduction. The velocity and pressure in the channel flow with a wavy wall can be decomposed into three components (reference 15).

$$u_i(\underline{x}, t) = \langle u_i(x_2) \rangle + \tilde{u}_i(\underline{x}, t) + u_i'(\underline{x}, t) ; i=1,2,3 \quad (28)$$

$$p(\underline{x}, t) = P(x_1) + \tilde{p}(\underline{x}, t) + p'(\underline{x}, t) \quad (29)$$

where  $\langle u_i \rangle$  is the mean velocity,  $\tilde{u}_i$  is the periodic part of the solution induced by the wall motion, and  $u_i'$  represents the turbulent fluctuations:  $P$ ,  $\tilde{p}$ , and  $p'$  have similar meanings. It is assumed that the periodic component is nothing more than the Stokes layer solution derived in the previous two sections.

The nondimensional Navier-Stokes equations, averaged over time and horizontal planes are (reference 11):

$$\frac{\partial}{\partial x_2} (\langle \tilde{u}_1 \tilde{u}_2 + u_1' u_2' \rangle) = - \frac{dP}{dx_1} + \frac{1}{Re_\tau} \frac{\partial^2}{\partial x_2^2} \langle u_1 \rangle \quad (30)$$

where it has been assumed that  $\langle \tilde{u}_1 u_2' + u_1' \tilde{u}_2 \rangle$  is negligible, i.e., that the turbulence and the Stokes Layer are uncorrelated. Assuming the  $\langle u_1' u_2' \rangle$  is not affected by the presence of  $\langle \tilde{u}_1 \tilde{u}_2 \rangle$ , the mixing length eddy viscosity model with Van Driest correction (reference 16), can be used to yield.

$$\frac{\partial}{\partial x_2} \left[ \left( 1 + \epsilon \frac{\partial}{\partial x_2} \langle u_1 \rangle \right) \frac{\partial}{\partial x_2} \langle u_1 \rangle \right] = Re_\tau \left( \frac{\partial}{\partial x_2} \langle \tilde{u}_1 \tilde{u}_2 \rangle + \frac{dP}{dx_1} \right) \quad (31)$$

where

$$\frac{\epsilon}{Re_\tau} = \text{Min} \{ (K)^2, [.41(1-|x_2|)^2] [1 - e^{-Re_\tau(1-|x_2|)/26}]^2 \} \quad (32)$$

Where K is a constant which will be determined subsequently.

Calculations of the  $\langle \tilde{u}_1 \tilde{u}_2 \rangle$  profile were performed with the assumption of symmetry at the channel centerline which implies that both walls are wavy. Integrating eq. (31) in  $x_2$  with the conditions that  $\epsilon$  and  $\langle \tilde{u}_1 \tilde{u}_2 \rangle$  are zero at  $x_2 = \pm 1$  gives

$$\frac{\partial}{\partial x_2} \langle u_1 \rangle = - \frac{1}{2\epsilon} \{ 1 - [1 - 4\epsilon R_{e_\tau} (\langle \tilde{u}_1 \tilde{u}_2 \rangle + x_2 \frac{\partial P}{\partial x_1})]^{1/2} \} \quad (33)$$

The  $\langle u_1 \rangle$  profile (Figure 4) was then obtained by numerical integration of Eq. (33) using a fourth order Runge-Kutta scheme. The required values of  $\langle \tilde{u}_1 \tilde{u}_2 \rangle$  were obtained from Eq. (27). The mass flow rate

$$\dot{m} \int_{-1}^1 \langle u_1 \rangle dx_2 \quad (34)$$

was then obtained by trapezoidal rule integration of the calculated  $\langle u_1 \rangle$  profile. The value of the constant  $K$  in Eq. (32) was determined by trial and error so that the mass flow rate calculated from Eqs. (33) and (34) with  $\langle \tilde{u}_1 \tilde{u}_2 \rangle = 0$  would equal the mass flow rate used in the LES calculations to be discussed subsequently. The value determined in this way was

$$K = 0.085$$

### 3.3.2 Momentum Balance

The effect of the wall motion was determined from the momentum balance. The time averaged momentum equation was integrated over a control volume bounded by the channel walls and periodic in-flow/out-flow boundaries. The first step of the process is averaging over horizontal planes, which yields Eq. (30). The next step is to integrate over the width of the channel to get.

$$\langle \tilde{u}_1 \tilde{u}_2 + u_1' u_2' \rangle \Big|_{-1}^1 = -2 \frac{dp}{dx_1} + \frac{1}{Re_\tau} \frac{\partial \langle u_1 \rangle}{\partial x_2} \Big|_{-1}^1 \quad (35)$$

Since both the periodic and the turbulent Reynolds stress are zero at the channel walls, Eq. (35) yields, for symmetric flow

$$\frac{dp}{dx_1} = \frac{1}{Re_\tau} \frac{\partial \langle u_1 \rangle}{\partial x_2} \Big|_{x_2 = 1} = \frac{1}{Re_\tau} U_w' \quad (36)$$

It is noted that since the walls are horizontal there are no horizontal pressure forces in the momentum balance. Thus, the only effect of the waviness that is felt by the flow is that of the wall motion on the mean velocity gradient at the wall.

In order to determine the effect of wall motion on the velocity



In order to determine the effect of wall motion on the velocity gradient at the wall, Eq. (33) was integrated using Eq. (36) and different values of  $dp/dx_1$ . The value of the  $dp/dx_1$  was adjusted by Newton's iteration method so the calculated mass flux given by Eq. (34) was equal to the mass flux of the unperturbed channel. The resulting increment in  $dp/dx_1$  is assumed to be twice the value that would be obtained with one moving wall and one rigid wall.

### 3.3.3 Results

The results for five specific cases are listed in Table 1. The table includes results from numerical integration of equations (33), and (34) , and from LES calculations which will be discussed subsequently. The values listed for the changes in  $dp/dx_1$ , from Eqs. (33) and (34) are half the values actually calculated in order to compare with the LES results which were obtained for a channel with one rigid and one moving wall.

The mixing length analysis was used to calculate the wall motion effects over a continuous range of the various parameters. A few cases were then selected for LES calculations. Case 1 is the reference case for which the parameters were listed in section 3.2. The value chosen for  $c$  corresponds approximately to the convection velocity of large scale eddies (reference 17). The value of five wall units for  $\eta_0^+$  is roughly the thickness of the viscous sublayer and was considered to be the limit of applicability of the linearized boundary conditions. The wavelength of 200 wall units

approximates the streamwise spacing of large eddies near the wall. Case 2 is the same as Case 1 except for the negative value of  $c$  which corresponds to a wave moving upstream. Case 3 corresponds to wall waves rotated  $90^\circ$  and moving in the spanwise direction. Case 4 is similar to case 2 to determine the effects of the magnitude of the wave speed.

The effect of the wall motion on the mean velocity profile as calculated by the integral theory is shown in figure 4 for case 2. The figure illustrates that the effect of the wall motion on the mean velocity profile is felt throughout the channel. This will be discussed further when the LES results are presented. The inset in Figure 4 illustrates that the  $\partial \langle u_1 \rangle / \partial x_2$  at the wall is lower for the wavy wall than for the rigid wall. The momentum balance shows that this reduces  $dP/dx_1$ . This figure also indicates the resolution required to correctly calculate the flow by LES; the computational mesh should have a point 0.2 wall units from the wall.

An important observation is that the wall motion can significantly affect the pressure gradient. The simplified theory presented here gives a larger pressure gradient reduction than LES. A major reason for this difference is that the Reynolds stress is overpredicted by the linear theory (Fig. 3).

The decrease in the driving pressure gradient can be explained as follows. The wall motion sets up a Stokes-like layer in its immediate vicinity. This layer has a "Reynolds Stress"

$\langle \tilde{u}_1 \tilde{u}_2 \rangle$  opposite in sign to the Reynolds Stress of the turbulence itself. The added "Reynolds Stress" acts to decrease the turbulence

production near the wall and thereby reduces the turbulent Reynolds Stress and the shear force on the wall. Reduction of the shear stress must, by momentum conservation, be accompanied by a reduced pressure gradient.

### 3.4 Energy Balance

A method of evaluating the net effect of the wall motion is to examine the energy balance. The mean energy equation is derived by taking the scalar product of the momentum equation with the velocity and averaging over time and a control volume bounded by the channel walls and periodic inflow, outflow and side planes. The resulting energy equation is

$$\begin{aligned}
 -u_m dP/dx_1 - \langle \tilde{p}\tilde{u}_2 \rangle + \frac{1}{2Re_\tau} \langle \frac{\partial}{\partial x_2} (\tilde{u}_1^2 + \tilde{u}_2^2 + \tilde{u}_3^2) \rangle \\
 = \frac{1}{T} \int_0^T \frac{1}{V} \int_V \frac{\partial u_i}{\partial x_j} \frac{\partial u_i}{\partial x_j} dv
 \end{aligned}
 \tag{37}$$

where  $V$  is the control volume. In Eq. (37)  $\langle \rangle$  indicates time and horizontal plane averages evaluated at the moving wall.

In the rigid-walled channel, the energy required to move the fluid through the channel is balanced by the dissipation. The moving wall contributes to the energy balance through the work done by viscous forces and by the fluctuating pressure at the wall and by changing the dissipation. Thus, any reduction in the required

energy to drive the flow may be offset by the work required to generate the Stokes layer.

Negative values of the wall pressure-work and positive values of the viscous-work terms represent energy added to the fluid by the wall. These must be considered penalties to be deducted from the reduced through-flow pressure-work requirement.

The various components of the energy balance are shown as functions of the wave speed in Figure 5. The energy throughput increment is the mean velocity,  $U_m$  times the change in the mean pressure gradient,  $dP/dx_1$  from its unperturbed channel (half the change in  $dP/dx_1$  found from the mixing-length analysis described in section 3.3). The  $\langle \tilde{p}\tilde{u}_2 \rangle$  and viscous wall work terms are evaluated using the linear theory. The change in dissipation was not computed; it is estimated that the dissipation is reduced somewhat by the wavy wall so the results should be conservative. Clearly, a large part of the change in the work required to drive the through flow is offset by the viscous work done by the wall motion. This is independent of the direction of the motion. On the other hand, the pressure work is direction dependent. For downstream wave motion at moderate wave speeds, the pressure work is negative, indicating that the wall absorbs energy from the fluid. Thus, the fluid drives the wall motion. For upstream wave motion, the wall adds energy to the fluid through the  $\langle \tilde{p}\tilde{u}_2 \rangle$  interaction. This suggests that upstream wave motion is not possible for compliant walls because it cannot be driven by the flow.

The net effect of the Stokes layer on the energy required to drive the flow through the channel is shown in Figure 6. A small net decrease in energy required is produced by a wall moving either upstream or downstream at moderate speeds; note that the change in dissipation is not included. The theoretical curve shown in Figure 6 displays singular behavior around  $c = 0$ . This is an inadequacy of the linearized theory.

The results shown in Figures 5 and 6 differ from results given in an earlier interim report (Ref. 18). The reason is that in the earlier report, the  $\langle \tilde{u}_1 \tilde{u}_2 \rangle$  contribution to Eq. (33) was reduced by an arbitrary factor of 0.5 to account approximately for nonlinearities (see Figure 3). The arbitrary reduction was not done here. Also, in the previous work the value of  $U_w'$  used in all calculations of quantities from the linear theory was the rigid-wall value. Since the slope of the mean velocity profile at the wall changes along with the mean pressure gradient, the present calculations also include the correct value of  $U_w'$ , given by Eq. (36). Although the approximations used lead to results that are only qualitative, the results suggest that (a) the effect of a wavy wall is to reduce the energy required to drive the flow and (b) the reduction is small.

In addition to the approximations already discussed, the turbulent pressure fluctuation was not included in calculating the pressure work term. The effect of including these fluctuations is

unknown as the theory does not predict the change in the turbulence quantities.

As the linear theory predicts a larger magnitude of reversed Reynolds stress near the wavy wall than the nonlinear theory, it is expected that the linear theory would overpredict the reduction in the mean pressure gradient and the viscous work and the pressure work at the wavy wall. A further illustration of the effects of the nonlinearities can be seen in the variation of the intensity of the velocity fluctuations produced in the Stokes layer. Figure 7 shows the variation of the rms velocity fluctuations  $\sqrt{\langle \tilde{u}_1^2 \rangle}$  near the wall for the linear and the nonlinear Stokes layer solutions for case 2. The linear solution has larger (negative) slope  $(\partial \sqrt{\langle \tilde{u}_1^2 \rangle} / \partial x_2)$  at the wall than does the nonlinear solution. This suggests that the actual viscous work would be smaller than predicted by the linear theory. However, the errors in the predicted quantities are expected to be small and to follow the correct trends. Therefore, the linear theory is believed to be a useful guide for LES calculations.

This study indicates that, in general, the wall must supply energy to produce the conditions that result in reduced mean pressure gradient. The question of whether a significant net reduction in the energy required to drive the flow is possible is the essential one. This investigation indicates that the amount of energy required from the wall is roughly equal to the amount of energy saved by the drag reduction.

### 3.5 Extension to Compliant Walls

The theory developed above can be extended to provide a method of estimating the drag in a channel containing compliant walls. As in the theory presented above, the fluid is considered as a device which responds to the wall shape by producing pressure fluctuations at the surface. In a similar manner, one can construct a linearized approximation to the dynamics of a solid wall, in which the wall is represented as a device which responds to the pressure fluctuations by producing surface displacements. This is essentially a linear control systems transfer function approach to the problem. In this view, the combined system is represented as shown in the figure below.

To make this calculation possible the following elements are needed:

1. The spectrum in space and time of the pressure fluctuations on a wall in natural turbulent flow. This could be obtained from either an experiment or a full or large eddy simulation. To date, only limited portions of the necessary data have been published, namely the time spectra of the pressure fluctuations.
2. A dynamic linearized model of the wall in which the input is the pressure fluctuations on the surface and the output is the surface displacement. This is just the dispersion relation for the surface and needs to be specified from the dynamics of deformable bodies. A more sophisticated model might include the effect of the surface shear stresses; however, these are not likely to be important.
3. A model for the effects of the wall surface displacement on the flow. The Stokes layer model presented above should be adequate for this task.

The suggested combination of these elements would produce a model capable of predicting the drag in a compliant wall channel containing a turbulent flow. On the basis of the experience



described in this report, it is anticipated that this theory will be useful in estimating the change in drag and the properties of the surface which would produce the greatest drag but will not be quantitatively accurate. Unfortunately, time restrictions prohibited the present study from investigating this model.

### 3.6 Pressure Drag

The momentum balance shows that, under the approximations employed, there is no pressure drag on the wall. However, an estimate of the pressure drag on the actual wavy wall can be obtained by assuming that the Stokes layer pressure at the displaced wall would obtain at the wavy wall. A "drag coefficient" can then be found by integration.

$$C_{D_p} = - \frac{2}{\rho U_m^2} \langle \tilde{p} \frac{\partial \eta}{\partial x_1} \rangle \quad (38)$$

Using equations (11) and (19), this becomes

$$C_{D_p} = -\eta_0^2 \alpha c A_i / U_m^2 \quad (39)$$

The viscous drag of the unperturbed channel is in equilibrium with the pressure drop:

$$C_D = 4/U_m^2 \quad (40)$$

so that

$$C_{D_p}/C_D = -\eta_0^2 \alpha c A_i / 4 \quad (41)$$

For cases 1, 2, and 4 of Table 1, the pressure drag from Eq. (41) is 3.9 percent, 10.4 percent, and 13.2 percent respectively. For spanwise waves, no pressure drag is produced. The LES results shown in Table 1 will be discussed subsequently.

#### 4. COMPLIANT WALL DYNAMICS

The work on the effects of moving walls with prescribed shapes on turbulent flow provided considerable understanding of the interaction between wall motion and the fluid flow. The principal purpose of this work was directed at understanding the interaction of a compliant wall with the flow. In this case, the equations for the wall motion must be solved simultaneously with the fluid equations.

If only streamwise variations in wall shape are allowed, the dynamic equation satisfied by the displacement  $y = \eta(x,t)$  of the plane surface bounding an elastic medium, including linear damping, is the second order equation (Benjamin, reference 3)

$$a_0^2 \frac{\partial^2 \eta}{\partial x^2} - \frac{\partial^2 \eta}{\partial t^2} - C \frac{\partial \eta}{\partial t} = p/m \quad (42)$$

where

$a_0$  is the velocity of free waves

$C$  is the damping coefficient

$p$  is the external pressure applied to the surface

$x$  is the streamwise coordinate

$m$  is the mass of the elastic material per unit surface area

Equation (42) can easily be extended to allow variation in the spanwise direction.

Yang and Heller (reference 19) analyzed a viscoelastic plate sandwiched between a rigid plate and flexible membrane. They obtained a pair of equations similar to equation (42) containing several additional terms; they allow for variation of the surface displacement in two directions. The major omissions in both of these approaches are the shearing stresses and rotary inertia in the dispersive material.

Accurate accounting for all possible effects is shown by Achenbach (reference 20) to produce a set of three rather complicated equations which admit many modes of vibration, each having its own dispersion curve. However, it is not known whether all modes are important in the fluid interaction problem. The modes associated with shearing and rotational motions are expected to interact much more weakly with the flow than the modes due to bending and thickness deformations produced by a fluctuating pressure.

Under the compliant Coating Drag Reduction Program sponsored by the U.S. Office of Naval Research, a considerable amount of work has been done to determine the characteristics of elastic surfaces which could interact strongly with the fluid flow. Much of the effort has been directed toward development of mathematical models of various combinations of layers of viscoelastic materials. Duncan and Hsu (reference 21) studied single-and double-layer viscoelastic coatings, and estimated the material properties required for maximum interaction with pressure fluctuations of the flow. Kalnins and Evrensel (reference 22) demonstrated how a composite, compliant coating could be modeled by a one degree-of-freedom system, similar to a membrane. At the time of the present work, a definitive description of a compliant surface had not been developed. The viscoelastic sandwich structure studied by Yang and Heller provided a simple means of testing the feasibility of coupling the LES with a compliant surface. The equations derived for the surface deflection

due to an imposed pressure distribution represent in an approximate way surfaces ranging from simple membranes to viscoelastic layers.

The compliant wall is assumed to be a laminated structure composed of a layer of a viscoelastic material between a stiff plate and a thin flexible plate.

The base plate is assumed to be subjected to small deflection, while the upper plate may undergo large deflections and, in addition, may be subjected to in-plane forces. According to Yang and Heller, experiments have shown that the Poisson's ratio,  $\nu$ , of PVC foam under transverse loads is nearly zero. This allows the assumption that the middle layer can be treated as a viscoelastic spring. The equations of motion of the composite plate then become

$$\begin{aligned}
M_1 \frac{\partial^2 \eta_1}{\partial t^2} + \frac{1}{6} \rho_3 h_3 \frac{\partial^2 \eta_2}{\partial t^2} + C_3 \left( \frac{\partial \eta_1}{\partial t} - \frac{\partial \eta_2}{\partial t} \right) \\
+ k_3 (\eta_1 - \eta_2) + D_1 \nabla^4 \eta_1 - N_x \frac{\partial^2 \eta_1}{\partial x^2} \\
- N_z \frac{\partial^2 \eta_1}{\partial z^2} = p(x, z, t)
\end{aligned} \tag{43}$$

and

$$\begin{aligned}
M_2 \frac{\partial^2 \eta_2}{\partial t^2} + \frac{1}{6} \rho_3 h_3 \frac{\partial^2 \eta_1}{\partial t^2} + C_3 \left( \frac{\partial \eta_2}{\partial t} - \frac{\partial \eta_1}{\partial t} \right) \\
+ k_3 (\eta_2 - \eta_1) + D_2 \nabla^4 \eta_2 = 0
\end{aligned} \tag{44}$$

where  $M_1 = \frac{1}{3} \rho_3 h_3 + \rho_1 h_1$ ,  $M_2 = \frac{1}{3} \rho_3 h_3 + \rho_2 h_2$ , and  $\rho_1$ ,  $\rho_2$ ,  $h_1$ ,  $h_2$ ,  $\eta_1(x, z, t)$  and  $\eta_2(x, z, t)$  are the masses per unit volume, thicknesses and transverse displacements of the upper plates and the base plate, respectively, and  $\rho_3$  and  $h_3$  are the mass per unit volume and thickness of the viscoelastic medium. The quantity  $C_3$  is the damping coefficient of the viscoelastic middle layer.

The spring constant  $k_3$  is related to the elastic modulus and the thickness of the middle layer by

$$k_3 = \frac{E_3}{h_3} \quad (45)$$

The quantities  $D_1$  and  $D_2$  are the bending rigidities of the upper plate and the base plate, respectively, with elastic moduli  $E_1$  and  $E_2$  and Poisson's ratios  $\nu_1$  and  $\nu_2$ :

$$D_i = \frac{E_i h_i}{12(1-\nu_i^2)} ; \quad i = 1, 2 \quad (46)$$

The function  $p(x, z, t)$  in equation (43) is the boundary layer pressure fluctuation.

If the base plate is completely rigid so that  $D_2 \rightarrow \infty$ , the base plate deflection can be neglected, eliminating equation (44). Equation (43) then reduces to

$$\begin{aligned} M_1 \frac{\partial^2 \eta}{\partial t^2} + C_3 \frac{\partial \eta}{\partial t} + k_3 \eta + D_1 \nabla^4 \eta \\ - N_x \frac{\partial^2 \eta}{\partial x^2} - N_z \frac{\partial^2 \eta}{\partial z^2} = p(x, z, t) \end{aligned} \quad (47)$$

In what follows, all lengths are nondimensionalized with the mean channel half-width,  $\bar{\delta}$ , densities with the fluid density,  $\rho$ ,

velocities with the fluid friction velocity,  $u_\tau = \sqrt{\tau_w/\rho}$ , and pressure and stresses with  $\rho u_\tau^2$ . The values used for the dimensional quantities are listed in table 2.

With the compliant wall displacement,  $\eta$ , included as a dependent variable along with the fluid velocity components and the pressure, equation (47) is solved simultaneously with the channel flow equations by writing it as two first order equations

$$\frac{\partial \eta}{\partial t} = \xi \quad (48)$$

$$\begin{aligned} \frac{\partial \xi}{\partial t} = & - [C_3 \xi + k_3 \eta + D_1 \nabla^4 \eta - N_x \frac{\partial^2 \eta}{\partial x^2} \\ & - N_z \frac{\partial^2 \eta}{\partial z^2} - p] \frac{1}{M_1} \end{aligned} \quad (49)$$

which are solved simultaneously with the fluid flow equations by the (implicit) Crank-Nicolson method.

## 5. LARGE-EDDY SIMULATION

The large-eddy simulation (LES) code used in this work is described in Reference 9. The equations for the large-scale flow field are obtained by integration of the filtered, three-dimensional, time-dependent Navier-Stokes equations. The small-scale field motions are simulated through an eddy-viscosity model. The program permits simulation of a turbulent channel flow at moderate Reynolds number ( $Re_\tau \approx 14000$ ).



The LES code was shown to capture most of the important features of the turbulent channel flow. Calculated results are in good agreement with experimental data for statistical quantities. Low- and high-speed streaks alternating in the spanwise direction found in the numerical results were in good qualitative agreement with experimental observations. The calculated production of turbulence was found to be intermittent in a manner that strongly resembles that seen in the laboratory.

The impetus for the present work was the capability of the three-dimensional time-dependent, numerical simulation to provide detailed, instantaneous information about the flow at many spatial locations. This information can be used effectively to study the structure and statistical properties of the flow. For the case of time- and spatially-varying boundary conditions, this capability provides a unique opportunity to study the mechanics of the interaction between the wall motion and the turbulent flow.

The code originally was developed for use on the ILLIAC IV computer at NASA/Ames Research Center. Some of the calculations for prescribed wall motion discussed in this report were performed on that computer. The code was modified for use on the NASA/Ames CRAY computer where the remainder of the calculations were done.

The LES calculations were made in three stages. First, a preliminary calculation was made to evaluate whether the choice of wall parameters would produce observable effects. Then, after the analytical studies provided guidelines for the choice of wall parameters, a second set of calculations was performed. Both stages employed a coordinate mesh that consisted of 64 points in the  $x_1$  and  $x_2$  directions (streamwise and normal to the walls) and 128 points in the  $x_3$  (spanwise) direction. In stage two, both prescribed wall motion and compliant wall motion were studied. In the final stage, 102 points were used in the  $x_2$  direction to better resolve the near wall region. Also, the terms of the global energy balance equation and pressure drag were calculated.

In the following sections, the results of both the coarse mesh and the fine mesh LES calculations will be used to illustrate the effects of the wall motion. Some of the results of the coarse-mesh calculations were presented in reference 18.

### 5.1 LES Results for Prescribed Wall Motion

The four cases discussed previously (section 3 and Table 1) were computed using the LES code. Since the sign of Reynolds stress  $-\langle u_1'' u_2'' \rangle$ , where  $u_1'' = u_1 - \langle u_1 \rangle$ , for a steady turbulent channel flow is negative near the upper wall, wall parameters were selected for which the linear theory, Eq. (27) gave positive values of  $-\langle \tilde{u}_1 \tilde{u}_2 \rangle$ ; this should reduce the production of turbulence and yield drag reduction.

The first computational mesh used in the LES code was approximately the same near the wall as the coarsest mesh shown in Figure 3. The finest mesh used for LES calculations had 102 points in the  $x_2$  direction, and near the wavy wall approximately corresponded to the finest mesh shown in Figure 3. The details of the computational mesh are listed in Table 3. Note that the distance from each wall in wall units is included in the table. These values are only approximate since they are based on the friction velocity of a rigid channel. For the channel with different boundary conditions on opposite walls, the mesh spacing in wall units will differ slightly for each wall.

Starting from an initial velocity field representing the flow in the rigid-walled channel, the governing equations were integrated forward in time with the prescribed moving wall conditions until the numerical solutions reached statistically steady states. The mass flux was held fixed while the mean pressure gradient was allowed to float.

#### 5.1.1 Effect of Wall Motion on Pressure Gradient

In Figure 8a, the pressure gradients for the rigid-walled channel and for the wavy-walled channels of Cases 1, 2, and 3, of Table 1 are shown; the coarse mesh was used for these cases. Using the fine mesh, cases 1 and 2 were recalculated and an additional case (case 4) with a higher-speed upstream-traveling wall wave was run; these results are given in Figure 8b. The terms of the energy balance equation were also computed in the fine mesh calculations.

All cases have an initial transient period wherein the solution adjusts from the rigid wall solution to the moving wall solution. Case 4 was started using the solution from the last time step of Case 2. This resulted in smaller initial oscillation and faster damping.

The coarse and fine mesh results are similar; the pressure gradient reductions agree quite well. The coarse mesh produces a reduction in  $dp/dx_1$  of about 5 percent for Case 1 and nearly 20 percent for Case 2, while the fine mesh produces reductions of about 3.5 and 17 percent, respectively. For case 3, the coarse mesh calculation produces a 10 percent reduction in  $dp/dx_1$ . The high speed case 4 calculated with the fine mesh yields a greater reduction (20 percent). The trends are consistent with the linear theory predictions.

#### 5.1.2 Effect of Wall Motion on Turbulence

Examples of the turbulence statistics from LES calculations are shown in Figures 9-16. All the figures show results of the fine mesh calculations. All cases show similar effects of the moving wall on the turbulence statistics.

In Figure 9, the mean velocity profile is shown for Case 2 using the fine mesh; the behavior is similar to that of the Stokes layer theory shown in Figure 4. Of particular interest is the expanded inset which shows the high resolution of the fine mesh which accurately predicts the lower value of the  $d \langle u_1 \rangle / dx_2$  at the moving wall.

Figure 8 shows only 400 time steps for the coarse mesh cases, 1200 steps for the fine mesh cases 1 and 2 and 900 steps for case 4. The total run length for the coarse mesh cases was 1600 steps; the profiles of the various quantities shown in Figures 9-16 were calculated by averaging over horizontal planes and the last 200 time steps. Profiles from the fine mesh calculations represent averages over the last 300 steps after a total run length of 1200 steps for cases 1 and 2 and 900 steps for case 4. Because of the short time-averaging period, the profiles suffer from some statistical noise. Nevertheless, certain trends can be discerned which indicate the effects of the wall motion on the turbulence.

In Figure 10, the horizontally averaged turbulence intensity components,  $\langle u_i^2 \rangle^{1/2}$  from Case 1 for the lower and upper halves of the wavy-walled channel, respectively, are shown. The only significant difference between the two halves of the flow occurs very near the upper (wavy) wall, where the  $u_1$  and  $u_2$  intensities increase significantly. The effect is shown more clearly in Figure 11, where the turbulence intensity  $\langle u_1^2 \rangle^{1/2}$  is compared for the rigid and moving walls for cases 1, 2, and 4. The intensity is very high at the moving wall in all cases but rapidly falls to a variation similar to that near the rigid wall.

In Figure 12 the turbulent shear stress for Cases 1, 2, and 4 is compared for the rigid and moving walls. Near the wavy wall the shear stress changes sign as expected. Near the channel center, statistical noise obscures any effects that might be present.

In Section 3 of this report, it was shown (Fig. 3) that the nonlinear terms of the Navier-Stokes equations have a large role in determining the effect of wall motion on the flow Reynolds stress and, consequently, on the drag of the channel. In Figure 13, the Reynolds stress from the nonlinear Stokes layer solutions for cases 1, 2, and 4 is compared with the LES results. Clearly, turbulence has an appreciable effect on the moving-wall/flow interaction. In particular, for the downstream-moving wall, LES produces much less  $\langle u_1'' u_2'' \rangle$  reversal. Also, it is clear why the fine mesh LES solution yields less reduction in the channel pressure gradient than the coarse mesh solution. The high resolution mesh, gives a significantly smaller Stokes layer contribution to  $\langle u_1'' u_2'' \rangle$ .

Two point correlation functions

$$R_{ii}(x_2, r_1) = \frac{\langle f_i''(\underline{x}) f_i''(x_1 + r_1, x_2, x_3) \rangle}{\langle f_i''^2(\underline{x}) \rangle} \quad (50)$$

$$R_{ii}(x_2, r_3) = \frac{\langle f_i''(\underline{x}) f_i''(x_1, x_2, x_3 + r_3) \rangle}{\langle f_i''^2(\underline{x}) \rangle} \quad (51)$$

where  $f''$  represents the fluctuating velocities,  $u_i''$  for  $i = 1, 2, 3$ , or the pressure fluctuation,  $p$  for  $i = 4$ , are plotted in Figure 14

at two vertical locations, one near the lower rigid wall and one near the upper wavy wall for case 1. The channel centerline is located 640 wall units from each wall. In this section, the  $\langle \rangle$  indicates an horizontal average. Since the statistics were not time-averaged, they suffer from statistical fluctuations, particularly at large separation distance. The longitudinal correlation near the rigid wall shown in Figure 14(a) is like that of Reference 9 for the rigid-walled channel. For small separation distances, the correlation for  $u_1''$  is larger than that for the corresponding transverse components,  $u_2''$  and  $u_3''$  and the pressure, and it extends over much longer distances than do the other correlations. This is also true in the upper half of the channel except very near the boundary. As the wavy wall is approached [Figure 14(b)], the correlation becomes dominated by the wall motion. At  $x_2 = .914$ , ( $y_w^+ \approx 55$  for a rigid walled channel) some effect of the boundary motion is apparent in  $u_2''$  and  $p$ . A smaller effect is discernible in the  $u_1''$ , while  $u_3''$  is completely unaffected. These comparisons show that the effects of the wall motion are felt for a considerable distance into the flow.

In the spanwise direction, the two-point correlations show very little wall motion effect except very near the upper boundary where the  $u_1''$ ,  $u_2''$  and  $p$  become highly correlated across the entire span of the channel due to the two-dimensional nature of the wall motion.

Energy spectra of the turbulence are shown in Figure 15 for the same two locations as for the two-point correlations. The effects

of the wall motion are evident in the spectra of the longitudinal and vertical energy components [Figure 15(b)] where sharp peaks occur at the wavenumber of the prescribed wall motion. The wall motion makes a negligible contribution to the spanwise energy spectra.

The same comments generally apply to the results of case 3 except that the largest effects occur in spanwise two-point correlations and energy spectra.

### 5.1.3 Energy Balance

As shown in Section 3.4, the presence of a moving wavy wall introduces two new terms to the kinetic energy integral equation. One term is the result of work done by the fluctuating pressure on the vertical motion of the wall. The other term is the work done by the viscous forces. These terms represent energy supplied or absorbed by the wall and must be compared to the reduction in the energy required to drive the main flow through the channel.

In Figure 16, the components of the energy balance from the LES are compared to the results of the linear theory. Three cases are represented for the LES: the downstream-traveling wave (case 1), and two upstream-traveling waves (cases 2 and 4). The LES results are generally in good overall agreement with the linear theory. The pressure work term is particularly well predicted by the theory, whereas the theory estimates the viscous work to be higher than the LES result. These results are consistent with those discussed



previously in connection with Figure 7 (Section 3.4), where it was shown that the inclusion of the nonlinearities significantly reduced the gradient of the turbulence intensity near the wall. This also results in a reduction in the viscous work term. It was found that the intensity gradient was further reduced in the LES.

The net result of the energy balance is shown in Figure 17. Again, the results of the linear theory are reproduced for comparison. The LES results seem to agree with the linear theory in predicting a net decrease in the energy requirement for both upstream- and downstream-traveling waves in the low-speed range. However, the calculation of the net energy reduction involves a small difference between quantities which are of similar magnitudes, each of which is subject to some uncertainty due to numerical error and statistical noise. Although, it cannot be stated unequivocally that a net drag reduction is produced, the fact that both LES and linear theory predict such a reduction makes it probable that a small net drag reduction is actually achieved.

#### 5.1.4 Pressure Drag

In a manner similar to the calculation of pressure drag by the linear theory in Section 3.6 of this report, the pressure drag was calculated in the LES by integrating the pressure fluctuations at the fictitious wall over the actual wall, i.e., as

$$C_{D_P} = - \frac{2}{\rho u_m^2} \langle \bar{P} \frac{\partial \eta}{\partial x_1} \rangle \quad (52)$$

where  $\bar{P}$  is the resolvable portion of the turbulent wall-pressure fluctuation from the LES calculation. The results of this calculation are included in Table 1 as compared to the drag of the unperturbed channel. For cases 1 and 4, the pressure drag predicted by the LES is somewhat smaller than predicted by the linear theory.

These comparisons are only a qualitative estimate of the channel drag since there is no actual pressure drag with the linearized boundary conditions. The interaction of the pressure fluctuations with the real wall cannot be evaluated except by use of a calculation scheme that employs the complete nonlinear boundary conditions. This needs to be done if valid results are to be obtained.

## 5.2 LES Results for Compliant Wall Motion

### 5.2.1 Effects of Turbulence on Wall Motion

Some calculations were performed for compliant walls using the coarse mesh LES program coupled to the compliant wall Equations (48) and (49). Several cases were calculated using various values of the elastic constants,  $k_3$ ,  $C_3$ , and  $D_1$  and membrane tension  $N_x$  and  $N_z$  (table 4). The first case used values given by Yang and Heller as

characteristic of a Mylar membrane and a PVC plastisol substrate. The non-dimensional tension forces applied to the membrane were varied from 0 to  $10^4$  (corresponding to 0 to 300 n/m). The material properties from Yang and Heller (reference 19) correspond to the following non-dimensional parameters

$$\bar{K}_3 = k_3 \bar{\delta} / (\rho u_\tau^2) = 1514$$

$$\bar{C}_3 = C_3 / (\rho u_\tau) = .098$$

$$\bar{D}_1 = D_1 / (\rho u_\tau^2 \bar{\delta}^3) = 1.58$$

$$\bar{N}_x = \bar{N}_z = N_x / (\rho u_\tau^2 \bar{\delta}) = 9082$$

Figure 18 shows the time history of the rms wall deflection (in wall units) and the rms wall velocity,  $\eta_t/u_\tau$  for the first case where  $\bar{N}_x = \bar{N}_z = 9082$ . The calculations appear to have reached a statistically steady state. However, the magnitude of the wall deflection is very small, on the order of 0.02 wall units. As the prescribed wall motion cases had a nondimensional surface deflection for the prescribed wall shape of five wall units and produced a small effect, this deflection will produce entirely negligible effects. As should be expected with such a small surface response, no effect on the mean pressure gradient was observed.

Insight into the nature of the interaction is obtained by examining the dispersion relation for the surface. For the general viscoelastic composite material described by Eq. (47), with damping coefficient,  $C_3 = 0$ , the natural frequency is,

$$\omega = \left\{ \frac{\bar{k}_3}{\bar{M}_1} + \frac{\pi^2}{\bar{M}_1} \left[ \bar{N}_x \left( \frac{n_x}{a} \right)^2 + \bar{N}_z \left( \frac{n_z}{b} \right)^2 \right] + \frac{\pi^4 \bar{D}_1}{\bar{M}_1} \left[ \left( \frac{n_x}{a} \right)^4 + \left( \frac{n_x n_z}{ab} \right)^2 + \left( \frac{n_z}{b} \right)^4 \right] \right\}^{1/2} \quad (53)$$

where  $n_x$ , and  $n_z = 0, 1, 2, \dots$ ,  $\bar{M}_1 = M_1 / \rho \delta$  and  $a$  and  $b$  are the length and width of the membrane.

For a simple membrane with  $k_3 = 0$  and negligible stiffness, the natural frequency becomes

$$\omega = \left\{ \frac{\pi^2}{\bar{M}_1} \left[ \bar{N}_x \left( \frac{n_x}{a} \right)^2 + \bar{N}_z \left( \frac{n_z}{b} \right)^2 \right] \right\}^{1/2} \quad (54)$$

In the present case

$$a = 2b = 2\pi$$

so

$$\omega = \frac{1}{2} \left\{ \frac{1}{\bar{M}_1} [\bar{N}_x (n_x)^2 + \bar{N}_z (2n_z)^2] \right\}^{1/2} \quad (55)$$

The characteristic time for the various modes can be found from

$$T_c = 2\pi/\omega$$

$$\text{For } \bar{N}_x/\bar{M}_1 = \bar{N}_z/\bar{M}_1 = 2000$$

$$T_c = 2\pi \left[ \frac{.002}{n_x^2 + (2n_z)^2} \right]^{1/2} \quad (56)$$

Values of  $T_c$  for the first 6 modes are listed in Table 5.

The parameters used for the calculations shown in Figure 18 correspond to a natural frequency of a spring-mass system which is approximately

$$\omega = \frac{\bar{\delta} \omega^*}{u_\tau} = \left( \frac{\bar{k}_3}{\bar{M}_1} \right)^{1/2} \sim 45$$

where  $\omega^*$  is the dimensional frequency in Hertz.

An estimate can be made as follows for the frequency of the turbulence pressure that contains the maximum energy. From experimental measurements (reference 17) the convection velocity of the turbulent pressure fluctuations at the wall is estimated to be  $.8U_m$ . A nominal value for the mean streamwise extent of the eddies producing the pressure fluctuations is two hundred wall units; the corresponding value for the non-dimensional frequency is

$$\omega \sim 300$$

Anticipating that resonance between the turbulent pressure fluctuation spectrum and the vibration characteristics of the wall is necessary to produce significant effects, the parameters of the surface equations were adjusted to make the natural frequency of the surface more closely correspond to the characteristic frequency of the fluid flow. The membrane tensions were set to zero ( $N_x = N_z = 0$ ), the viscoelastic damping,  $C_3$ , was zero, the bending stiffness  $D_1$  was increased and the spring constant,  $k_3$ , was increased to raise the vibration frequency (case 2 in Table 4). The resulting mean rms wall deflection was  $\eta^+ \sim .013$ , indicating no resonance between the wall and the flow, and as before, there was no noticeable effect on the mean channel pressure gradient. This indicates that the estimate of the required resonant frequency was incorrect. For these small wall deflections the linearized

treatment of wall boundary conditions is accurate.

Other calculations were made with the surface equations containing only the membrane tension terms. That is,

$$k_3 = C_3 = D_1 = 0$$

For the first such case (case 3 in table 4)

$$\frac{\bar{N}_x}{\bar{M}_1} = \frac{\bar{N}_z}{\bar{M}_1} = 200$$

This produced a wall vibration response to the turbulent pressure fluctuations which increased continuously (Figure 19), showing no tendency to stabilize. The calculation was halted when the amplitude of the wall deflections reached five wall units due to anticipated errors from linearization of the boundary conditions. Increasing  $\bar{N}_x/\bar{M}_1$  and  $\bar{N}_z/\bar{M}_1$  to 2000 produced a wall vibration which increased stepwise (Figure 20). Starting from no vibration, the wall amplitude increased and appeared to stabilize at an rms value of two wall units. After about 600 calculation steps (a time of about  $0.225\bar{\delta}/u_\tau$ ), the amplitude again began to increase, and then stabilized at about four wall units. After another short period of stability, the amplitude again began to increase.

In order to obtain more insight into the nature of the interaction the pressure fluctuations and the wall shapes for the various cases calculated are examined. In Figure 21, the distribution of pressure fluctuations on the compliant wall is plotted for the case of a membrane with  $\bar{N}_x/\bar{M}_1 = \bar{N}_z/\bar{M}_1 = 2000$  at integration step 600 ( $T = .225$ ); this pressure distribution is typical. It is quite three-dimensional and contains a variety of wavelengths. By contrast, the surface shape is characterized by longer wavelength displacements and, in most cases, near two-dimensionality corresponding to the natural modes of vibration of the membrane. Figure 22 shows the surface displacement for the Yang and Heller surface which has an rms displacement of about  $.02 v/u_\tau$  (Figure 18). Figure 23 shows the surface shape for the modified Yang and Heller surface (case 2, table 4) for which the damping,  $C_3$ , was zero, the membrane tensions were zero and the spring constant,  $k_3$ , was adjusted to increase the natural frequency of the elastic material. This surface shows more three-dimensionality but is still dominated by long wavelengths and small amplitudes. The nearly two-dimensional surface displacement in Figure 22 corresponds to one of the natural modes due to the dominant membrane terms of equation (53), whereas the more three-dimensional displacements in Figure 23 are due primarily to the spring constant term  $k_3\eta$  and the stiffness term  $DV^4\eta$ . Recall that in this case, the membrane stretching terms were absent ( $N_x = N_z = 0$ ).



These results indicate the need for information about the space-time spectra of the pressure fluctuations in order to "tune" the surface parameters to achieve resonance with the flow. Such information would be very difficult to obtain experimentally, but it could be obtained using LES. Such calculations are suggested as possible future work.

The largest surface displacements were obtained for the membrane surfaces. Figure 24 shows the membrane surface for the case with  $N_x/M_1 = N_z/M_1 = 2000$  at five different times. The membrane deformation is nearly two-dimensional. The stepwise behavior of the rms amplitude of the membrane vibration discussed previously is found to correspond to a progressive development of different modes of the vibration.

The dispersion relation Eq. (55) shows the reason for the two-dimensionality of the membrane surface. First, the computational region is rectangular, so that the lowest mode is dominated by the lowest mode of the longest side, which is in the streamwise direction. For integration times shorter than the characteristic time of the second longitudinal mode, (see table 4) both streamwise and spanwise waves develop. Then, as the time for the second longitudinal mode is reached, at approximately  $T = 0.142$ , the surface develops the wave shown in Figure 24 (a). As the integration proceeds further, the subharmonic wave begins to develop and becomes complete as the integration time exceeds  $T = 0.28$  Figures 24 (b), (c) and (d). Further integration increases the

amplitude of the subharmonic wave while the higher frequency waves in both the streamwise and the spanwise directions are damped, yielding the smooth, two-dimensional wave shown in Figure 24 (e).

Comparison of the compliant-membrane calculations with the prescribed-wall results reveals that while the compliant-wall shape was roughly two-dimensional and sinusoidal like the prescribed wall, with comparable amplitude, the dominant wavelength produced (the region size) was much longer than the prescribed value (.05 x region size). The prescribed wall motion produced a discernible drag reduction because it had the proper length scales to interact with the energy-carrying motions of the flow. The compliant walls had wavelengths too long to interact significantly with the turbulence. To match both frequency and wavelength of the turbulence the wall wave will need to have a wavespeed about equal to the flow speed. This is the essential criterion and requires very low wave speeds for solids. So the wall will need low tension, high density, and low stiffness.

#### 5.2.2 Wall Motion Effects on Turbulence

The only compliant surfaces for which noticeable effects were produced in the flow were the membranes. Results for the case with  $\bar{N}_x/\bar{M}_1 = \bar{N}_z/\bar{M}_1 = 2000$  are shown in Figures 25-28. In Figure 25 the turbulence intensity components,  $(u_1'')'$ ,  $(u_2'')'$ ,  $(u_3'')'$  for the lower and upper halves of the channel respectively are shown.

As for the prescribed wall case shown in (Figure 9), the only significant differences occur very near the upper wall, where the  $(u_1'')'$  and  $(u_2'')'$  increase due to the wall motion. Here, the greatest effect is seen in the  $u_1$ -component, while the  $u_2$ -component has only a slight increase in intensity due to the wall motion.

In Figure 26, the turbulent shear stress is shown. In contrast to the prescribed-wall result, there is no noticeable effect.

Two-point correlation functions as defined by Eqs. (50) and (51) are shown in Figure 27 at the same distance ( $x_2 = \pm .990$ ) from each boundary. At the lower boundary [Figure 27(a)] the longitudinal correlations are typical of turbulent flow near a rigid boundary. Near the upper boundary [Figure 27(b)], the longitudinal correlations for the pressure and the spanwise velocity component,  $u_3$ , are unaffected by the wall motion, while the  $u_1$  and  $u_2$  components clearly show the long wavelength of the boundary shape. As expected, the effect did not propagate very far into the flow. The next level at which the solution was examined was at  $x_2 = .941$ ; no effects could be seen.

In the spanwise direction, the two-point correlations reveal the two-dimensional nature of the wall motion. The pressure and  $u_3$ -velocity correlations are unaffected by the wall motion, but the  $u_1$ - and  $u_2$ -components are highly correlated across the entire span of the calculation.

Energy spectra of the turbulence are shown in Figure 28 for the same two locations as for the two-point correlations.

The longitudinal and vertical energy components show a significant increase due to the wall motion in the energy contained in the lower wavenumber range.

### 5.3 LES Results for Other Types of Wall Conditions

#### 5.3.1 "Smart Wall" Experiments

In the belief that the optimum drag reduction would result from a wall that destroyed all of the turbulent pressure fluctuations, cases which imposed such a boundary condition were run. In the "standard" problem, the three velocity components,  $u_1$ ,  $u_2$ , and  $u_3$ , are specified at the wall and the pressure is computed. In the modified calculation, the  $u_1$  and  $u_3$  velocity components were specified to be zero, and the pressure was specified to be constant at the wall while the  $u_2$  velocity component was computed. This corresponds to a porous wall with a plenum behind it. Calculations resulted in a higher mean pressure gradient indicating that the technique actually results in increased drag.

#### 5.3.2 Distributed Suction/Blowing

A boundary condition which represents a distribution of suction and blowing through a wall without wall motion is

$$\begin{aligned}u_1 &= u_3 = 0 \\u_2 &= A \sin (\alpha x_1 + \beta x_3 - \omega t)\end{aligned}$$

The specific formulation used here has a simple traveling wave form.

Calculations were performed for this formulation both with LES and the mixing length analysis. For a value of  $A$  which gives the same  $u_2$  amplitude as the moving walls, the Stokes layer Reynolds stress is smaller than when the accompanying  $u_1$  boundary condition is present. As a consequence, the effect on the mean pressure gradient is less than for the moving wall. Another result was that the change in the mean pressure gradient was positive for waves moving downstream and negative for waves moving upstream. That is, downstream-traveling waves produced a drag increase, and upstream-traveling waves produced a drag reduction.

### 5.3.3 Longitudinal Grooves

A drag reduction technique that has been shown to be effective experimentally is that of longitudinally-grooved surfaces having groove depths and spacings on the order of the turbulent wall-streak and burst dimensions (reference 23). In order to investigate the applicability of LES, two cases were calculated for longitudinal grooves of sinusoidal profile. The surface shape was described by Eq. (11) with  $\alpha = 0$  and  $\omega = 0$ . The boundary conditions were Eqs. (9) and (10). The values used for the other parameters were

$$n_0^+ = 5 \text{ and } 6$$

$$\beta = 40 \text{ and } 8$$

The values of  $\beta$  correspond to a wavelength (groove spacing) of 100 and 500 wall units, respectively.

The results were that the short wavelength case produced a slight increase in the mean channel pressure gradient, while the long wavelength case showed essentially no change in the pressure gradient. Experimental results (reference 23) show that sharp-edged grooves with spacings of 10-20 wall units are required to produce a significant effect. The fact that no effects were observed in the LES with smooth grooves is consistent with those results.

#### 6.0 LES IN GENERALIZED COORDINATES

It was shown in a previous section that the use of linearized boundary conditions places limitations on the magnitude of the parameters defining the wall motion and especially, on the amplitude. Furthermore, the values required to produce interesting effects are close to the limits of validity of the model. In this section, a formulation of the equations for large-eddy simulation of the channel flow using the exact wall boundary conditions is presented. The formulation is based on a generalized coordinate transformation applied to the Navier-Stokes equations and then specialized to the case of flow in a channel with one flexible wall. Implementation of the formulation was beyond the scope of the present project, but is required if LES is to be used to explore the significant part of the parameter space. This section documents the

derivation of the equations, provides some analysis of potential sources of difficulty, and suggests the procedure for completing the analysis.

### 6.1 Governing Equations

The complete nonlinear Navier-Stokes equations, with velocities normalized by the friction velocity, lengths normalized by the channel half-width and pressure normalized by  $\rho u_\tau^2$ , can be written

$$\frac{\partial D}{\partial t} + \frac{\partial E_j}{\partial x_j} = \frac{1}{Re_\tau} \frac{\partial}{\partial x_k} \left( \frac{\partial F}{\partial x_k} \right) \quad (57)$$

where

$$D = \begin{Bmatrix} \rho \\ u \\ 1 \\ u \\ 2 \\ u \\ 3 \end{Bmatrix}; E_j = \begin{Bmatrix} u & u_j \\ u_1 & u_j \\ u_2 & u_j \\ u_3 & u_j \end{Bmatrix} + \begin{Bmatrix} \rho u_j \\ \delta_{1j} \rho \\ \delta_{2j} \rho \\ \delta_{3j} \rho \end{Bmatrix}; F = \begin{Bmatrix} 0 \\ u \\ 1 \\ u \\ 2 \\ u \\ 3 \end{Bmatrix} \quad (58)$$

and

$$Re_\tau = \frac{u_\tau \delta}{\nu} \quad (59)$$

## 6.2 Boundary Conditions

The boundary conditions for flow in a channel consist of the condition of no-slip at the channel walls and the condition that the velocity components are all periodic at the inflow and outflow boundaries and at the lateral boundaries:

$$\begin{aligned}u_i(x_1, 0, x_3, t) &= 0 \quad \text{for } i = 1, 2, 3 \\u_1(x, h, x_3, t) &= u_3(x_1, h, x_3, t) = 0 \\u_2(x_1, h, x_3, t) &= \frac{\partial h}{\partial t}(x_1, x_3, t) \\u_i(x_1 + a, x_2, x_3, t) &= u_i(x_1, x_2, x_3, t) \\u_i(x_1, x_2, x_3 + b, t) &= u_i(x_1, x_2, x_3, t)\end{aligned} \tag{60}$$

where  $h$  is the instantaneous distance between the channel walls and  $a$  and  $b$  are the length and width of the computational region (note that the definition of  $x_2$  has been changed so that  $x_2 = 0$  is the lower wall and  $x_2 = h$  is the upper wall).

## 6.3 Coordinate Transformation

Define a general transformation of the form

$$\begin{aligned}\tau &= t \\ \xi_i &= f(x_j, t) \quad \text{for } i, j = 1, 2, 3\end{aligned} \tag{61}$$



where  $\xi_2$  is defined so that  $\xi_2 = 0$  is the channel centerline and the channel walls are at  $\xi_2 = \pm 1$ .

The chain rule yields

$$\frac{\partial}{\partial t} = \frac{\partial}{\partial \tau} + \frac{\partial \xi_j}{\partial t} \frac{\partial}{\partial \xi_j} \quad (62)$$

and

$$\frac{\partial}{\partial x_i} = \frac{\partial \xi_j}{\partial x_i} \frac{\partial}{\partial \xi_j} \quad (63)$$

The inverse transformation is

$$\frac{\partial}{\partial \tau} = \frac{\partial}{\partial t} + \frac{\partial x_j}{\partial \tau} \frac{\partial}{\partial x_j} \quad (64)$$

and

$$\frac{\partial}{\partial \xi_i} = \frac{\partial x_j}{\partial \xi_i} \frac{\partial}{\partial x_j} \quad (65)$$

with Equations (62) and (63), Equation (57) can be written

$$\begin{aligned}
 J \frac{\partial}{\partial \tau} (J^{-1} D) + J \frac{\partial}{\partial \xi_j} \left( J^{-1} D \frac{\partial \xi_j}{\partial t} + J^{-1} \frac{\partial \xi_j}{\partial x_k} E_k \right) \\
 - JD \left[ \frac{\partial}{\partial \tau} (J^{-1}) + \frac{\partial}{\partial \xi_j} \left( J^{-1} \frac{\partial \xi_j}{\partial t} \right) \right] \\
 - JE_k \frac{\partial}{\partial \xi_j} \left( J^{-1} \frac{\partial \xi_j}{\partial x_k} \right) = \frac{1}{R_{e_\tau}} \nabla^2 D
 \end{aligned} \tag{66}$$

where  $J$  is the Jacobian of the transformation

$$J = \frac{1}{6} \epsilon_{ijk} \epsilon_{lmn} \frac{\partial \xi_i}{\partial x_l} \frac{\partial \xi_j}{\partial x_m} \frac{\partial \xi_k}{\partial x_n} \tag{67}$$

and

$$\nabla^2 D = \frac{\partial \xi_l}{\partial x_k} \frac{\partial}{\partial \xi_l} \left( \frac{\partial \xi_m}{\partial x_k} \frac{\partial D}{\partial \xi_m} \right) \tag{68}$$

and after some manipulation, it can be shown that equation (66) becomes, for incompressible flow,

$$\frac{\partial}{\partial \xi_j} \left( J^{-1} \frac{\partial \xi_j}{\partial x_k} u_k \right) = 0 \tag{69}$$

and

$$\begin{aligned} \frac{\partial}{\partial \tau} (J^{-1} u_i) + \frac{\partial}{\partial \xi_j} (J^{-1} u_i \frac{\partial \xi_j}{\partial \tau}) + \frac{\partial}{\partial \xi_j} (J^{-1} \frac{\partial \xi_j}{\partial x_k} u_i u_k) \\ + \frac{\partial}{\partial \xi_j} (J^{-1} \frac{\partial \xi_j}{\partial x_k} \delta_{ik} P) = \frac{J^{-1}}{Re_\tau} \nabla^2 u_i \end{aligned} \quad (70)$$

#### 6.4 Filtering

The next step in developing the flow equations for large-eddy simulation is to apply a filter to Equations (69) and (70). The filter used by Moin and Kim (reference 9) will be applied in the transformed coordinates. This is equivalent to assuming that the small scale fluctuations move up and down and stretch with the moving wall. The filter takes the form

$$\bar{f}(\xi_i, \tau) = \iiint_V f(\xi_i', \tau) \left[ \prod_{k=1}^3 G(\xi_k - \xi_k') d\xi_k' \right] \quad (71)$$

where, for  $i = 1$  and  $3$

$$G(\xi_i - \xi_i') = \left( \frac{6}{\pi \Delta_i} \right)^{1/2} \exp \left[ -6(\xi_i - \xi_i')^2 / \Delta_i^2 \right] \quad (72)$$

and for  $i = 2$

$$G(\xi_2 - \xi_2') = \begin{cases} \frac{1}{\Delta^+(\xi_2) + \Delta^-(\xi_2)} & \text{for } (\xi_2 - \Delta^-) < \xi_2' < \xi_2 + \Delta^+ \\ 0 & \text{for } \xi_2' > (\xi_2 + \Delta^+) \\ & \text{and } \xi_2' < (\xi_2 - \Delta^-) \end{cases} \quad (73)$$

where

$$\Delta^+(\xi_2) = \frac{1}{2} (\xi_{2j+1} - \xi_{2j}) \quad (74)$$

and

$$\Delta^-(\xi_2) = \frac{1}{2} (\xi_{2j} - \xi_{2j-1}) \quad (75)$$

for

$$\frac{1}{2} (\xi_{2j} + \xi_{2j-1}) < \xi_2 < \frac{1}{2} (\xi_{2j} + \xi_{2j+1}) \quad (76)$$

## 6.5 Generalized Equations

It is assumed that the wall shape consists only of large scale variations. Applying the filter to Equations (69) and (70) yields the dynamical equations of the large-scale flow field in the transformed coordinates.

The continuity equation becomes:

$$\frac{\partial}{\partial \xi_j} (J^{-1} \frac{\partial \xi_j}{\partial x_k} \bar{u}_k) = 0 \quad (77)$$

and the momentum equations are:

$$\begin{aligned} \frac{\partial}{\partial \tau} (J^{-1} \bar{u}_i) + \frac{\partial}{\partial \xi_j} (J^{-1} \bar{u}_i \frac{\partial \xi_j}{\partial \tau}) + \frac{\partial}{\partial \xi_j} (J^{-1} \frac{\partial \xi_j}{\partial x_k} \bar{u}_i \bar{u}_k) \\ + \frac{\partial}{\partial \xi_j} (J^{-1} \frac{\partial \xi_j}{\partial x_k} \delta_{ik} \bar{P}) = \frac{J^{-1}}{Re_\tau} \nabla^2 \bar{u}_i \end{aligned} \quad (78)$$

The product  $\bar{u}_i \bar{u}_k$  contains small-scale components which must be accounted for. Each component is decomposed into a filtered (large-scale) part and an unfiltered (small-scale) part, eq.,  $u_i = \bar{u}_i + u'_i$ . Then filtering  $u_i u_k$  yields

$$\overline{u_i u_k} = \overline{\bar{u}_i \bar{u}_k} + R_{ik} \quad (79)$$

where

$$\bar{R}_{ik} = \overline{\bar{u}_i u'_k} + \overline{u'_i \bar{u}_k} + \overline{u'_i u'_k} \quad (80)$$

The subgrid scale stresses are defined by

$$\bar{\tau}_{ik} = \bar{R}_{ik} - \frac{1}{3} \delta_{ik} \bar{R}_{\ell\ell} \quad (81)$$

and the modified pressure is

$$\bar{\bar{P}} = \bar{P} + \frac{1}{3} \bar{R}_{\ell\ell} \quad (82)$$

The filtered momentum equation [(equation (85))] then becomes

$$\begin{aligned} \frac{\partial}{\partial \tau} (J^{-1} \bar{u}_i) + \frac{\partial}{\partial \xi_j} (J^{-1} \bar{u}_i \frac{\partial \xi_j}{\partial \tau}) + \frac{\partial}{\partial \xi_j} (J^{-1} \frac{\partial \xi_j}{\partial x_k} \overline{\bar{u}_i \bar{u}_k}) \\ + \frac{\partial}{\partial \xi_j} (J^{-1} \frac{\partial \xi_j}{\partial x_k} \bar{\tau}_{ik}) + \frac{\partial}{\partial \xi_j} (J^{-1} \frac{\partial \xi_j}{\partial x_k} \delta_{ik} \bar{\bar{P}}) = \frac{J^{-1}}{Re_\tau} \nabla^2 \bar{u}_i \end{aligned} \quad (83)$$

Numerical solution of Equations (77) and (83) requires careful consideration of the conservation properties; these are discussed in the next section.

The channel flow computer program developed by Moin and Kim has been thoroughly tested and evaluated and has been found to be accurate, and stable for channels with flat walls. For channels

with more general wall conditions, it is desirable to use numerical methods which reduce to the existing method. As a first step in developing such a method, define transformed velocity components as

$$Q_j = J^{-1} \frac{\partial \xi_j}{\partial x_k} u_k \quad (84)$$

With this definition, equation (72) becomes

$$\frac{\partial Q_j}{\partial \xi_j} = 0 \quad (85)$$

Using the inverse velocity transformation,

$$u_i = J \frac{\partial x_i}{\partial \xi_j} Q_j \quad (86)$$

and adding appropriate terms to both sides of the resulting equation, equation (83) becomes, after some manipulation

$$\frac{\partial \bar{Q}_i}{\partial \tau} = [(1 + \delta_{i2}) \langle v_t \rangle + \delta_{i1} v_t^* + \frac{1}{R_{e_\tau}}] \frac{\partial^2 \bar{Q}_i}{\partial \xi_2^2} \quad (87)$$

$$+ \frac{1}{R_{e_\tau}} \left( \frac{\partial^2 \bar{Q}_i}{\partial \xi_1^2} + \frac{\partial^2 \bar{Q}_i}{\partial \xi_2^2} \right) - \frac{\partial \bar{P}}{\partial \xi_i} + H_i$$

where

$$\begin{aligned} H_i = & \frac{1}{R_{e_\tau}} J^{-1} v^2 \left( J \frac{\partial x_i}{\partial \xi_j} \bar{Q} \right) - \frac{\partial^2 \bar{Q}_i}{\partial \xi_j \partial \xi_j} \\ & + \frac{\partial}{\partial \tau} \left( \bar{Q}_i - \frac{\partial x_i}{\partial \xi_j} \bar{Q}_j \right) - \frac{\partial}{\partial \xi_j} \left( \frac{\partial x_i}{\partial \xi_k} \frac{\partial \xi_j}{\partial t} \bar{Q}_k \right) \\ & + \frac{\partial}{\partial \xi_j} \left[ \left( \delta_{ij} - J^{-1} \frac{\partial \xi_j}{\partial x_k} \delta_{ik} \right) \bar{P} \right] - \frac{\partial}{\partial \xi_j} \left( J^{-1} \frac{\partial \xi_j}{\partial x_k} \overline{u_i u_k} \right) \\ & - \frac{\partial}{\partial \xi_j} \left( J^{-1} \frac{\partial \xi_j}{\partial x_k} \bar{\tau}_{ik} \right) - [(1 + \delta_{i2}) \langle v_t \rangle + \delta_{i1} v_t^*] \frac{\partial^2 \bar{Q}_i}{\partial \xi_2^2} \end{aligned} \quad (88)$$

Equation (87) is identical in form to equation (5.1) of reference 9. The terms representing the velocity components and the



right-hand side of the equation are more complicated and the turbulent shear stress has not yet been completely defined.

The boundary conditions are:

$$\begin{aligned}
 \bar{Q}_i &= 0 \text{ at } \xi_2 = -1; i = 1, 2, 3 \\
 \bar{Q}_1 &= \bar{Q}_3 = 0 \text{ at } \xi_2 = +1 \\
 \bar{Q}_2 &= \frac{1}{J} \frac{\partial \xi_2}{\partial x_2} \frac{1}{\delta} \frac{\partial h}{\partial t} \text{ at } \xi_2 = +1 \\
 \bar{Q}_i &= \text{periodic in } \xi_1 \text{ and } \xi_3
 \end{aligned} \tag{89}$$

The turbulent shear stress in equation (88) is defined in the same manner as in reference 9. That is

$$\tau_{ij} = 2v_T(S_{ij} - \langle S_{ij} \rangle) - 2v_T^* \langle S_{ij} \rangle \tag{90}$$

where  $v_T$  and  $v_T^*$  are the small-scale eddy viscosities which represent the action of the unresolved scales of motion on those that are resolved. In the generalized equations, it is appropriate to describe the shear stress in terms of the transformed velocities and coordinates. Accordingly,

$$S_{ij} = \frac{1}{2} \left( \frac{\partial \bar{Q}_i}{\partial \xi_j} + \frac{\partial \bar{Q}_j}{\partial \xi_i} \right) \tag{91}$$

## 6.6 Discretization of the Generalized Equations

### 6.6.1 Transformation for a Wavy Wall

It has been pointed out by several previous researchers that when studying flows over wavy walls it is desirable to allow the eddy viscosity and turbulent kinetic energy profiles to move up and down with the wall. Also, since measurements are most easily made with a probe which moves up and down with the wall or is located at a fixed point, a completely curvilinear coordinate system is not practical. A coordinate transformation which satisfies these considerations and allows the calculations to be performed in a channel of fixed width is

$$\begin{aligned}\tau &= t \\ \xi_1 &= x_1 \\ \xi_2 &= 2x_2/h(x_1, x_3, t) - 1 \\ \xi_3 &= x_3\end{aligned}\tag{92}$$

Thus, while  $x_2$  varies from zero to  $h(x_1, x_3, t)$ ,  $\xi_2$  varies from -1 to +1.

### 6.6.2 Conservation Properties

It is generally accepted that, in the numerical treatment of a differential conservation law, the equations must be in strong

conservation form in order to capture discontinuities properly (cf. Lax (reference 24), Viviand (reference 25), and Vinokur (reference 26) and others). This requirement has been primarily enforced for compressible flows where capturing shock waves is important. However, these properties are important in incompressible flows as well (reference 27).

In the incompressible case, because of the uncoupling of the mass and momentum conservation equations from the thermodynamic energy equation, the momentum equation carries a second important property; conservation of kinetic energy. In reference 9, the momentum equation is written in a particular form which is found to conserve energy, momentum, and circulation with virtually any difference scheme. The generalization to the present case, is not clear. The construction of an energy-conserving difference scheme in the generalized coordinate problem is crucial, and should be the next step in completing the analysis. It was not possible due to time limitations to complete that step in this effort.

The requirements for mass conservation and the time differencing requirements for momentum conservation are easily demonstrated. Consider equations (85) and (87) expressed as difference equations:

$$\frac{\delta \bar{Q}_j}{\delta \xi_j} = 0 \quad (93)$$

$$\frac{\Delta \bar{Q}_i}{\Delta \tau} = [(1 + \delta_{i2}) \langle v_T \rangle + \delta_{i1} v_T^* + \frac{1}{R_{e_\tau}}] \frac{\delta}{\delta \xi_2} \frac{\delta \bar{Q}_i}{\delta \xi_2} \quad (94)$$

$$+ \frac{1}{R_{e_\tau}} \left[ \frac{\delta}{\delta \xi_1} \left( \frac{\delta \bar{Q}_i}{\delta \xi_1} \right) + \frac{\delta}{\delta \xi_3} \left( \frac{\delta \bar{Q}_i}{\delta \xi_3} \right) \right] - \frac{\delta \bar{P}}{\delta \xi_i} + H_i$$

where  $\delta/\delta \xi$  is a finite difference approximation to  $\partial/\partial \xi$  and  $\Delta$  represents the finite difference between time steps  $n$  and  $n+1$ ,

$$\Delta = ( )^{n+1} - ( )^n \quad (95)$$

Now, conditions which will ensure conservation in a uniform flow field are examined. If the flow field represented by the velocity components,  $u_i$ , is uniform, then Equation (93) with (86) implies the following difference relation:

$$\frac{\delta}{\delta \xi_j} \left( J^{-1} \frac{\delta \xi_j}{\delta x_i} \right) = 0 \quad (96)$$

Similarly, the requirement that the transformed momentum equation should numerically conserve momentum in a uniform flow leads to the following difference equation

$$\begin{aligned}
 & \frac{\Delta}{\Delta \tau} (J^{-1} \frac{\delta \xi_i}{\delta x_k}) \\
 & - [(1 + \delta_{i2}) \langle v_T \rangle + \delta_{i1} v_T^* + \frac{1}{R_{e\tau}}] \frac{\delta}{\delta \xi_2} [\frac{\delta}{\delta \xi_2} (J^{-1} \frac{\delta \xi_i}{\delta x_k})] \\
 & + \frac{1}{R_{e\tau}} \{ \frac{\delta}{\delta \xi_1} [\frac{\delta}{\delta \xi_1} (J^{-1} \frac{\delta \xi_i}{\delta x_k})] + \frac{\delta}{\delta \xi_3} [\frac{\delta}{\delta \xi_3} (J^{-1} \frac{\delta \xi_i}{\delta x_k})] \} \\
 & = H_i
 \end{aligned} \tag{97}$$

Now the term  $H_i$  contains terms identical to those on the left-hand side of equation (97). Thus, for uniform flows, equation (97) reduces to

$$\frac{\Delta J^{-1}}{\Delta \tau} + \frac{\delta}{\delta \xi_j} (J^{-1} \frac{\Delta \xi_j}{\Delta t}) = 0 \tag{98}$$

The transformation described in the previous section yields the following difference relations:

$$J^{-1} = h/2$$

$$J^{-1} \frac{\delta \xi_i}{\delta x_i} = h/2 \quad ; i = 1, 3$$

$$J^{-1} \frac{\delta \xi_i}{\delta x_j} = 0 \quad ; \quad \begin{matrix} i = 1, j = 2, 3 \\ i = 2, j = 1, 2 \end{matrix}$$

$$J^{-1} \frac{\delta \xi_2}{\delta x_i} = -\frac{1}{2} (\xi_2 + 1) \frac{\delta h}{\delta \xi_i} \quad ; i = 1, 3$$

$$J^{-1} \frac{\delta \xi_2}{\delta x_2} = 1$$

Expanding equation (93) gives

$$S_1 = \frac{\delta}{\delta \xi_1} (J^{-1} \frac{\delta \xi_1}{\delta x_1}) + \frac{\delta}{\delta \xi_2} (J^{-1} \frac{\delta \xi_2}{\delta x_1}) + \frac{\delta}{\delta \xi_3} (J^{-1} \frac{\delta \xi_3}{\delta x_1}) \quad (99)$$

If central differencing is used, then the transformation yields

$$S_1 = \frac{\delta}{\delta \xi_1} \left( \frac{h}{2} \right) + \frac{1}{\xi_2^{j+1} - \xi_2^{j-1}} \left[ -\frac{1}{2} (\xi_2^{j+1} + 1) \left( \frac{\delta h}{\delta \xi_1} \right) \right]_{j+1} \\ + \frac{1}{2} (\xi_2^{j-1} + 1) \left( \frac{\delta h}{\delta \xi_1} \right) \Big|_{j-1} \quad (100)$$

By rearranging the right-hand-side of equation (100) and using the fact that  $\delta h / \delta \xi_1$  is not a function of  $\xi_2$ , it can be shown that

$$S_1 = 0$$

Similarly, it can be shown that if central differencing is used:

$$S_2 = \frac{\delta}{\delta \xi_1} (J^{-1} \frac{\delta \xi_1}{\delta x_2}) + \frac{\delta}{\delta \xi_2} (J^{-1} \frac{\delta \xi_2}{\delta x_2}) + \frac{\delta}{\delta \xi_3} (J^{-1} \frac{\delta \xi_3}{\delta x_2}) = 0 \quad (101)$$

and

$$S_3 = \frac{\delta}{\delta \xi_1} (J^{-1} \frac{\delta \xi_1}{\delta x_3}) + \frac{\delta}{\delta \xi_2} (J^{-1} \frac{\delta \xi_2}{\delta x_3}) + \frac{\delta}{\delta \xi_3} (J^{-1} \frac{\delta \xi_3}{\delta x_3}) = 0 \quad (102)$$

Thus, if central differencing is used, equation (93) will numerically conserve mass.

The condition for momentum conservation requires

$$\frac{\Delta J^{-1}}{\Delta \tau} + \frac{\delta}{\delta \xi_j} (J^{-1} \frac{\Delta \xi_j}{\Delta t}) = 0 \quad (103)$$

For the transformation, this can be expressed in the following difference formulation:

$$\begin{aligned}
& \frac{\Delta J^{-1}}{\Delta \tau} + \frac{\delta}{\delta \xi_j^{n+1}} [(J^{-1})^n \frac{\Delta \xi}{\Delta t}] \\
& = \frac{1}{2} \frac{\Delta h}{\Delta \tau} + \frac{\delta}{\delta \xi_2^{n+1}} \left[ \frac{h^n}{2} (2) \frac{x_2}{\Delta t} \left( \frac{1}{h^{n+1}} - \frac{1}{h^n} \right) \right] \\
& = \frac{1}{2} \frac{\Delta h}{\Delta \tau} - \frac{1}{h^{n+1}} \frac{\Delta h}{\Delta t} \frac{\delta x_2}{\delta \xi_2^{n+1}} = 0
\end{aligned} \tag{104}$$

Thus, if the time differencing is done in accordance with equation (104), equation (103) will be satisfied and momentum will be conserved.

### 6.6.3 Solution Algorithm

Since equation (87) has the same form as the equations used in Reference 9, the numerical method used in that reference is suggested as the one to use first. Thus, the pseudospectral method would be used in the  $\xi_1$  and  $\xi_3$  directions, and central differences would be used in the  $\xi_2$  direction. Time advancement would be made using a semi-implicit method wherein the backward-difference formula would be used for the time derivative of the velocities, the Crank-Nicholson method for the viscous and pressure terms and the Adams-Bashforth method for the remainder,  $H_i$  terms.

## 7. CONCLUDING REMARKS

A program for large-eddy simulation of turbulent flow in a channel was adapted to deal with time-varying wall motion through



the use of linearized boundary conditions. The code was applied to flow in channels with one wall having prescribed wavy motion, and to channels with a compliant wall.

A mixing-length analysis employing a linearized Stokes layer theory capable of qualitative prediction of the change in pressure gradient was developed and used to guide the selection of parameters for LES calculations. The results indicate that a small drag-reduction is possible under certain conditions of wall motion. The drag-reduction is the result of the creation of a Stokes-like layer whose Reynolds stress is opposite to that of the undisturbed flow. This decreases the turbulence production near the wall and reduces the pressure gradient needed to drive the flow.

Predictions using both the linear theory and LES indicate that much of the reduction in the energy required to drive the flow through the channel is offset by the work required to drive the wall against pressure and viscous stresses. The net effect appears to yield a small decrease in the energy required to drive the flow.

Estimates of the drag reduction obtained from the mixing length analysis are generally higher than those obtained from LES. However, the mixing length analysis provides a simple first estimate of the net drag reduction due to a wavy wall.

To resolve the rapid variation of the Reynolds stress near the moving wall a fine mesh is required. For this reason, the mesh was refined beyond that used in the plane channel; the changes were small.

The most significant effects of wall motion on the flow are found within a layer whose thickness is comparable to the viscous sublayer thickness. To validate the results obtained using the linearized conditions requires that the exact boundary conditions be applied at the actual wall location. This in turn requires transformation to a time-dependent coordinate system which renders the calculation much more complicated.

Calculations for compliant elastic walls coupled to the flow were unsuccessful in producing significant effects on the channel drag for material properties representative of existing foam or plastisol materials. The only surfaces which yielded a notable response were thin membranes under slight tension. The membranes developed low frequency, long wavelength surface shapes which did not interact with the flow to create drag reducing effects.

#### 8. ACKNOWLEDGMENTS

The work reported in this report was sponsored by the U.S. Office of Naval Research under Contract No. N00014-81-C-0506. Computer time was furnished by the Thermo- and Gas-Dynamics Division of the NASA/Ames Research Center. The assistance of Dr. N. Mansour in determining the requirements of numerical schemes for generalized equations is also gratefully acknowledged.

## REFERENCES

1. Kramer, M. O.: Boundary Layer Stabilization by Distributed Damping. A.S.N.E. Jour., Vol. 72, Feb. 1960, pp. 25-30.
2. Kramer, M. O.: Reduction of Drag of a Fast Underwater Body by Means of an Artificial Dolphin Skin. Jahrbuch 1960 der DGLR, pp. 102-110.
3. Benjamin, T. B.: Effects of a Flexible Boundary on Hydrodynamic Stability. Jour. of Fluid Mech., Vol. 9, Pt. 4, Dec. 1960, pp. 513-532.
4. Kendall, J. M.: The Turbulent Boundary Layer Over a Wall with Progressive Surface Waves. Jour. of Fluid Mech., Vol 41, Pt. 2, Apr. 1970, pp. 259-281.
5. Williams, J. E. F.: Reynolds Stress Near a Flexible Surface Responding to Unsteady Air Flow. Bolt Beranek and Newman, Inc. Rept. No. 1138, June 1964.
6. Blick, E. F.: The Theory of Skin Friction Reduction by a Compliant Coating in a Turbulent Boundary Layer. In Viscous Drag Reduction, C. Sinclair Wells, Ed., Plenum Press, 1969, pp. 409-425.
7. Thorsness, C.B., Morrisroe, P.E., and Hanratty, T.J.: A Comparison of Linear Theory with Measurements of the Variation of Shear Stress Along a Solid Wave, Chem. Engrg. Sci., Vol. 33, 1978, pp. 579-592.
8. Buckles, J., Hanratty, T.J., and Adrian R.J.: Turbulent Flow Over Large-Amplitude Wavy Surfaces, Journ. of Fluid Mech., Vol. 140, 1984, pp. 27-44.
9. Moin, P. and Kim, J.: Numerical Investigation of Turbulent Channel Flow. Jour. of Fluid Mech., Vol. 118, 1982, pp. 341-377.
10. Kreplin, H. and Eckelmann, M.: Behavior of the Three Fluctuating Velocity Components in the Wall Region of a Turbulent Channel Flow, Physics of Fluids, Vol. 22, 1979, pp. 1233-1239.
11. Norris, H. L., III and Reynolds, W. C.: Turbulent Channel Flow With a Moving Wavy Boundary. Stanford University Technical Rept. No. TF-7, 1975.

12. Hanratty, T.J., Abrams, J, and Frederick, K.A.: Flow Over Solid Wavy Surfaces, Structure of Turbulent Shear Flow IUTAM Symposium, Marseille 1982.
13. Kelleher, M.D. and Balasubramanian, R.: On the Use of Linearized Boundary Conditions in the Computation of Flow Over Wavy Walls ASME Symposium on Laminar and Turbulent Boundary Layers, FED. Vol 11, New Orleans, LA February 1984.
14. Kim, J. and Moin, P.: An Application of a Fractional Step Method to Incompressible Navier Stokes Equations, NASA TM-85898, March 1984.
15. Hussain, A. K. M. F. and Reynolds, W. C.: The Mechanics of an Organized Wave in Turbulent Shear Flow. Jour. of Fluid Mech., Vol. 41, Pt. 2, 1970, pp. 241-258.
16. White, F. M.: Viscous Fluid Flow. McGraw-Hill Book Co., New York, 1974, pp. 486-488.
17. Willmarth, W. W.: Pressure Fluctuations Beneath Turbulent Boundary Layers. Annual Review of Fluid Mechanics, Vol. 7, 1975, pp. 13-38.
18. Kuhn, G. D., Moin, P., Kim, J. J., and Ferziger, J. H.: Turbulent Flow in a Channel with a Wall with Progressive Waves. Presented at ASME Symposium on Laminar and Turbulent Boundary Layers. New Orleans, Louisiana, February 1984.
19. Yang, J. N. and Heller, R. A.: Random Vibration of Compliant Wall. Proceedings of the American Society of Civil Engineers (Jour. of Engrg. Mechanics Div.), Vol. 102, No. EM6, December 1976, pp. 1041-1057.
20. Achenbach, J. D.: Wave Propagation in Elastic Solids, American Elsevier Publishing Company, New York, 1973, pp. 202-261.
21. Duncan, J.H., and Hsu, C.C.: The Response of a Two-Layer Viscoelastic Coating to Pressure Disturbances from a Turbulent Boundary Layer, AIAA Paper No. 84-0535, Presented at AIAA 22nd Aerospace Sciences Meeting, January 9-12, 1984, Reno, Nevada.
22. Kalnins, A., and Evrensel, C.: Viscoelastic Slab Modeled by a One DOF System for low-frequency Response, Report to ONR Compliant Coating Drag Reduction Program Review, October 1983.

23. Walsh, M.J. and Lindemann, A.M.: Optimization and Application of Riblets for Turbulent Drag Reduction, AIAA Paper No. 84-0347, presented at AIAA 22nd Aerospace Sciences Meeting, January, 1984, Reno, Nevada.
24. Lax, R. D.: Weak Solutions of Nonlinear Hyperbolic Equations and Their Numerical Computation. Communications on Pure and Applied Mathematics, Vol. 7, 1954.
25. Viviand, H.: Conservation Forms of Gas Dynamic Equations. La Recherche Aerospatiale, No. 1, Jan.-Feb. 1974.
26. Vinokur, M.: Conservation Equations of Gasdynamics in Curvilinear Coordinate Systems. Jour. of Computational Physics, Vol. 14, No. 2, Feb. 1974.
27. Mansour, N.N., Ferziger, J.H., and Reynolds, W.C.: Large-Eddy Simulation of a Turbulent Mixing Layer, Report No. TF-11, Thermosciences Div., Dept. of Mechanical Engineering, Stanford University, April 1978.

Change in  $-dP/dx$

CASE	$\eta_o^+$	$\lambda^+$	$c/U_m$	$\theta$	Eq. (34)	LES	LES	$\frac{C_{DP}}{C_D}$ (Theory)	$\frac{C_{DP}}{C_D}$ (LES)
						Coarse Mesh	Fine Mesh		
1	5	200	0.78	0	-0.076	-0.050	-0.035	0.039	0.014
2	5	200	-0.78	0	-0.214	-0.200	-0.173	0.104	0.111
3	5	50	0.78	90	-0.219	-0.100		0	
4	5	200	-1.10	0	-0.267	0	-0.192	0.132	0.126

TABLE 1

Effects of a Wall with Progressive Waves

$$\rho = 1000 \text{ kg/m}^3$$

$$u_{\tau} = .051 \text{ m/sec}$$

$$\bar{\delta} = .0127 \text{ m}$$

$$\frac{u_{\tau} \bar{\delta}}{\nu} = 640$$

$$\rho_1^* = 1025 \text{ kg/m}^3$$

$$\rho_3^* = 1394 \text{ kg/m}^3$$

$$h_1^* = .025 \text{ mm}$$

$$h_3^* = 20 \text{ mm}$$

**TABLE 2**

Parameters of a compliant wall composed of a mylar sheet over a PVC foam substrate on a stiff backing plate.

Coordinate	Label	Length	No. of Grid Points
$x_1$	a	$2\pi$	64
$x_2$		2	64,102
$x_3$	b	$2\pi$	128

$x_2$  Grid Distribution  
(Lower Half of Symmetric Channel)

Coarse Mesh			Fine Mesh		
Point	$x_2$	$y_w^+$	Point	$x_2$	$y_w^+$
2	-0.9972	1.78	2	-0.9997	0.20
3	-0.9940	3.85	3	-0.9990	0.64
4	-0.9902	6.26	4	-0.9982	1.13
5	-0.9858	9.06	5	-0.9974	1.68
6	-0.9808	12.30	6	-0.9964	2.30
7	-0.9749	16.10	7	-0.9953	3.00
8	-0.9680	20.50	8	-0.9941	3.78
9	-0.9601	25.50	9	-0.9927	4.67
10	-0.9510	31.40	10	-0.9912	5.66
11	-0.9404	38.20	11	-0.9894	6.79
12	-0.9287	46.00	12	-0.9874	8.05
13	-0.9141	55.00	13	-0.9852	9.47
14	-0.8980	65.30	14	-0.9827	11.10
15	-0.8795	77.20	15	-0.9799	12.90
16	-0.8583	90.70	16	-0.9768	14.90
17	-0.8342	106.00	17	-0.9732	17.10
18	-0.8069	124.00	18	-0.9693	19.70
19	-0.7760	143.00	19	-0.9648	22.50
20	-0.7412	166.00	20	-0.9598	25.70
21	-0.7023	191.00	21	-0.9542	29.30
22	-0.6590	218.00	22	-0.9479	33.40
23	-0.6112	249.00	23	-0.9409	37.90
24	-0.5587	283.00	24	-0.9330	42.90
25	-0.5016	319.00	25	-0.9242	48.50
26	-0.4400	359.00	26	-0.9144	54.80
27	-0.3741	401.00	27	-0.9034	61.80
28	-0.3044	445.00	28	-0.8912	69.60
29	-0.2314	492.00	29	-0.8777	78.30
30	-0.1558	541.00	30	-0.8626	88.00
31	-0.0783	590.00	31	-0.8459	98.60
32	-0.0000	640.00	32	-0.8275	110.00
			33	-0.8071	123.00
			34	-0.7847	138.00
			35	-0.7601	154.00
			36	-0.7332	171.00
			37	-0.7038	190.00
			38	-0.6718	210.00
			39	-0.6372	232.00
			40	-0.5998	256.00
			41	-0.5597	282.00
			42	-0.5168	309.00
			43	-0.4712	339.00
			44	-0.4230	369.00
			45	-0.3723	402.00
			47	-0.2643	471.00
			48	-0.2075	507.00
			49	-0.1492	545.00
			50	-0.0900	583.00
			51	-0.0301	621.00

Table 3  
Details of the Computational Domain



CASE	$\bar{K}_3$	$\bar{C}_3$	$\bar{D}_1$	$\bar{N}_x$	$\bar{N}_z$	$\bar{M}_1$
1	1514	.098	1.58	9082	9082	.7795
2	70,600	0	15.37	0	0	.7795
3	0	0	0	10	10	.051
4	0	0	0	100	100	.051

TABLE 4

Parameters of Compliant Surfaces

$n_x$	$n_z$	$\omega$	$T_C$
1	0	22.14	.2838
2	0	44.28	.1419
1	1	49.51	.1269
2	1	62.64	.1003
1	2	91.33	.0688
2	2	98.95	.0635

TABLE 5

Frequencies and characteristic times  
of a rectangular membrane

AD-A149 283

LARGE EDDY SIMULATION OF TURBULENT FLOW IN CHANNELS  
WITH WAVY WALLS INCL. (U) NIELSEN ENGINEERING AND  
RESEARCH INC MOUNTAIN VIEW CA G D KUHN ET AL. JUL 84  
NEAR-TR-325 N00014-81-C-0506

2/2

UNCLASSIFIED

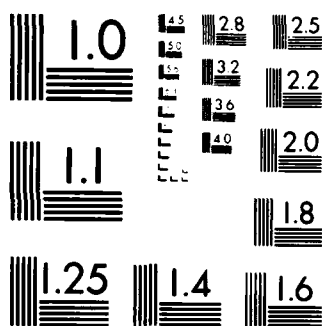
F/G 20/4

NL

END

FILMED

DTIC



MICROCOPY RESOLUTION TEST CHART  
NATIONAL BUREAU OF STANDARDS 1963-A

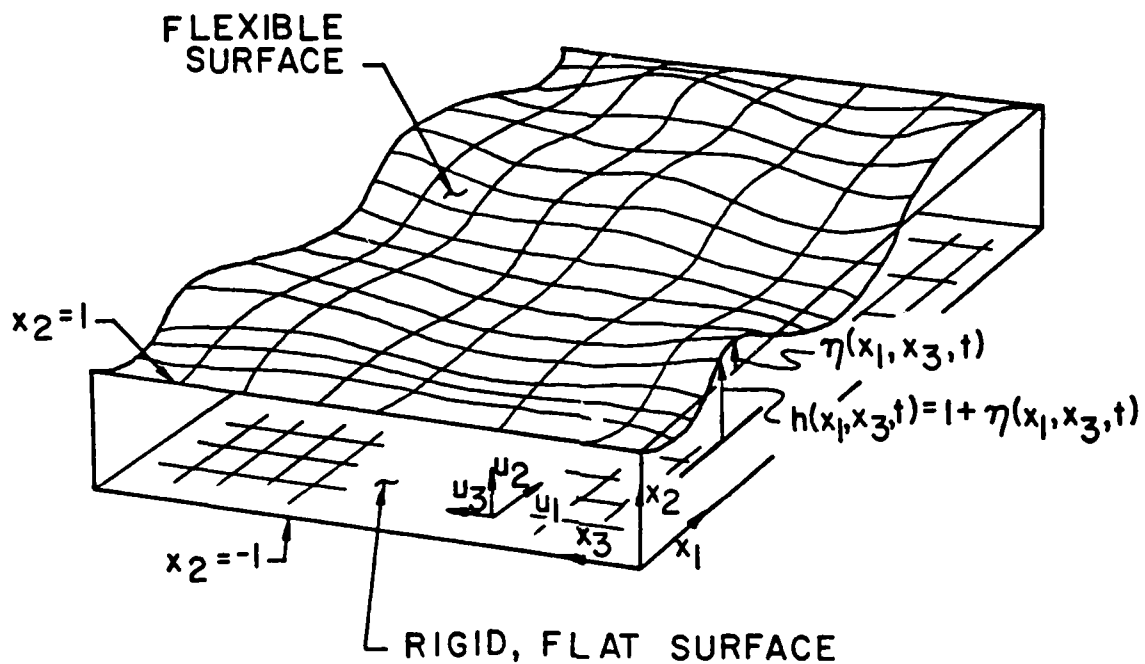


Figure 1.- Coordinates and velocity components for a channel with one wavy wall.

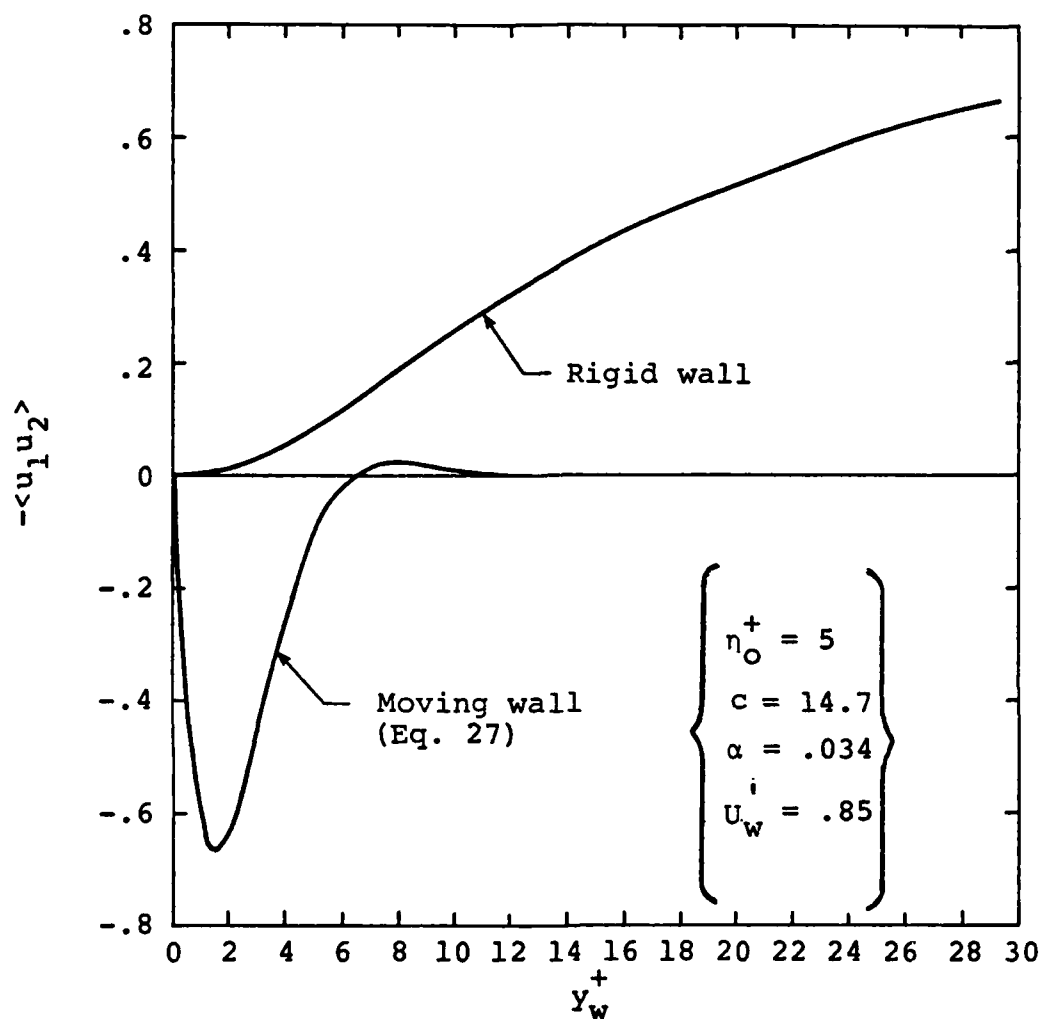


Figure 2.- Comparison of Reynolds stress from Stokes layer solution with that for turbulent flow near a rigid wall.

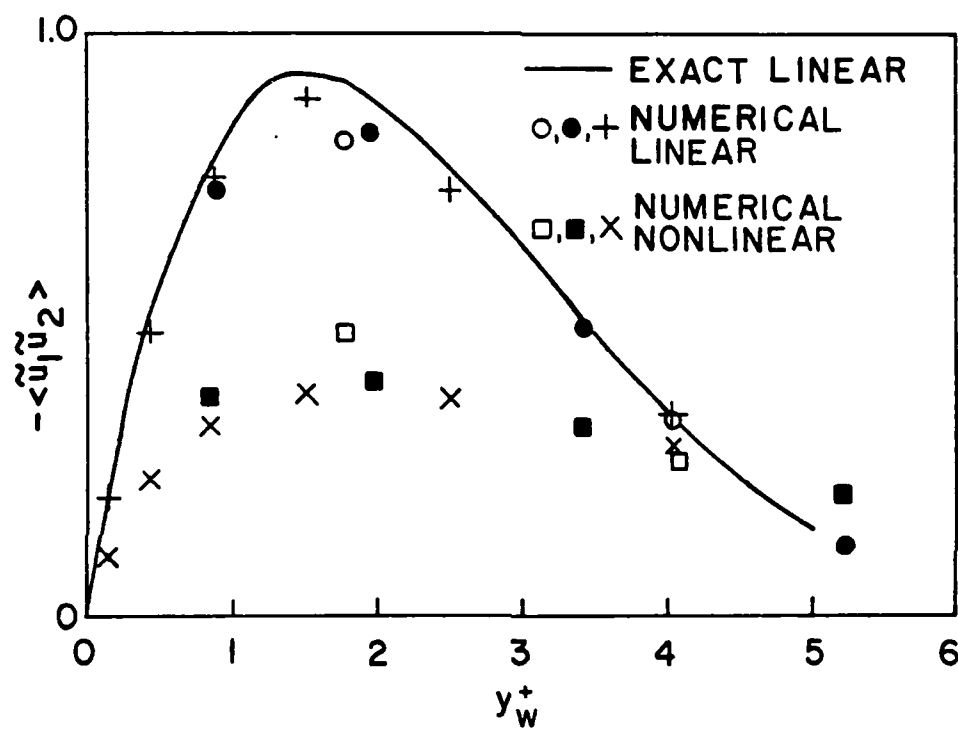


Figure 3.- Comparison of linear and nonlinear solutions for Stokes layer.

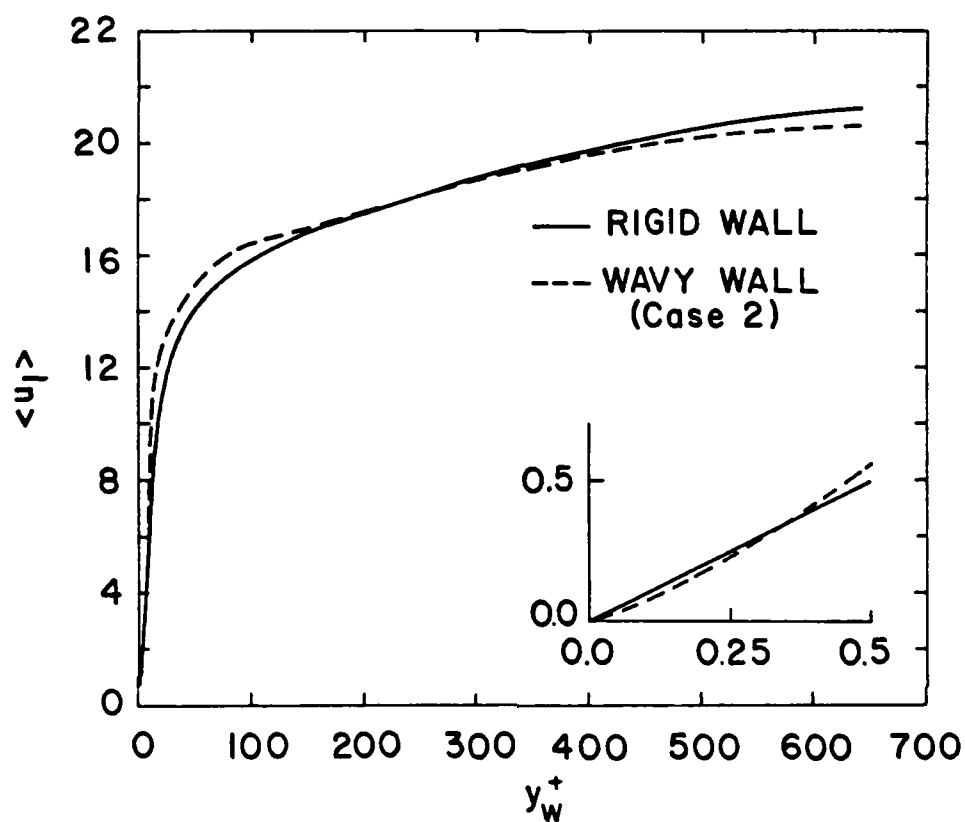


Figure 4.- Effect of wall motion on mean velocity profile in channel.



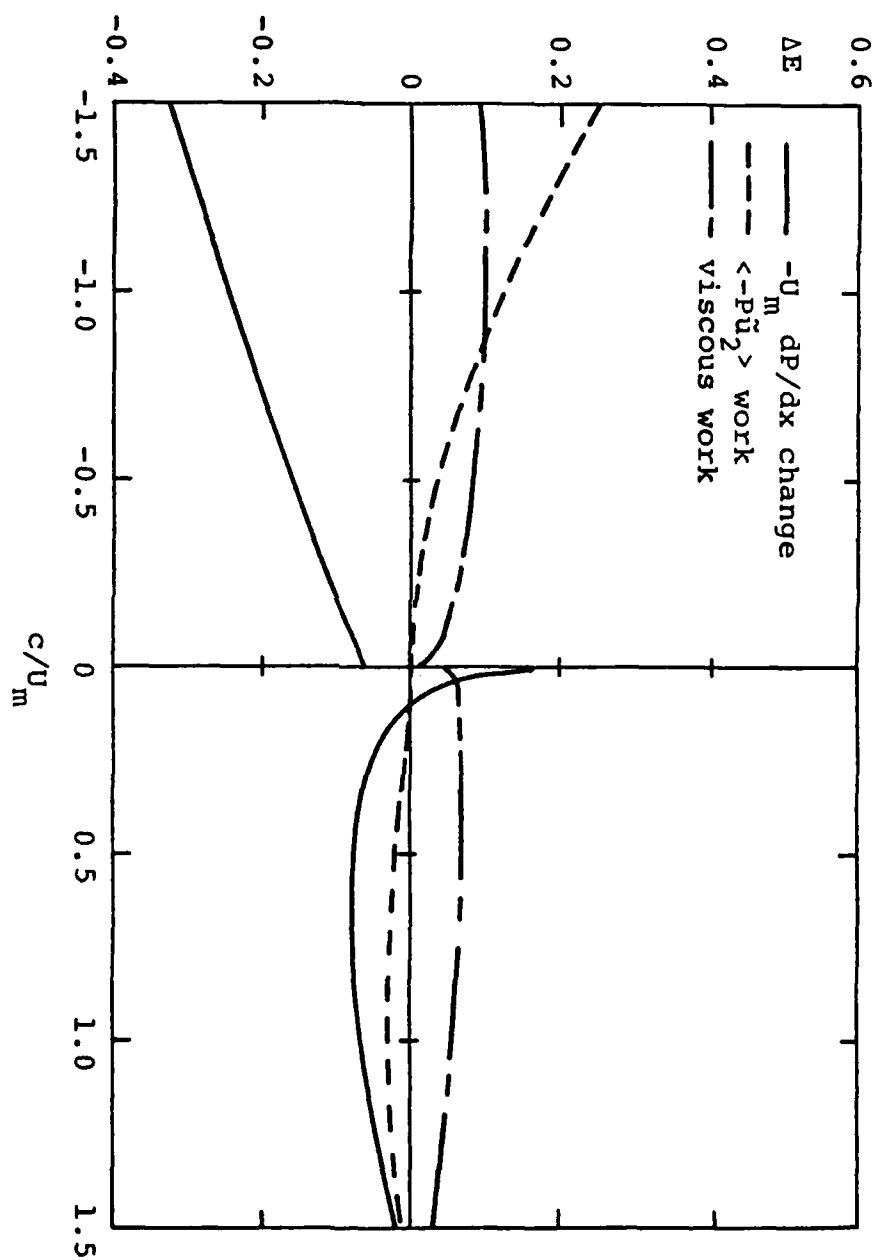


Figure 5.- Components of energy balance from linear theory.

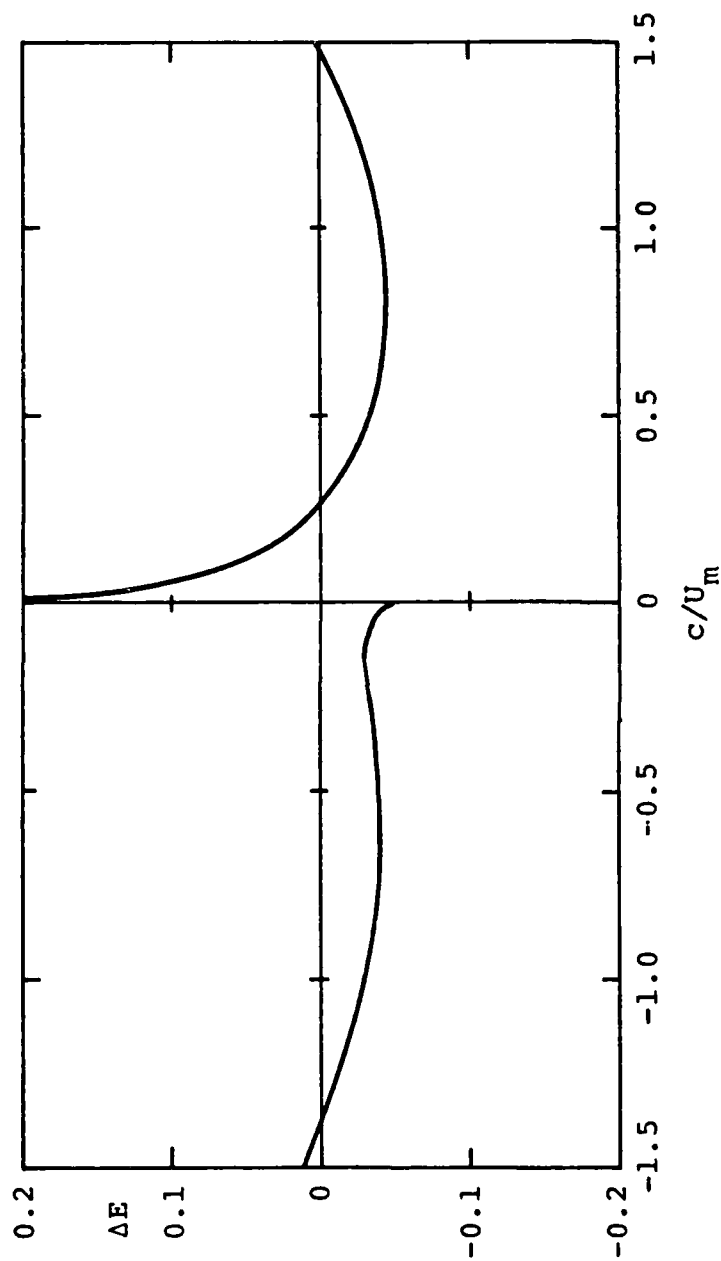


Figure 6.- Net change in energy required to drive flow through channel  
in response to Stokes layer from linear theory.

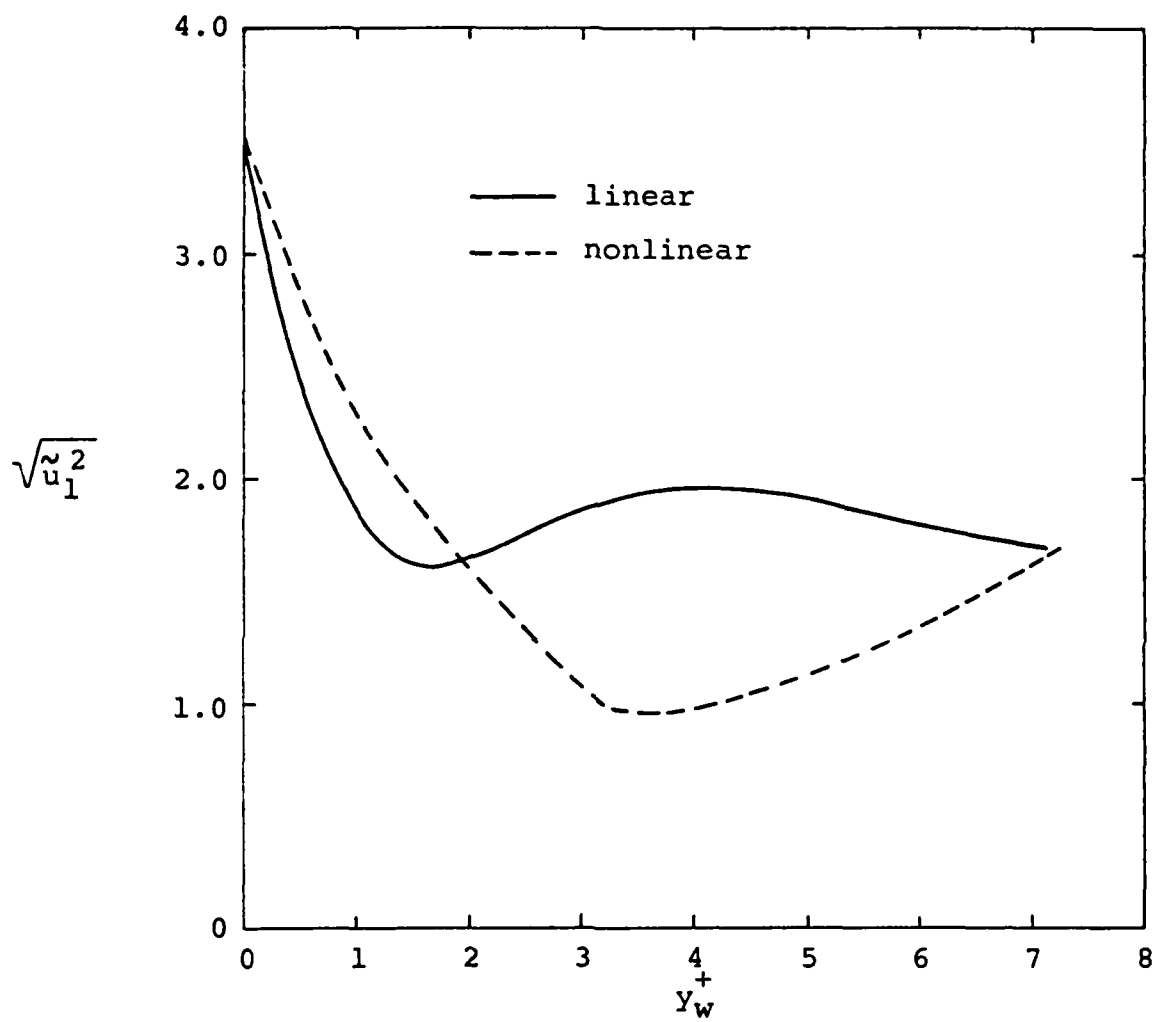
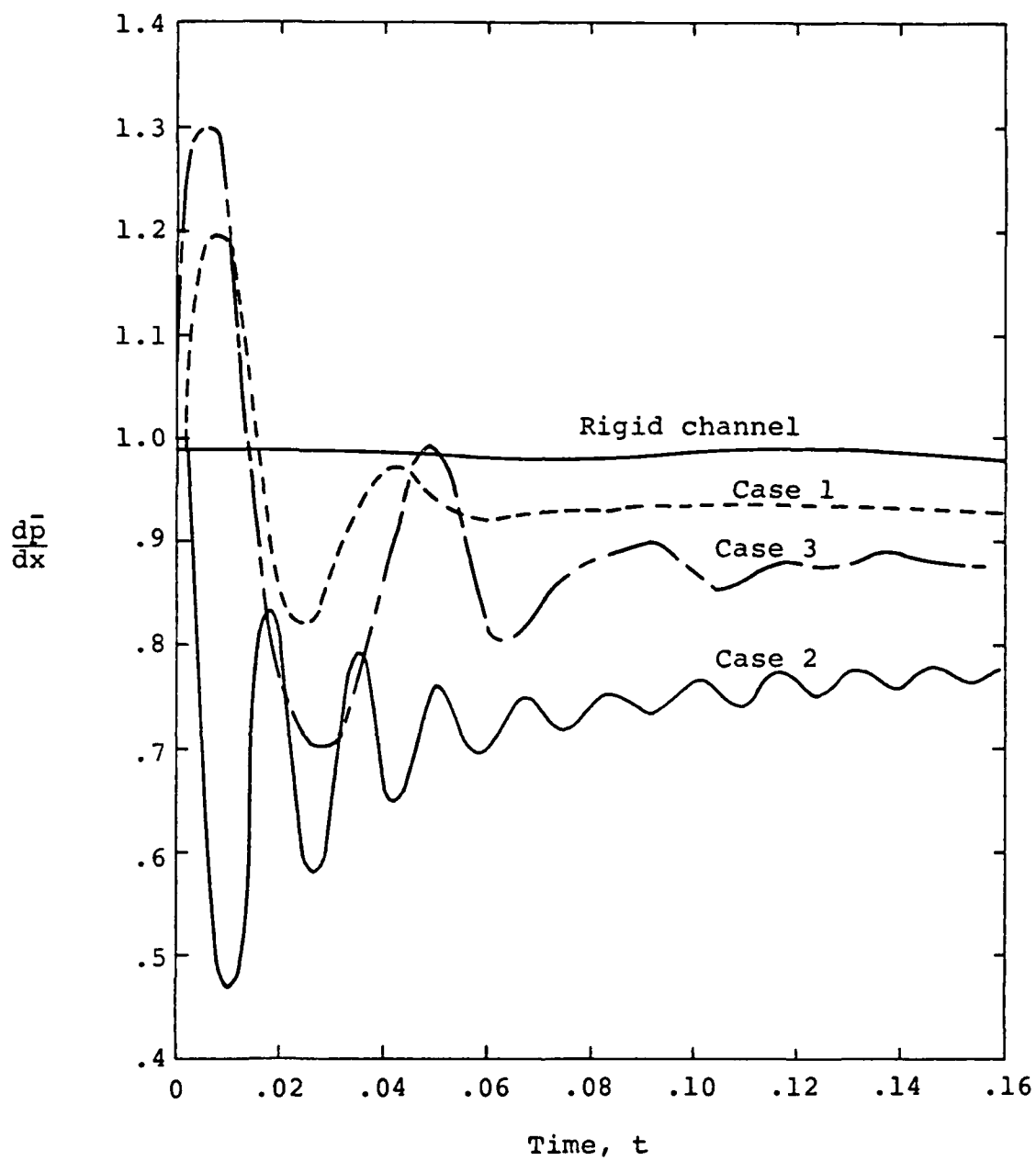
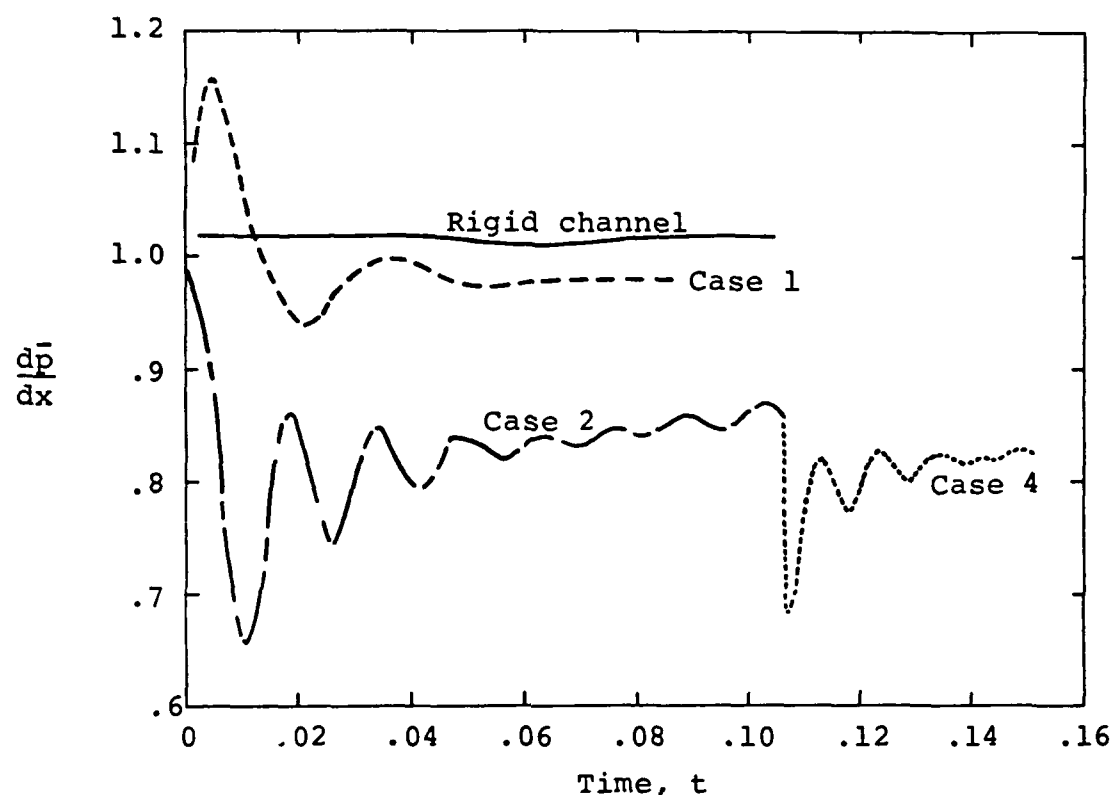


Figure 7.- Comparison of variation of rms  $u_1$  component for flow near the moving wall from linear and nonlinear Stokes analysis.



(a) Coarse mesh LES

Figure 8.- Pressure gradient in turbulent channel.



(b) Fine mesh LES  
Figure 8.- Concluded.

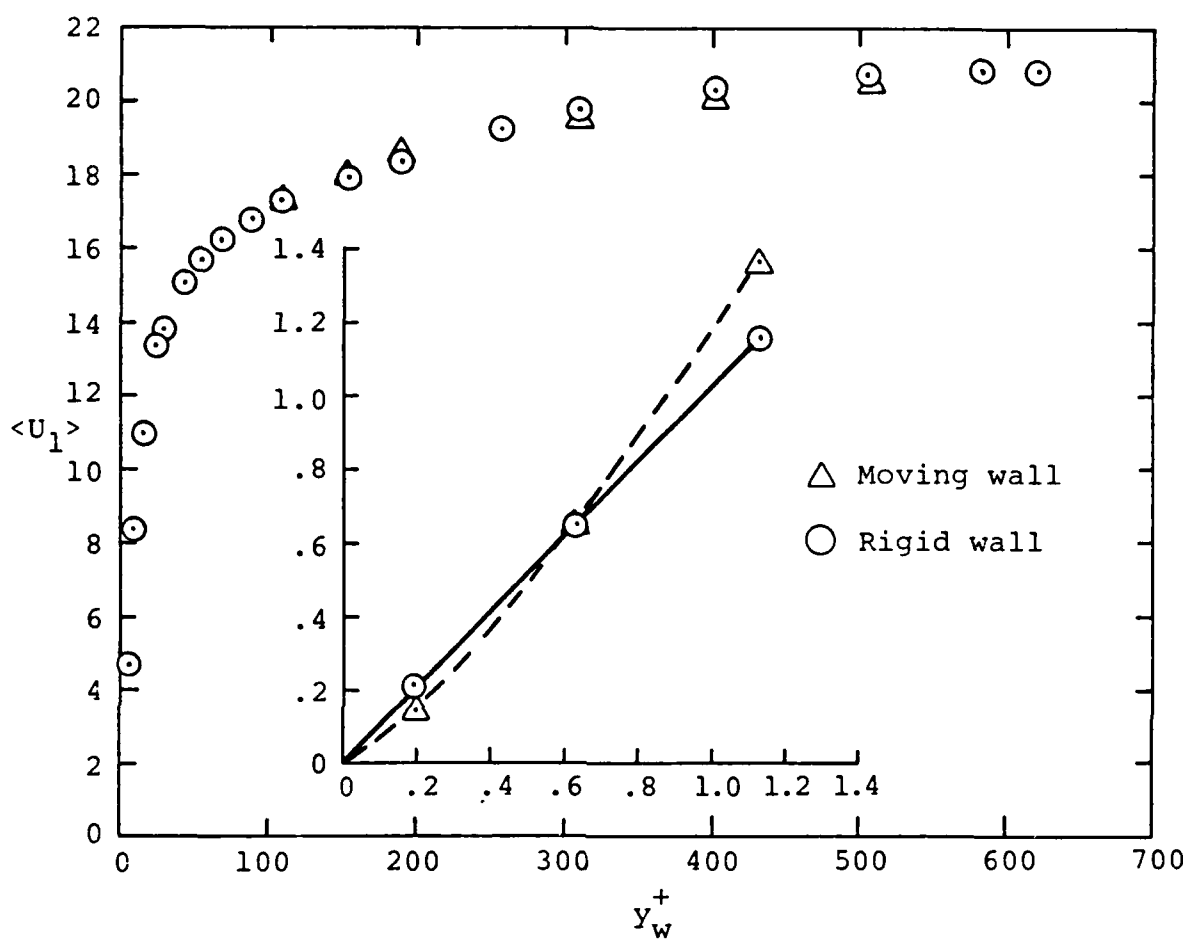


Figure 9.- Effect of wall motion on mean velocity profile in channel from LES.

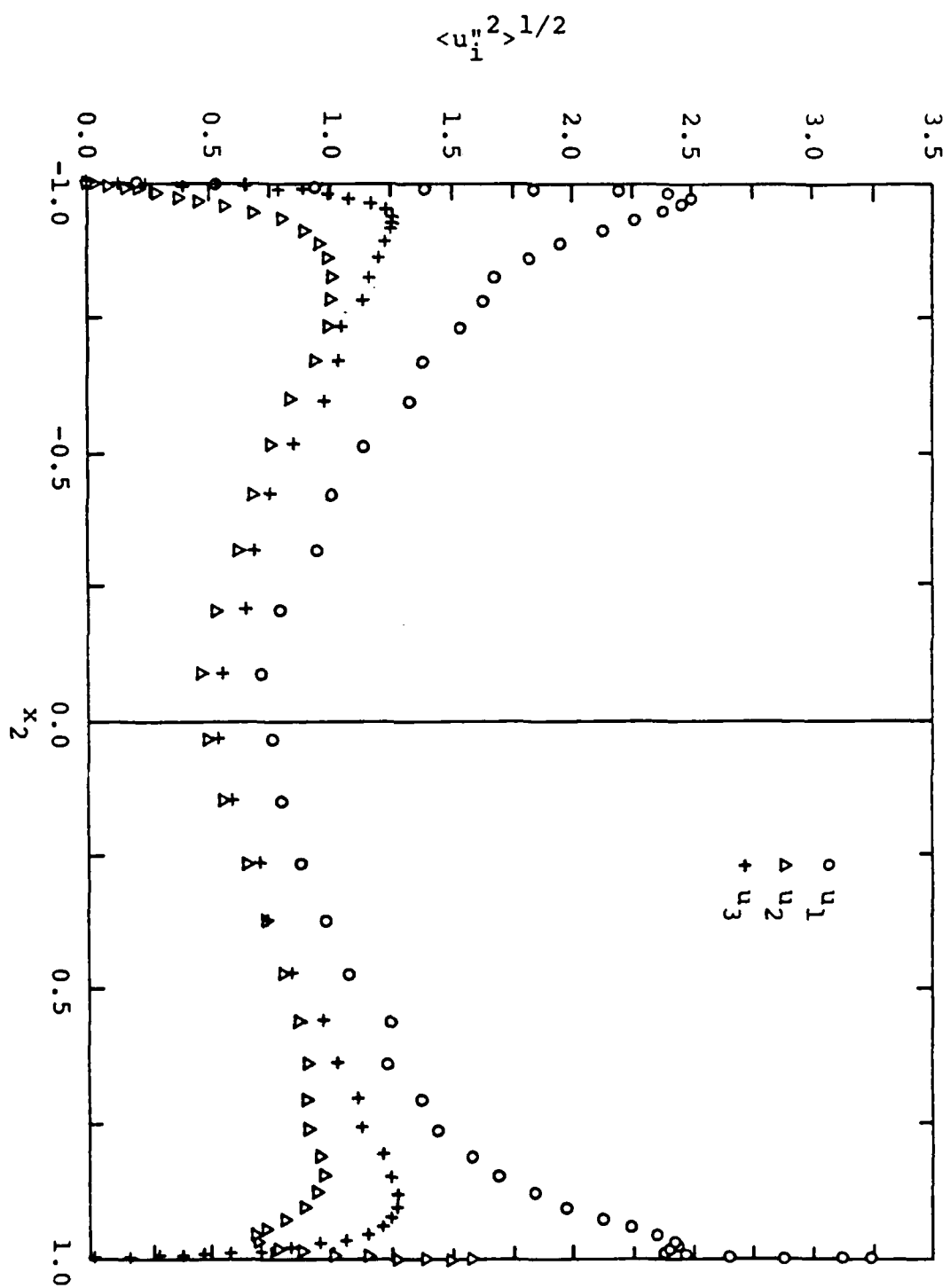
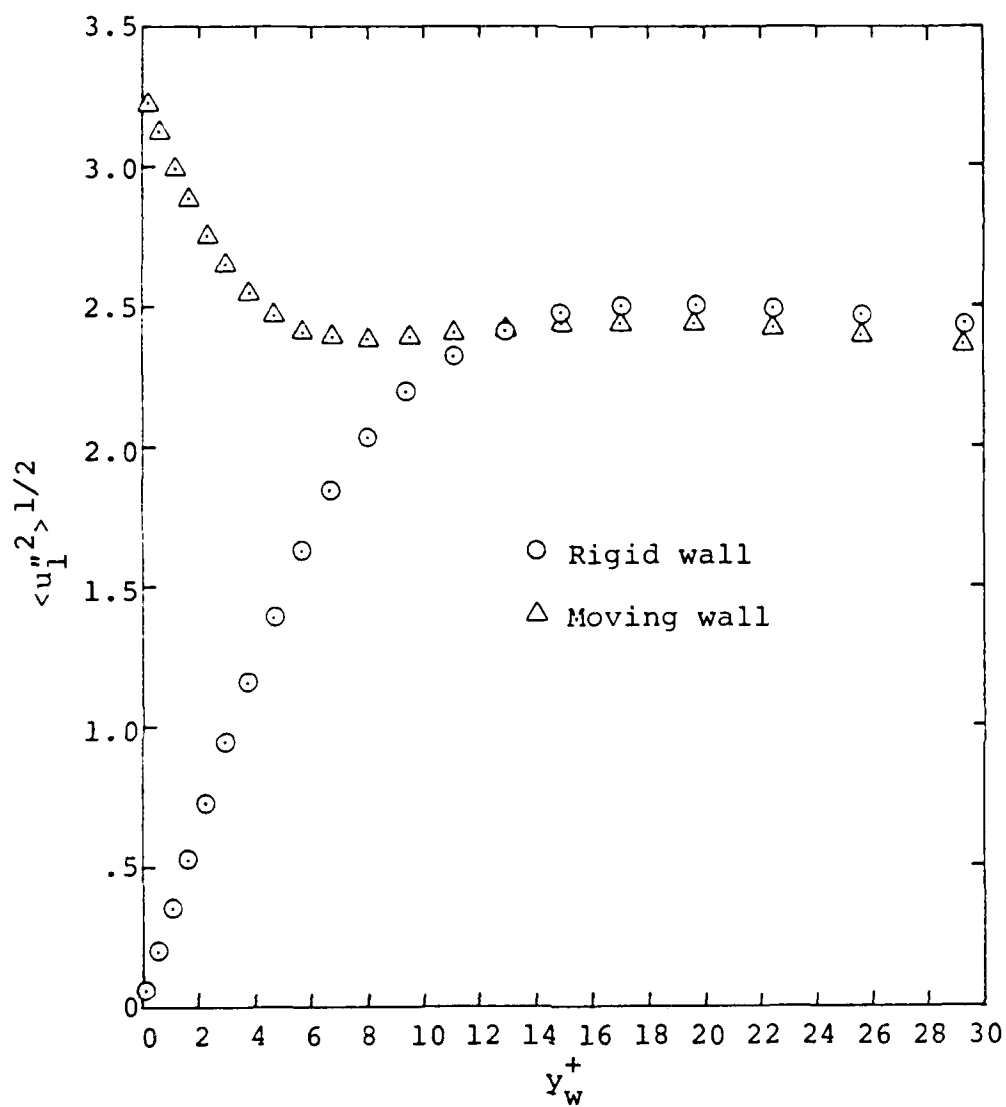


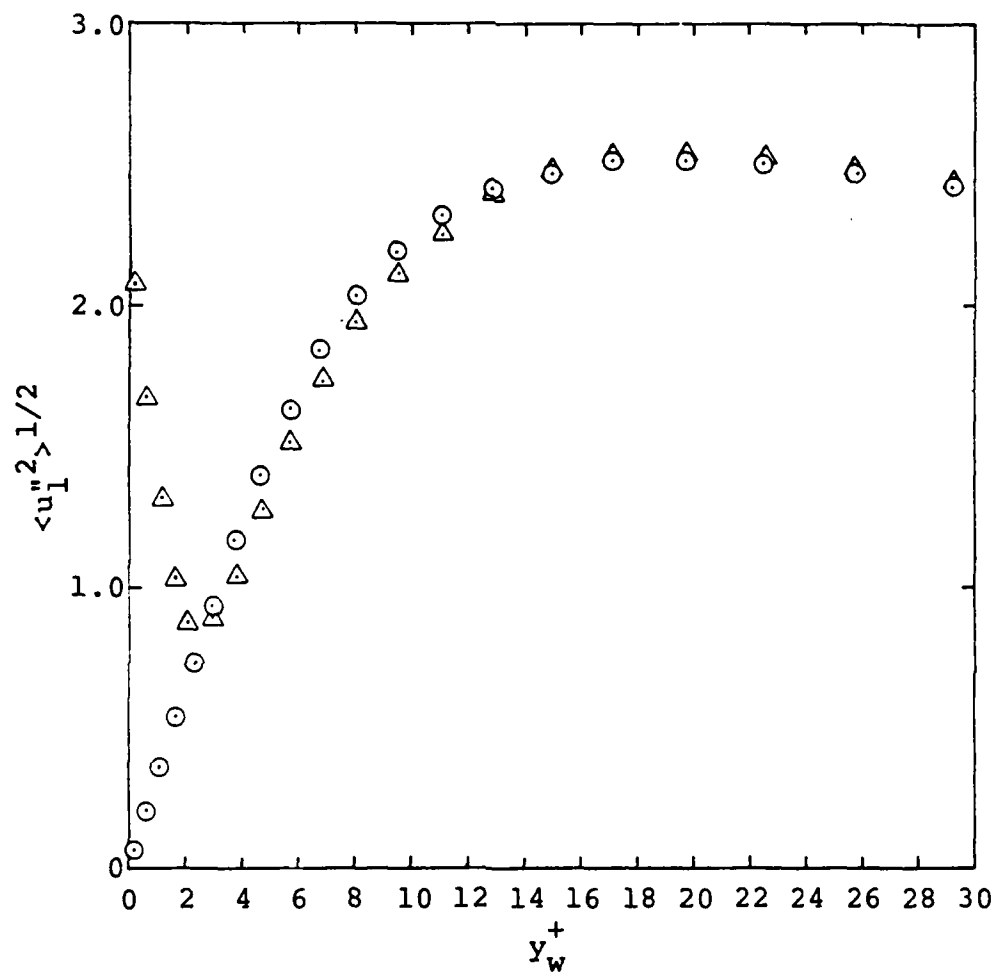
Figure 10.- Turbulence intensities in a channel with prescribed sinusoidal wall motion (case 1).



(a) Case 1

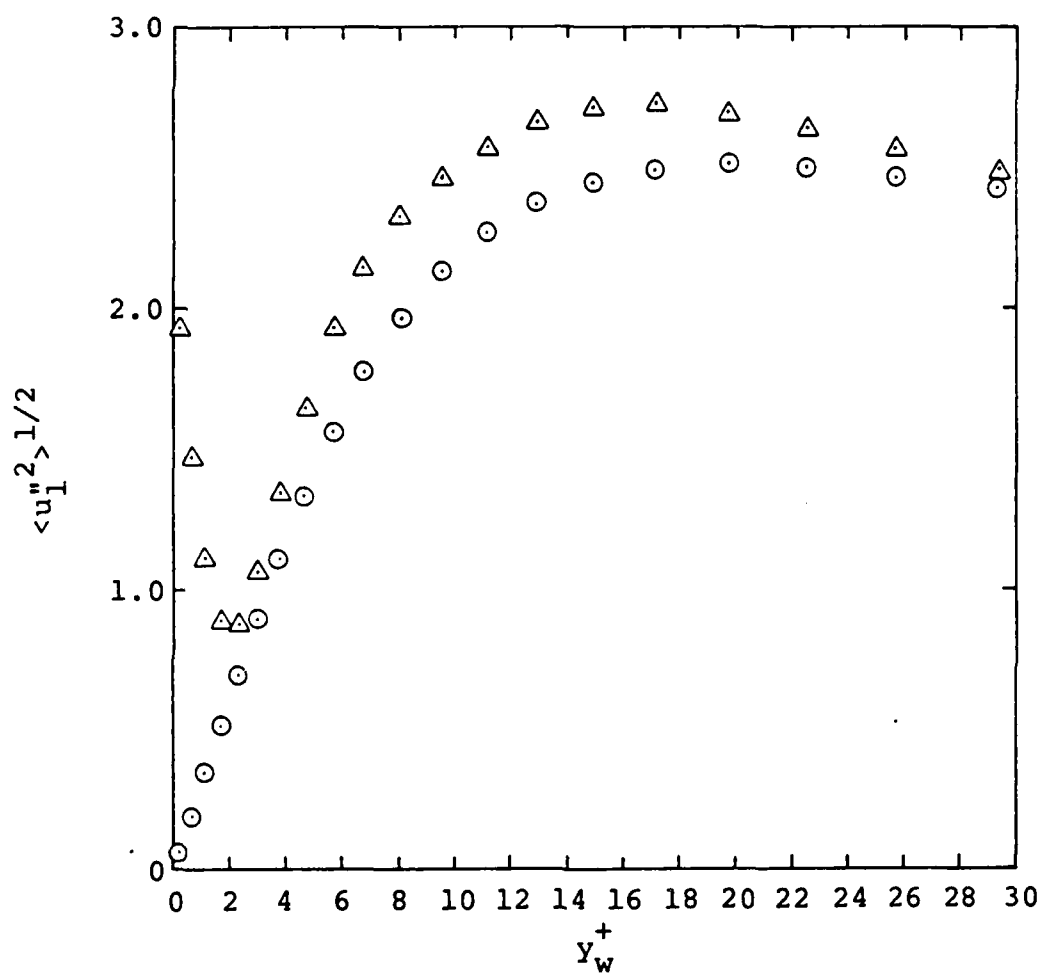
Figure 11.- Turbulence intensities in a channel with prescribed sinusoidal wall motion.





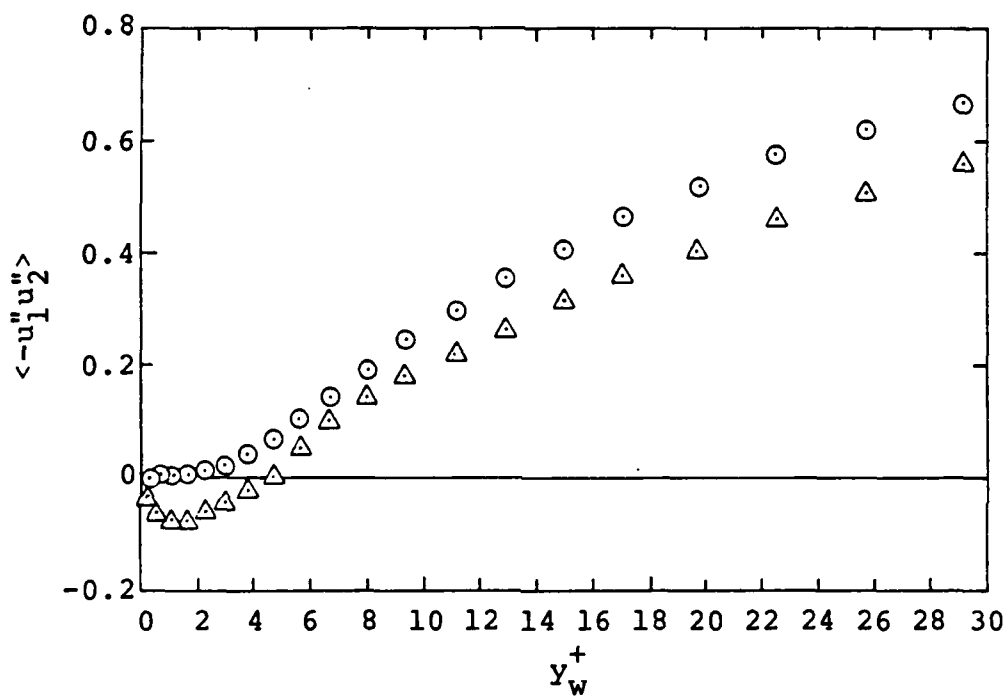
(b) Case 2

Figure 11.- Continued.



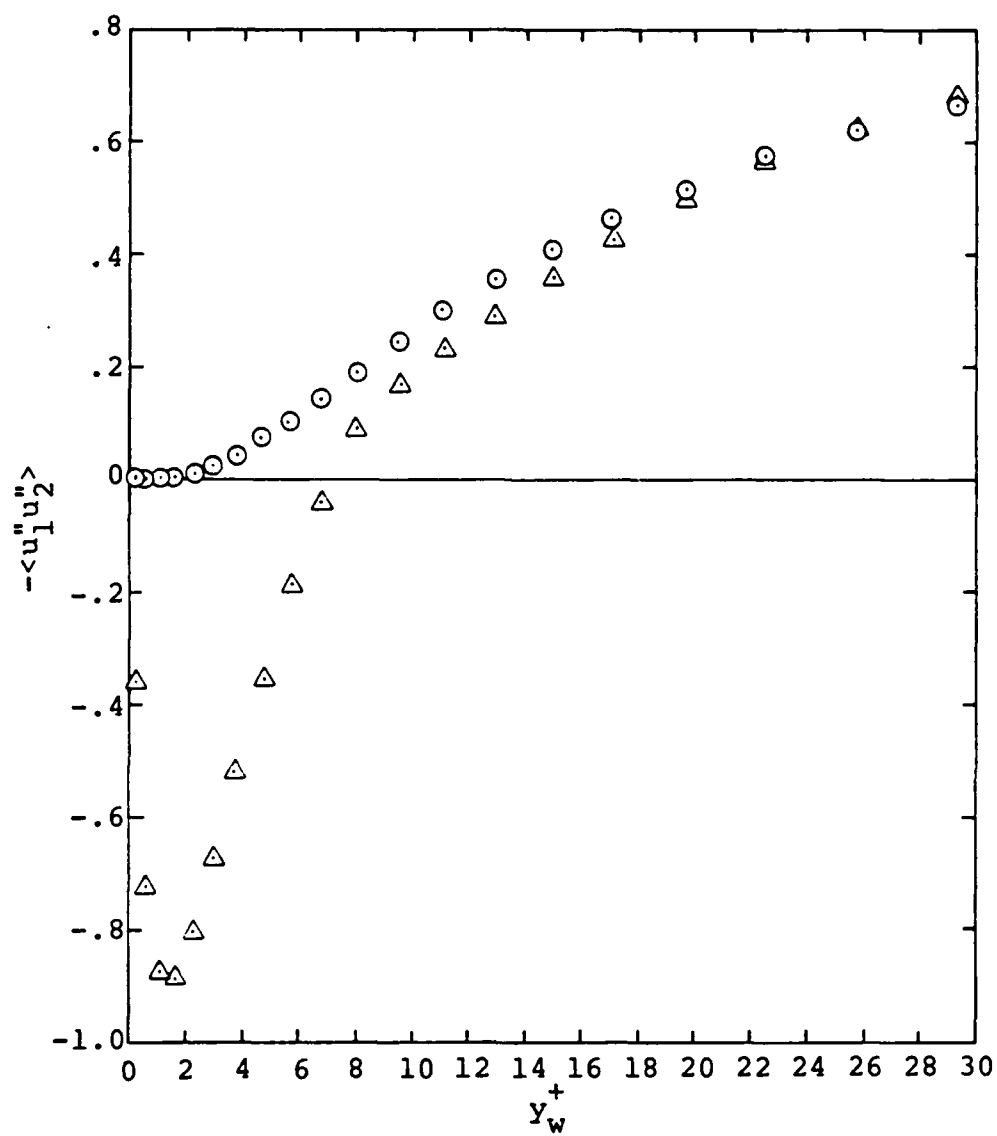
(c) Case 5

Figure 11.- Concluded.



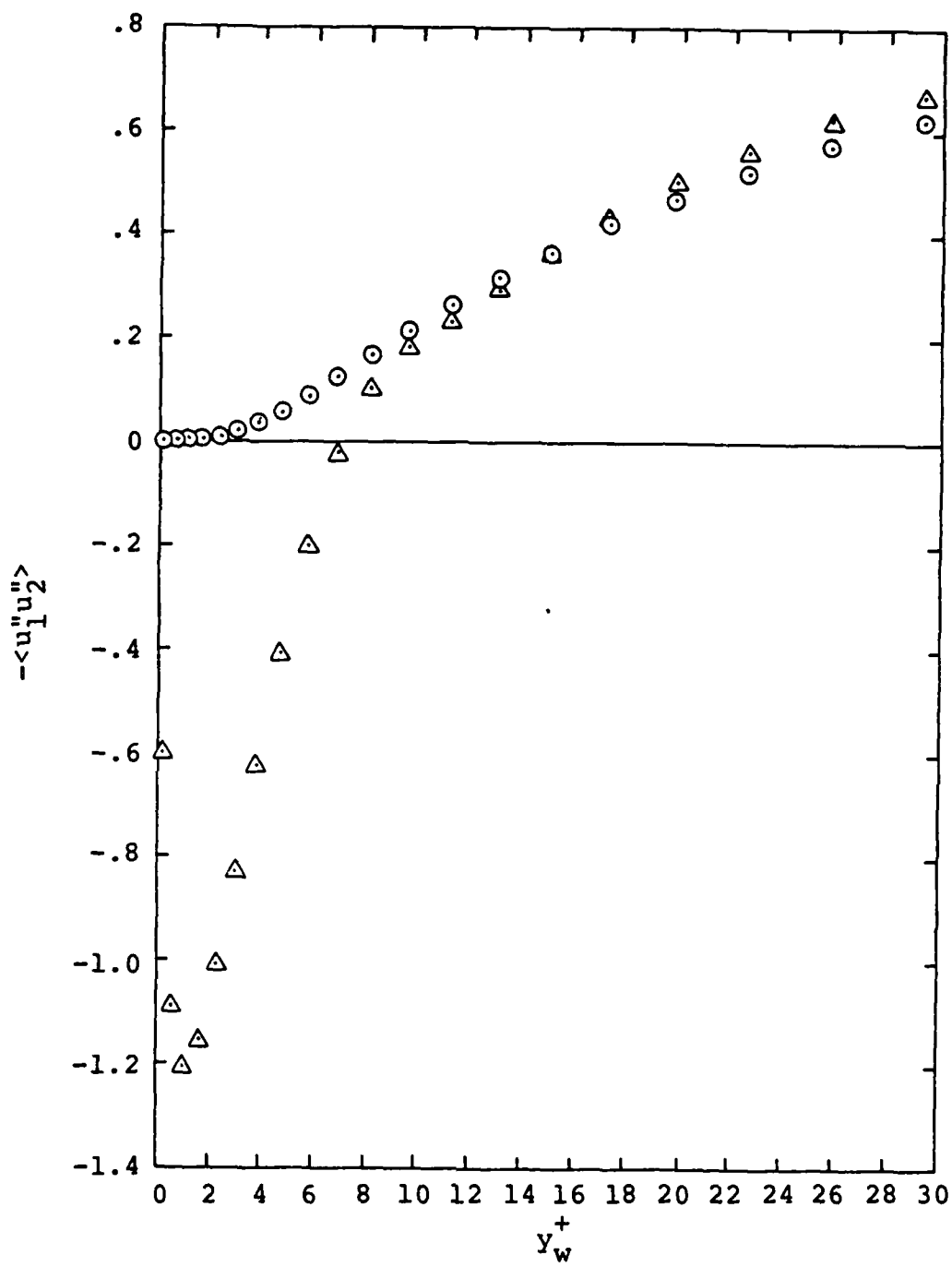
(a) Case 1 (Fine mesh)

Figure 12.- Comparison of turbulent shear stress for rigid and wavy walls.



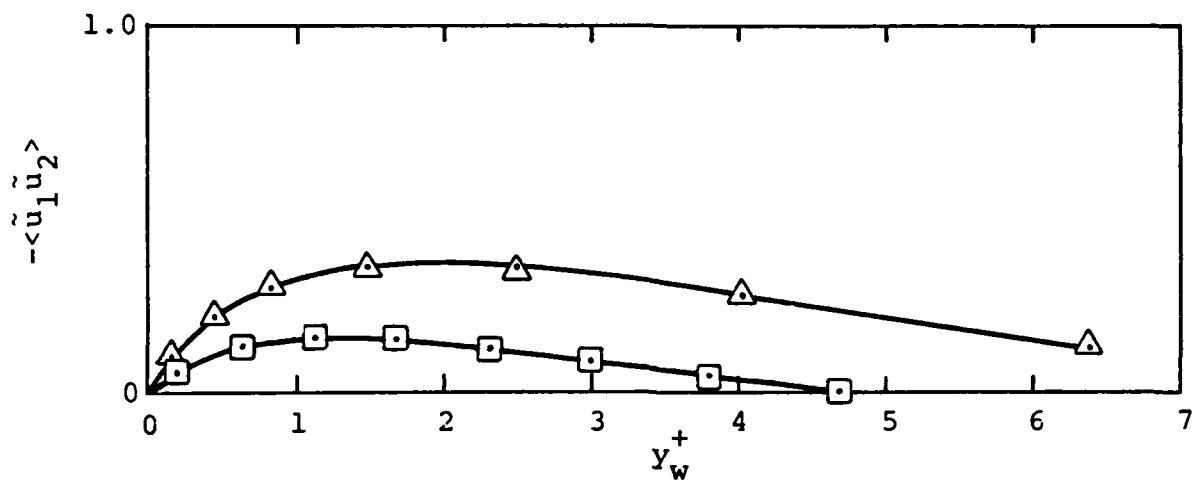
(b) Case 2

Figure 12.- Continued.

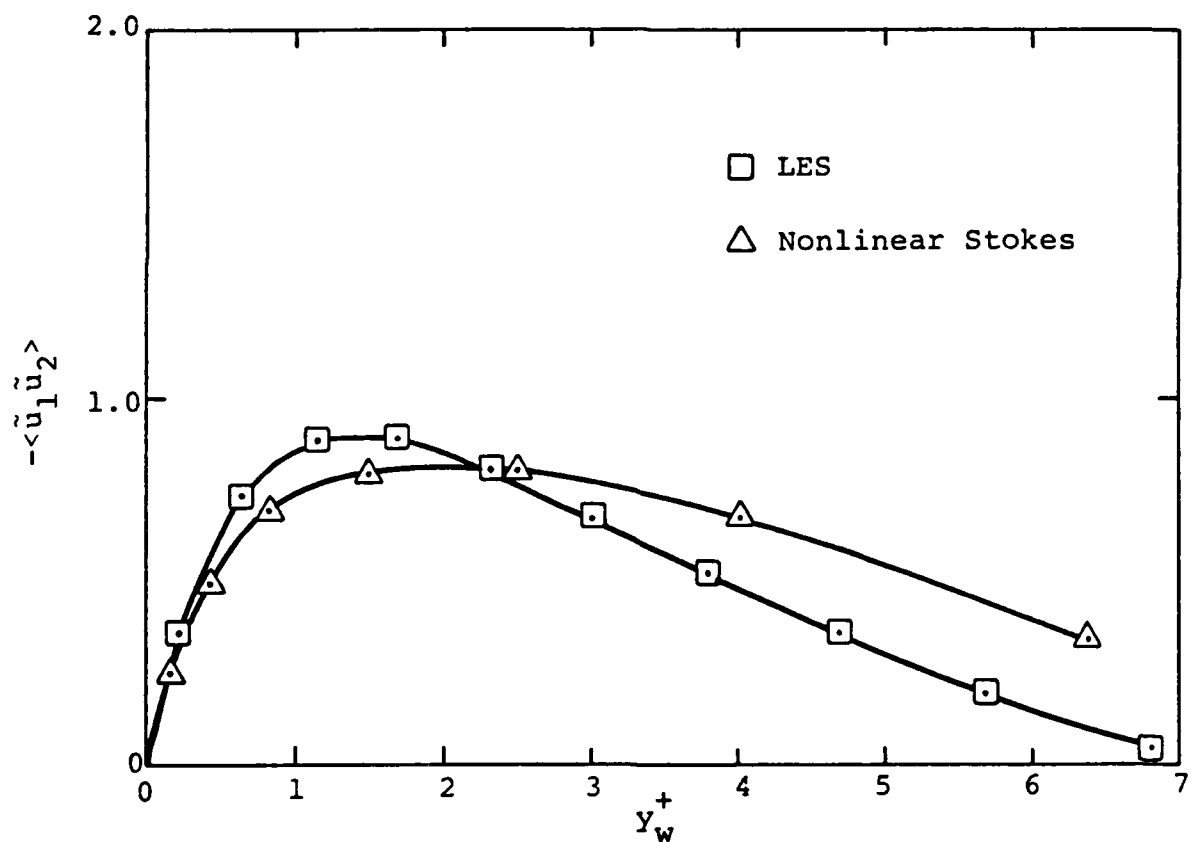


(c) Case 5

Figure 12.- Concluded.

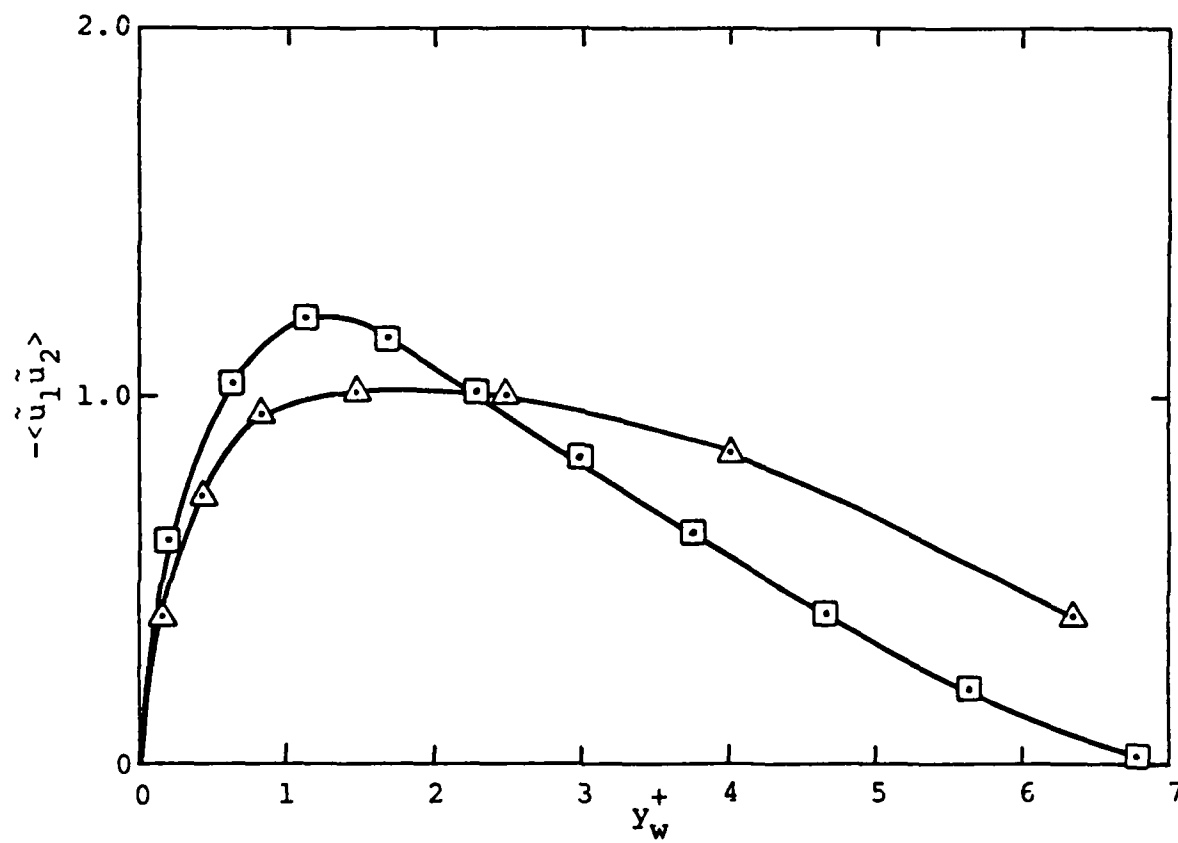


(a) Case 1



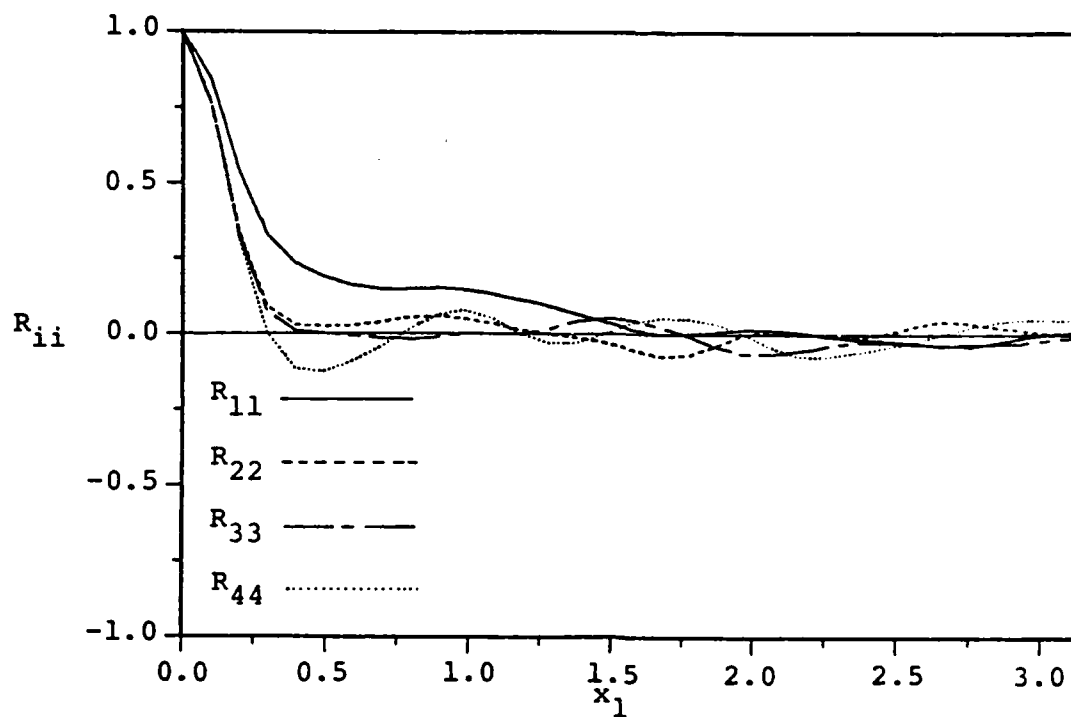
(b) Case 2

Figure 13.- Comparison of near-wall Reynolds stress from LES and nonlinear Stokes layer solution.

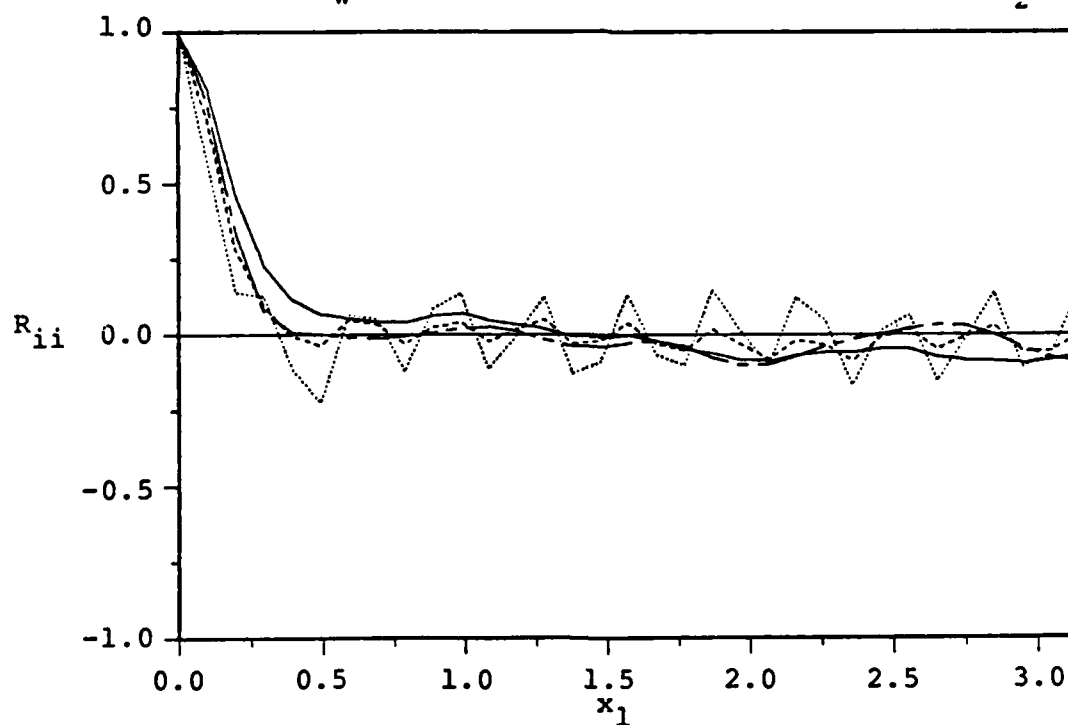


(c) Case 5

Figure 13.- Concluded.



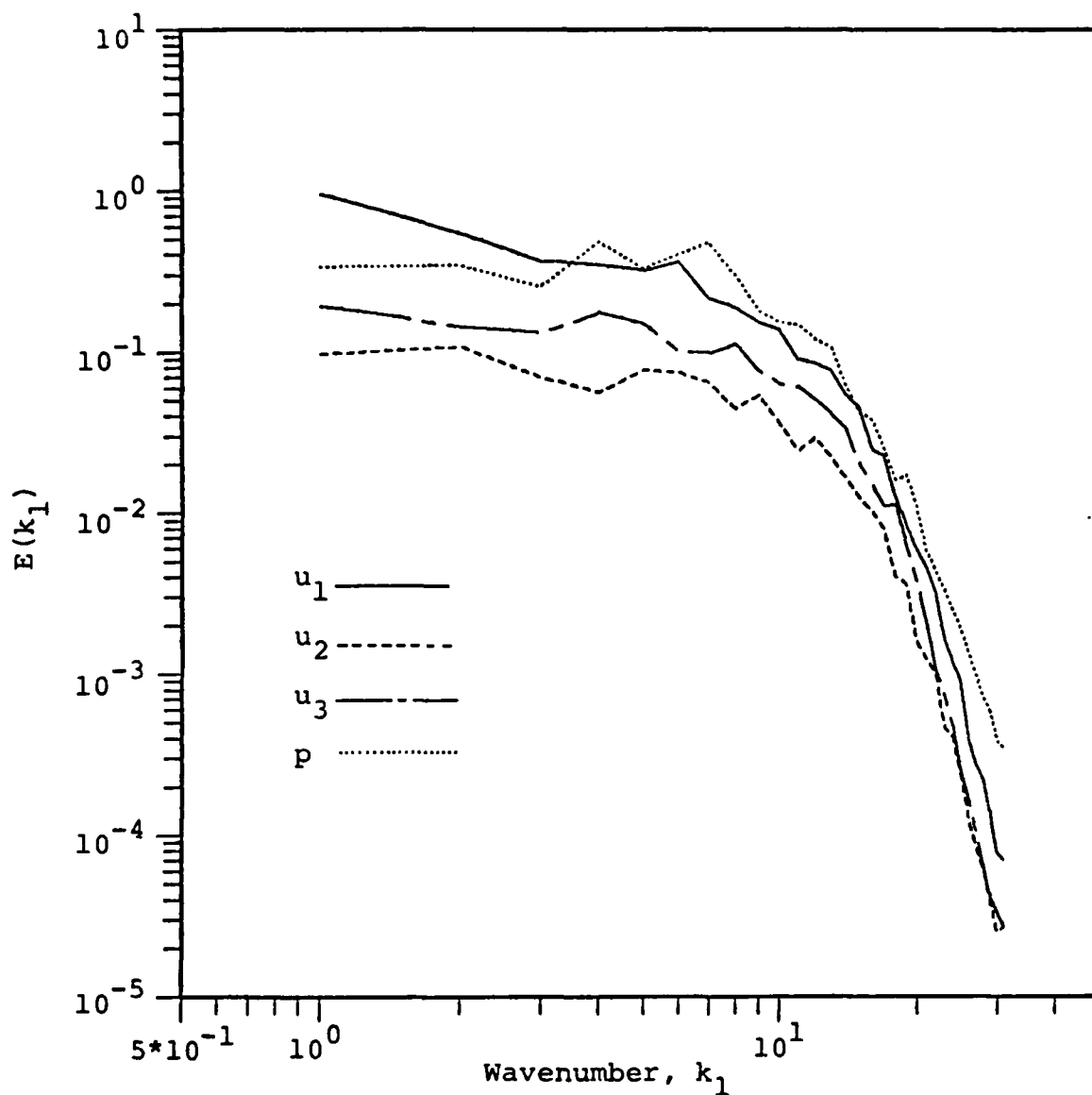
(a)  $y_w^+ \approx 55$  measured from the rigid wall ( $x_2 = -.914$ )



(b)  $y_w^+ \approx 55$  measured from the moving wall ( $x_2 = +.914$ )

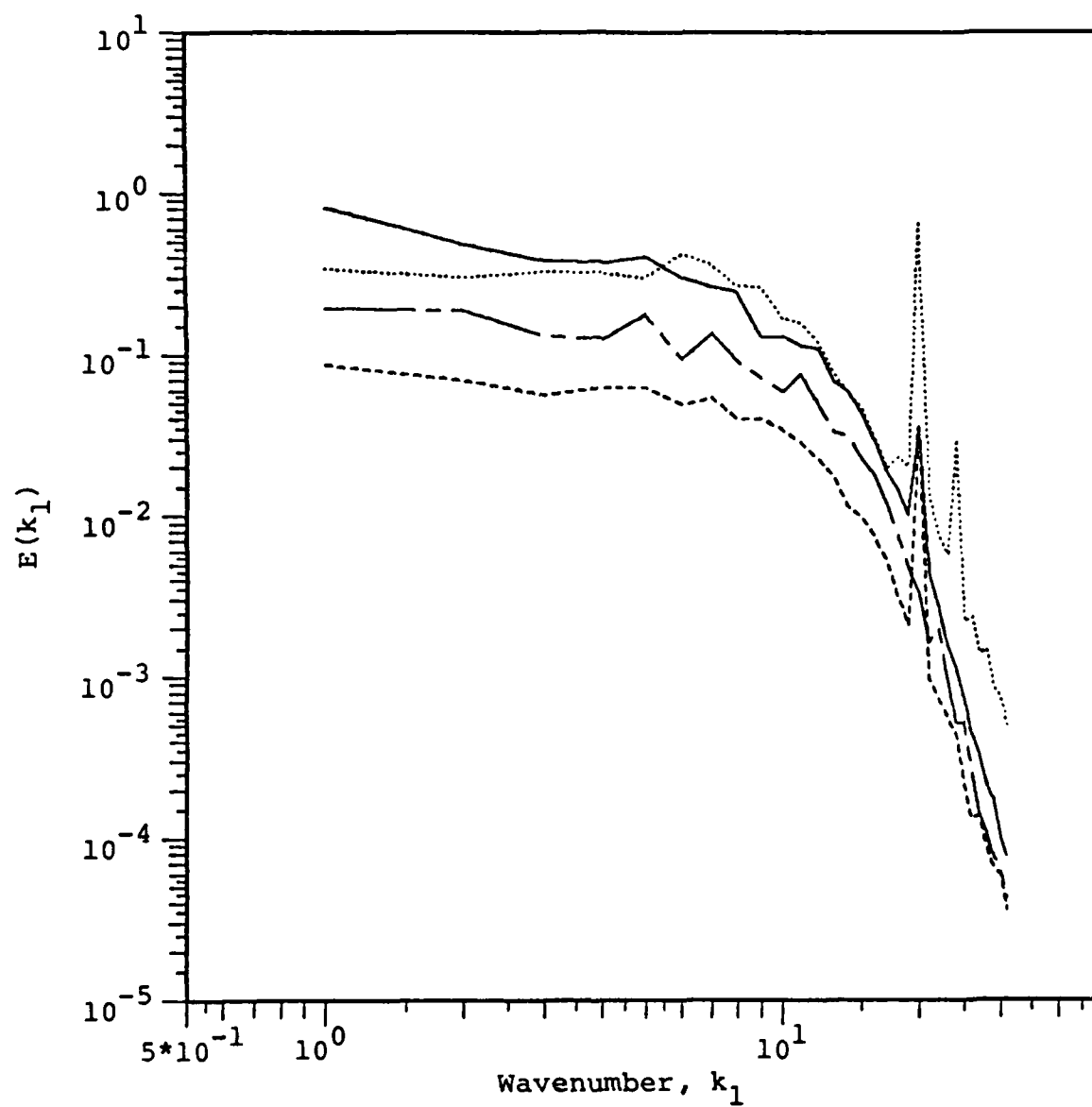
Figure 14.- Streamwise two-point correlation function for a channel with prescribed motion on one wall (Case 1).





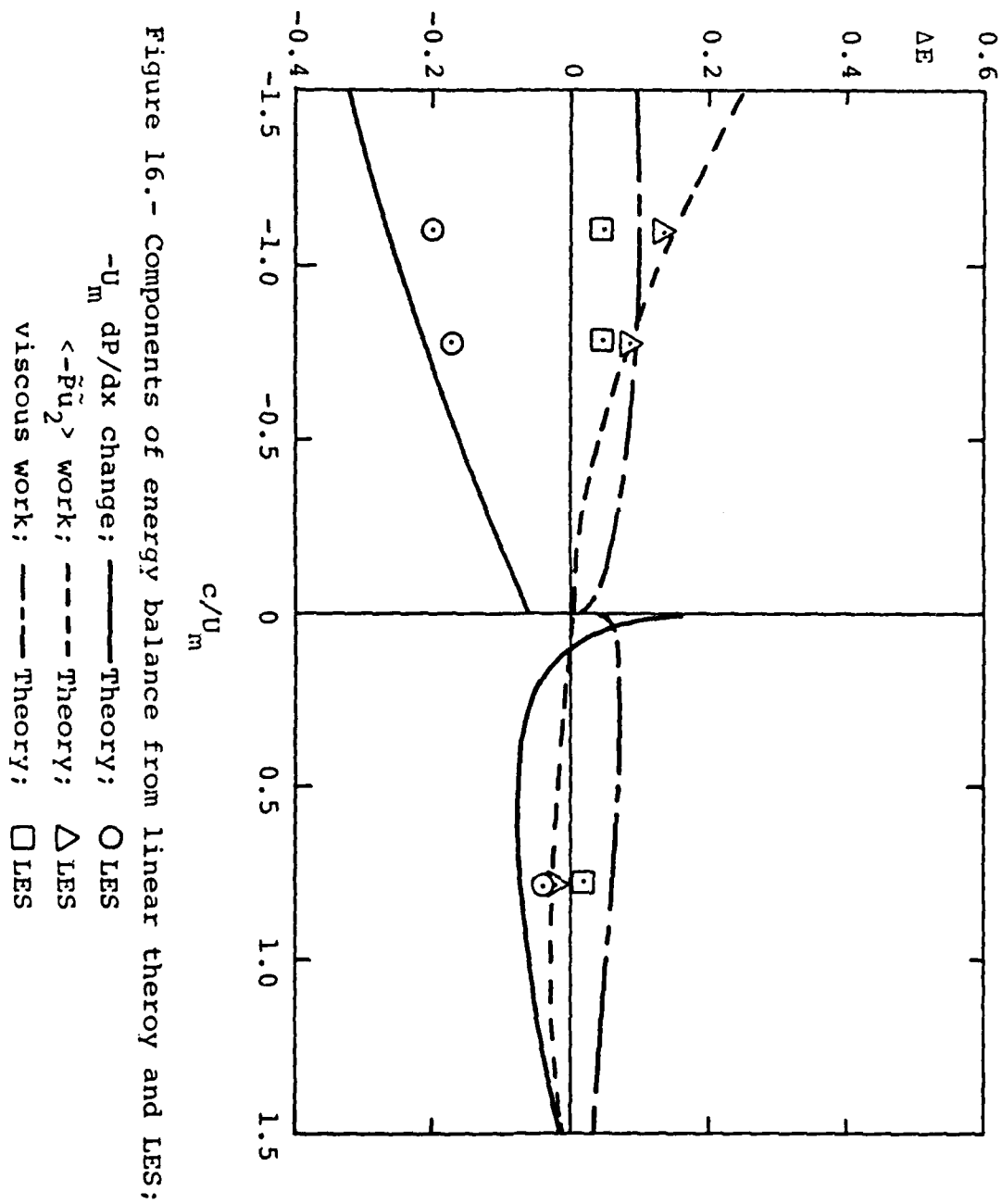
(a)  $y_w^+ \approx 55$  measured from the rigid wall ( $x_2 = - .914$ )

Figure 15.- Streamwise energy spectra for a channel with prescribed motion on one wall (Case 1).



(b)  $y_w^+ = 55$  measured from the moving wall ( $x_2 = -.914$ )

Figure 15.- Continued.



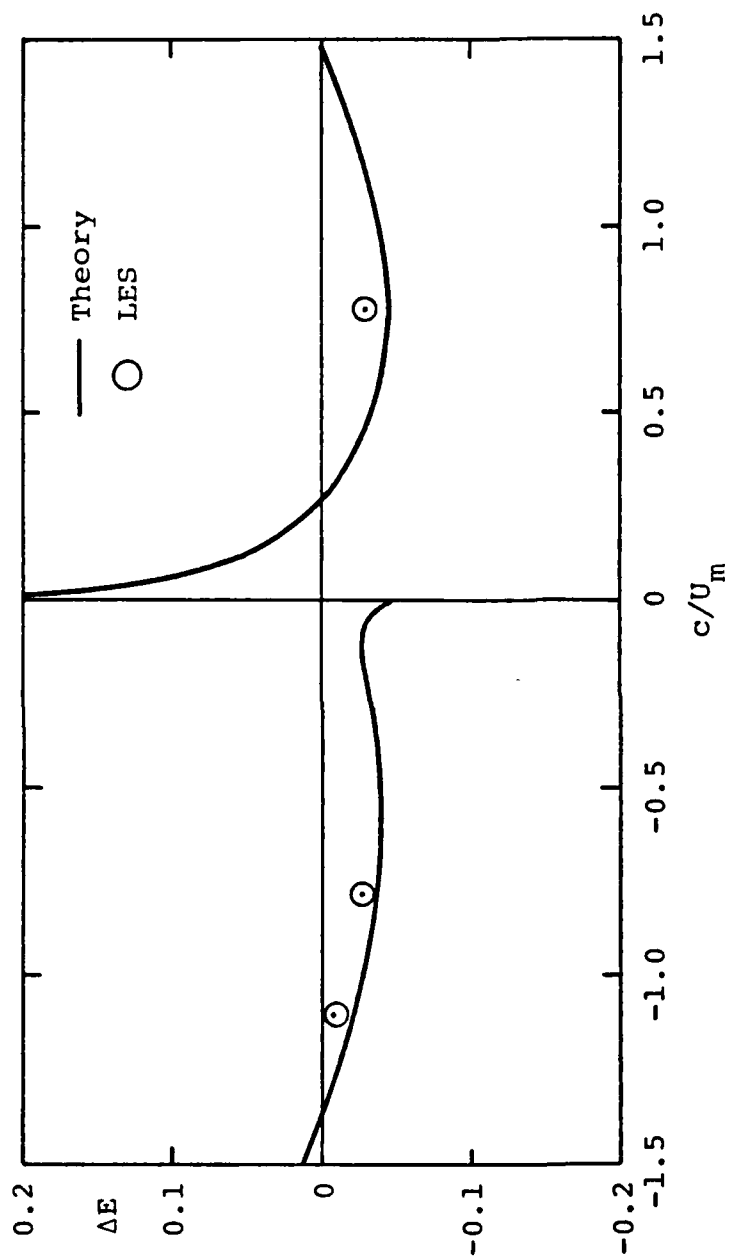
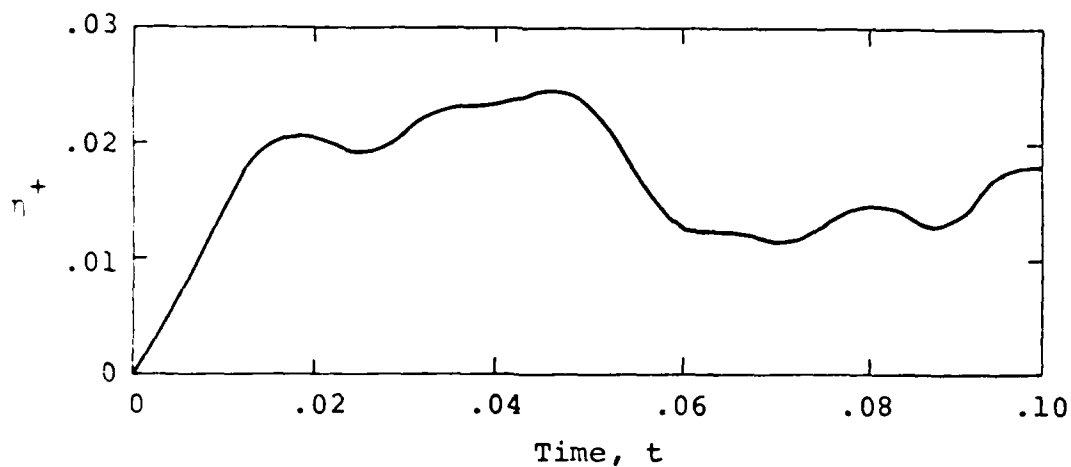
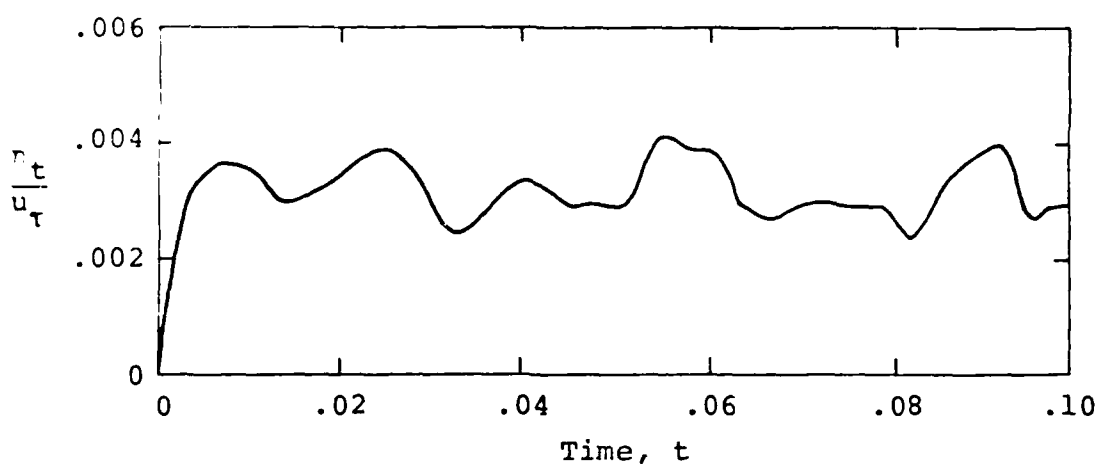


Figure 17.- Net change in energy required to drive flow through channel in response to Stokes layer from linear theory and LES.



(a) rms wall deflection,  $\eta^+$



(b) rms wall velocity  $\eta_t/u_\tau$

Figure 18.- Time history of rms wall deflection and rms wall velocity for first compliant wall calculation.

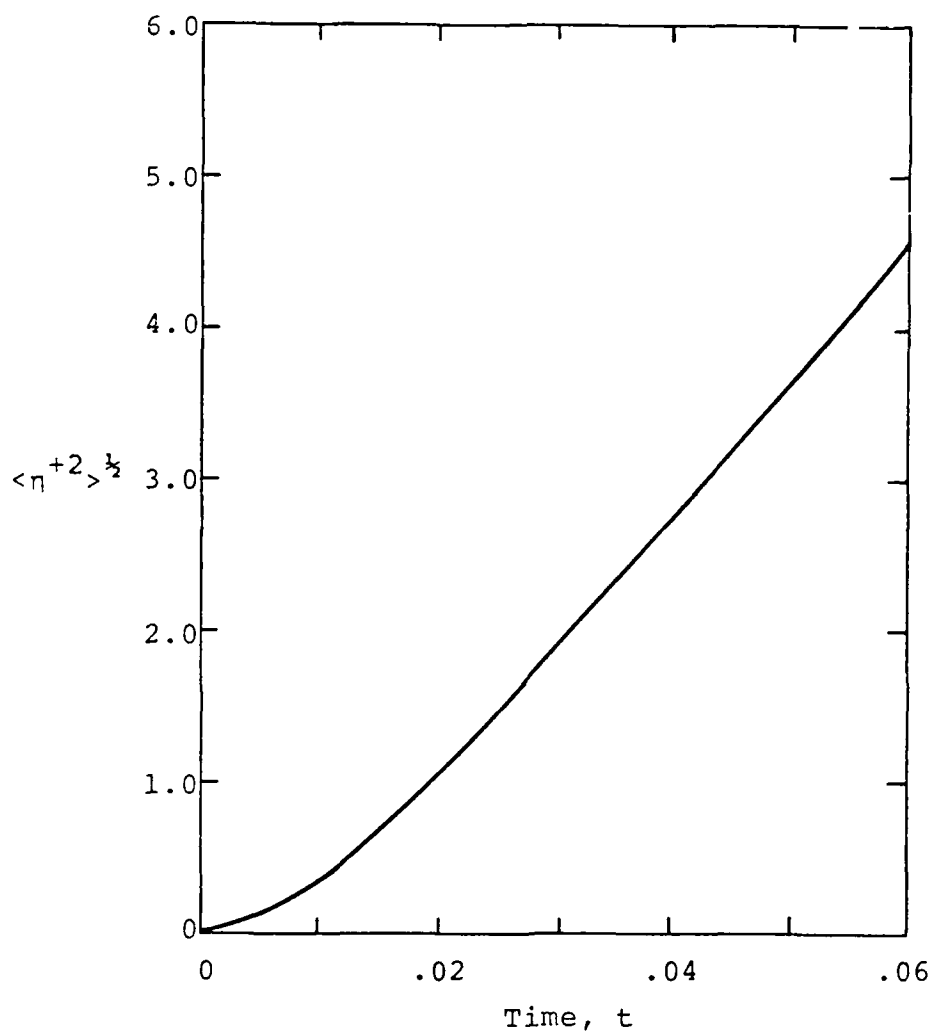


Figure 19.- Time history of rms wall deflection for membrane with tension;  $\bar{N}_x = \bar{N}_z = 10$  (Case 3, Table 4).

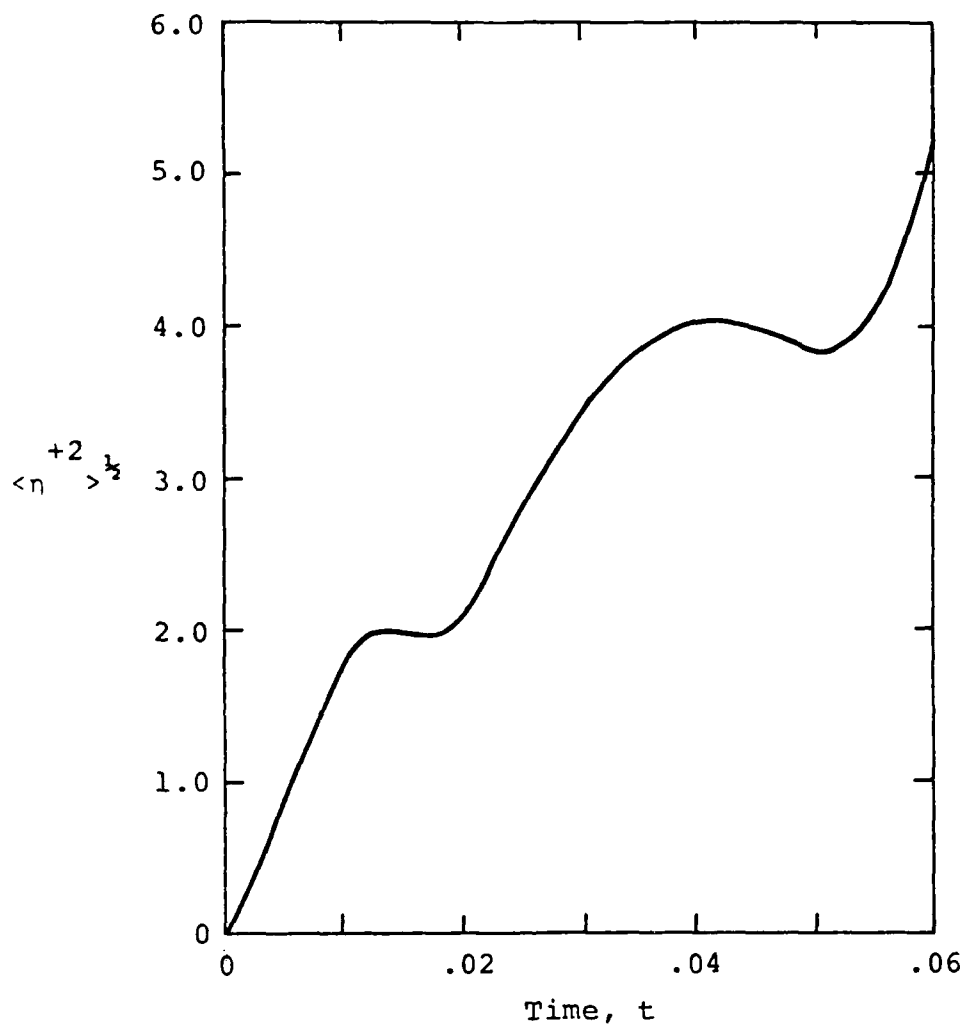


Figure 20.- Time history of rms wall deflection for a membrane with tension;  $\bar{N}_x = \bar{N}_z = 100$  (Case 4, Table 4).

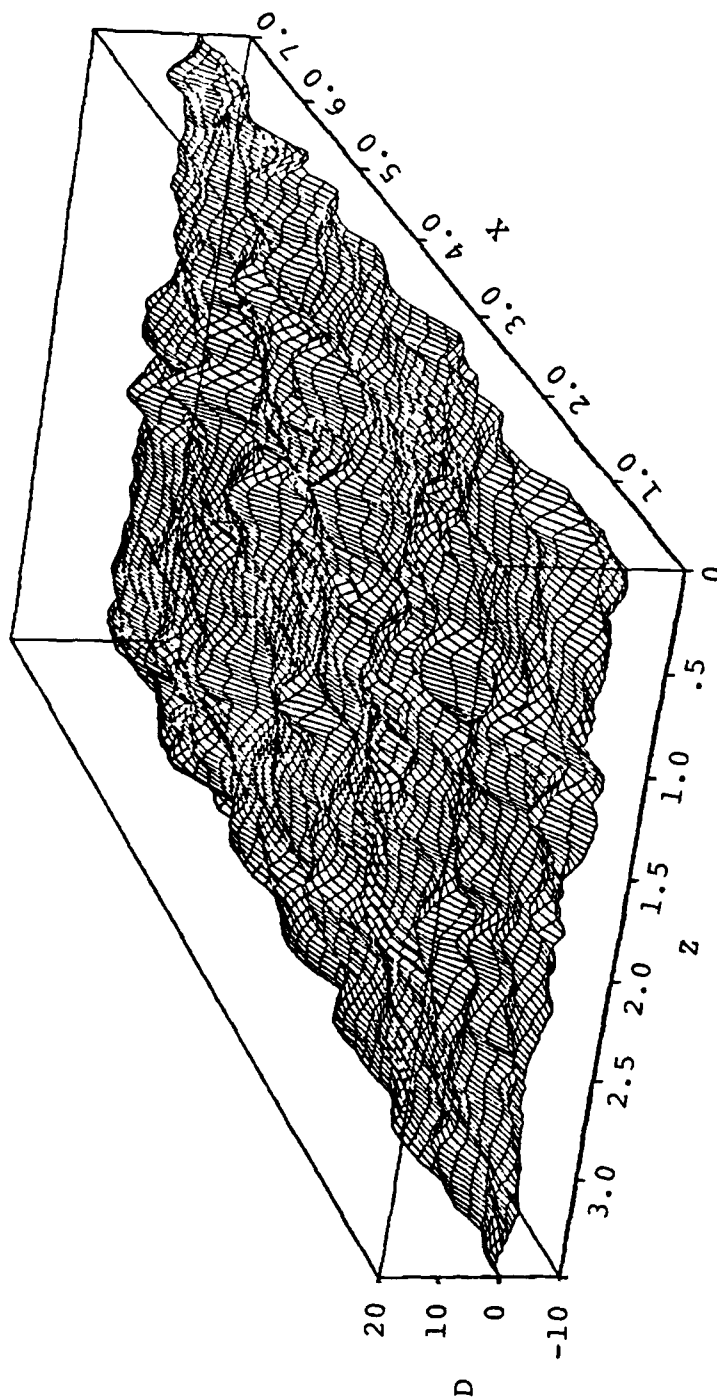


Figure 21.- Plot of typical distribution of pressure fluctuations on a compliant wall.



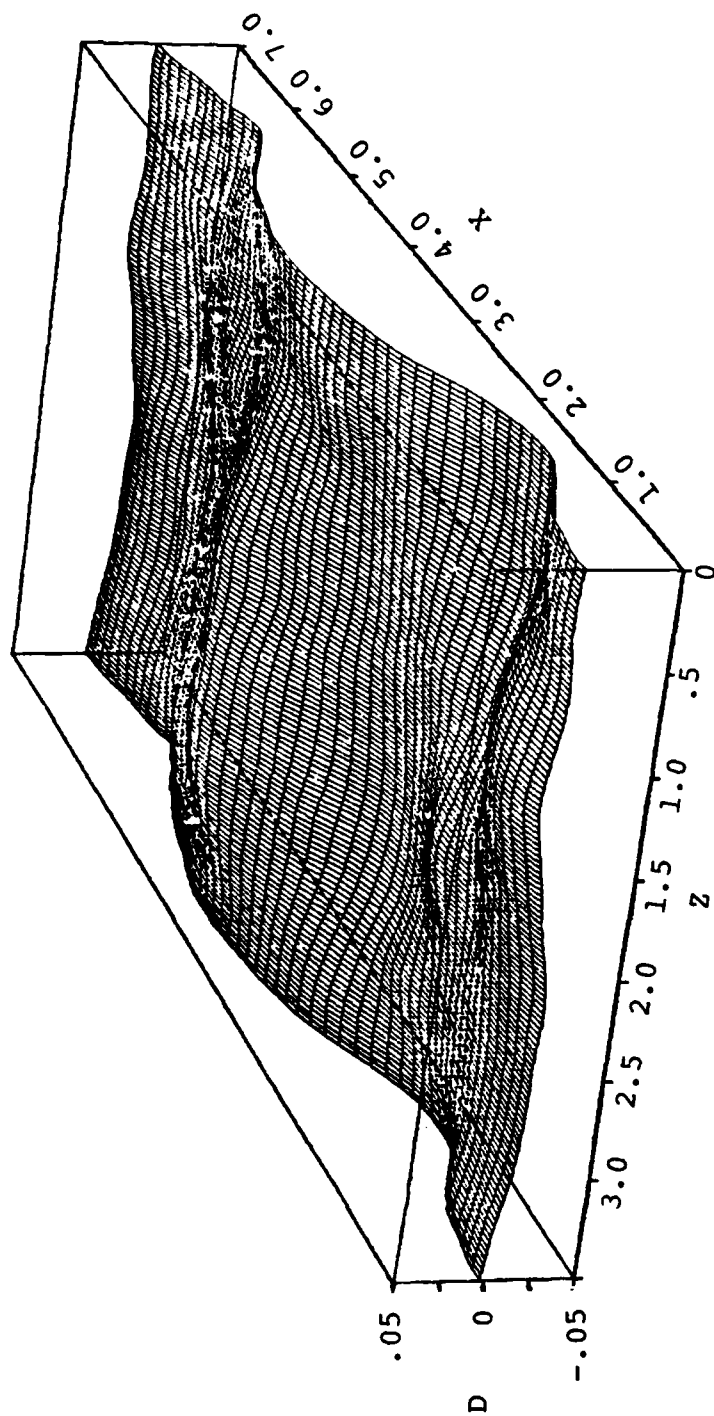


Figure 22.- Plot of wall shape for Yang and Heller compliant wall.

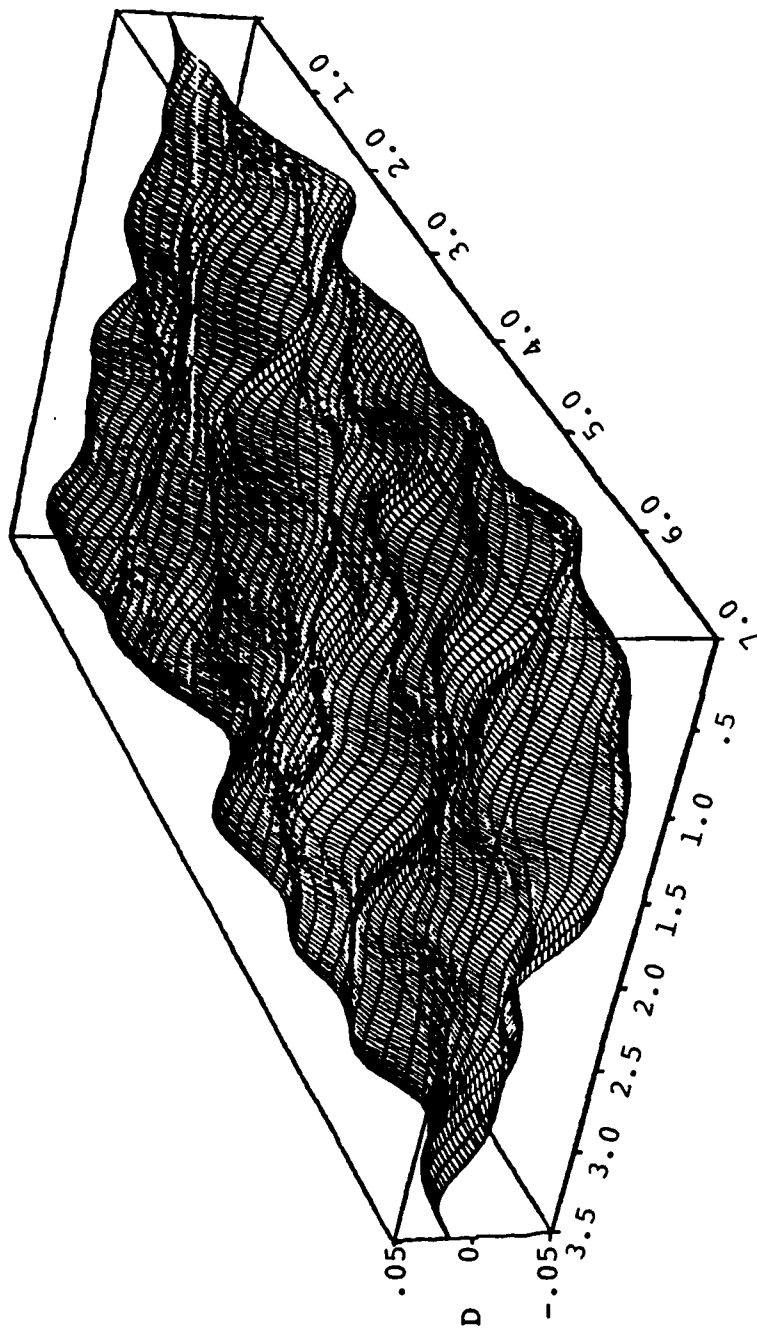
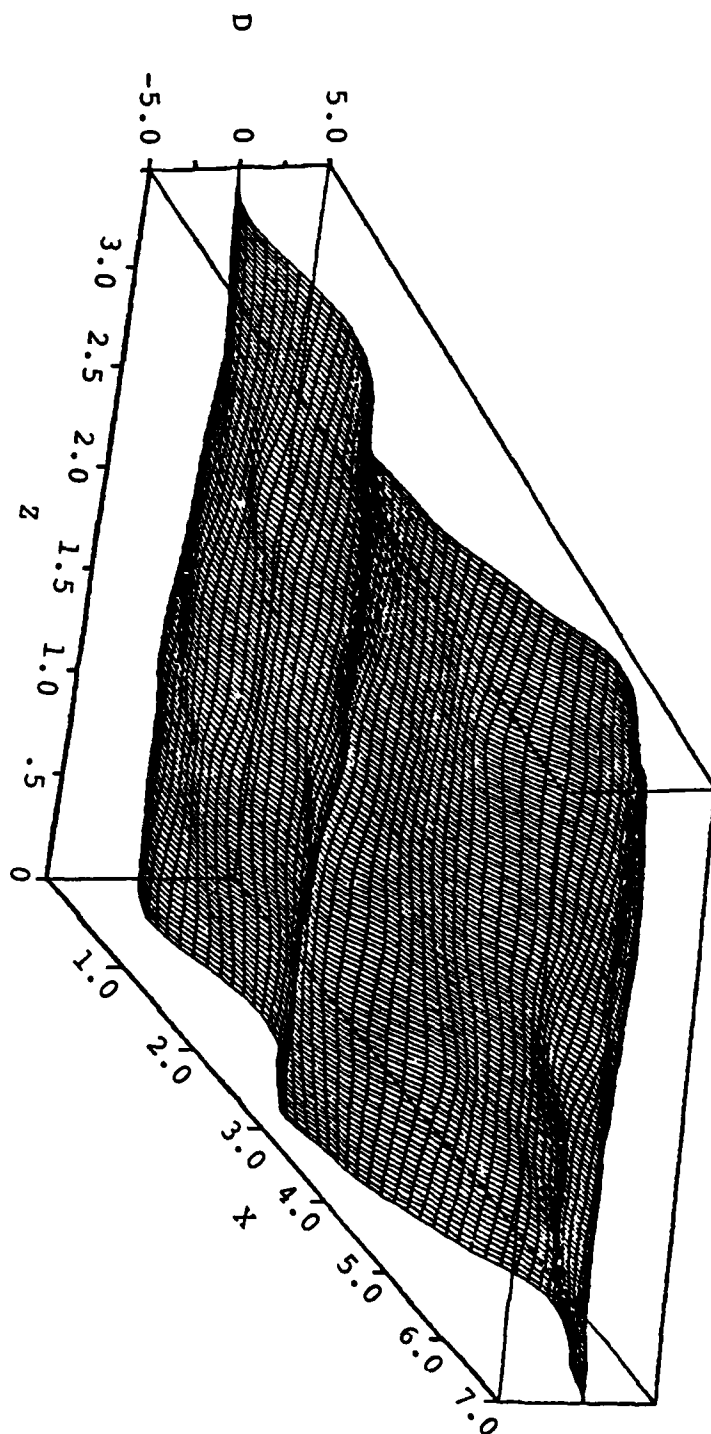
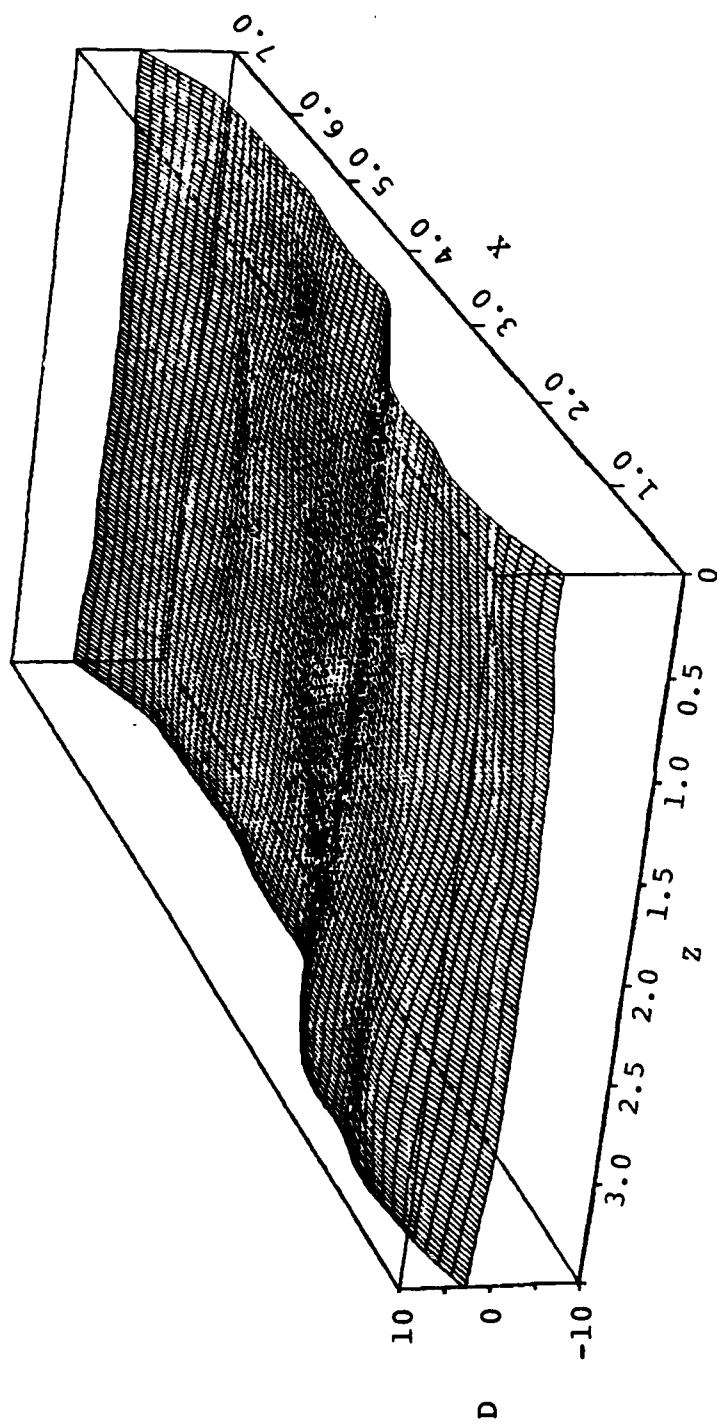


Figure 23.- Plot of wall shape for Yang and Heller compliant wall with viscoelastic damping and membrane tension omitted.



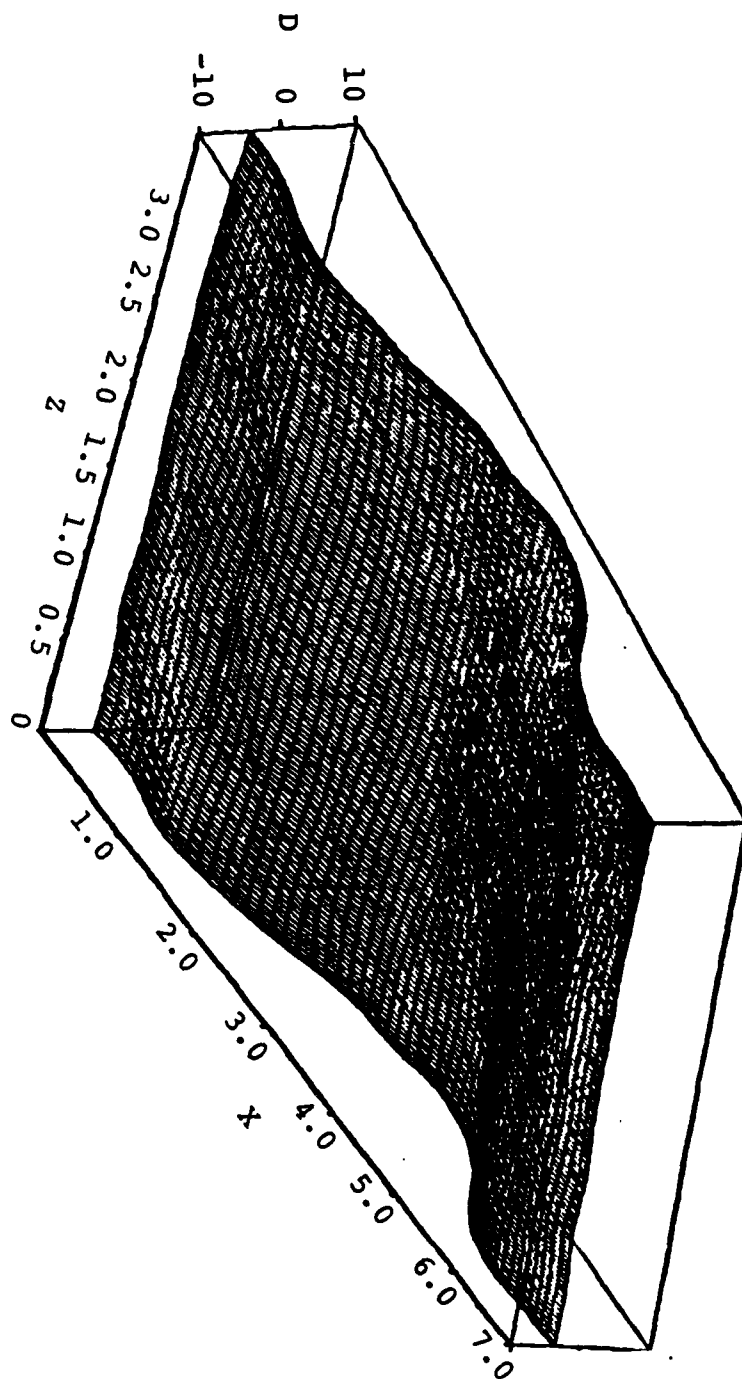
(a)  $t = .1928$

Figure 24.- Plots of wall shape for a compliant membrane with  $N_x = N_z = 100$ .



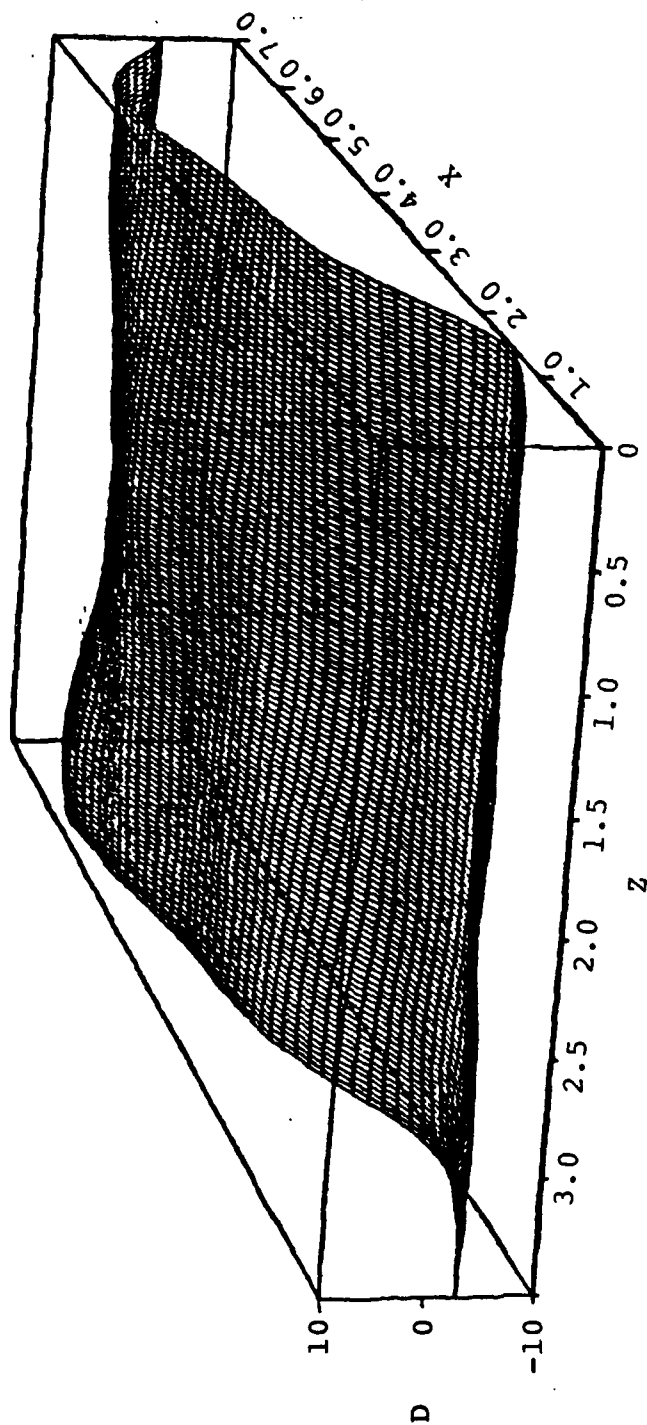
(b)  $t = .3214$

Figure 24.- Continued.



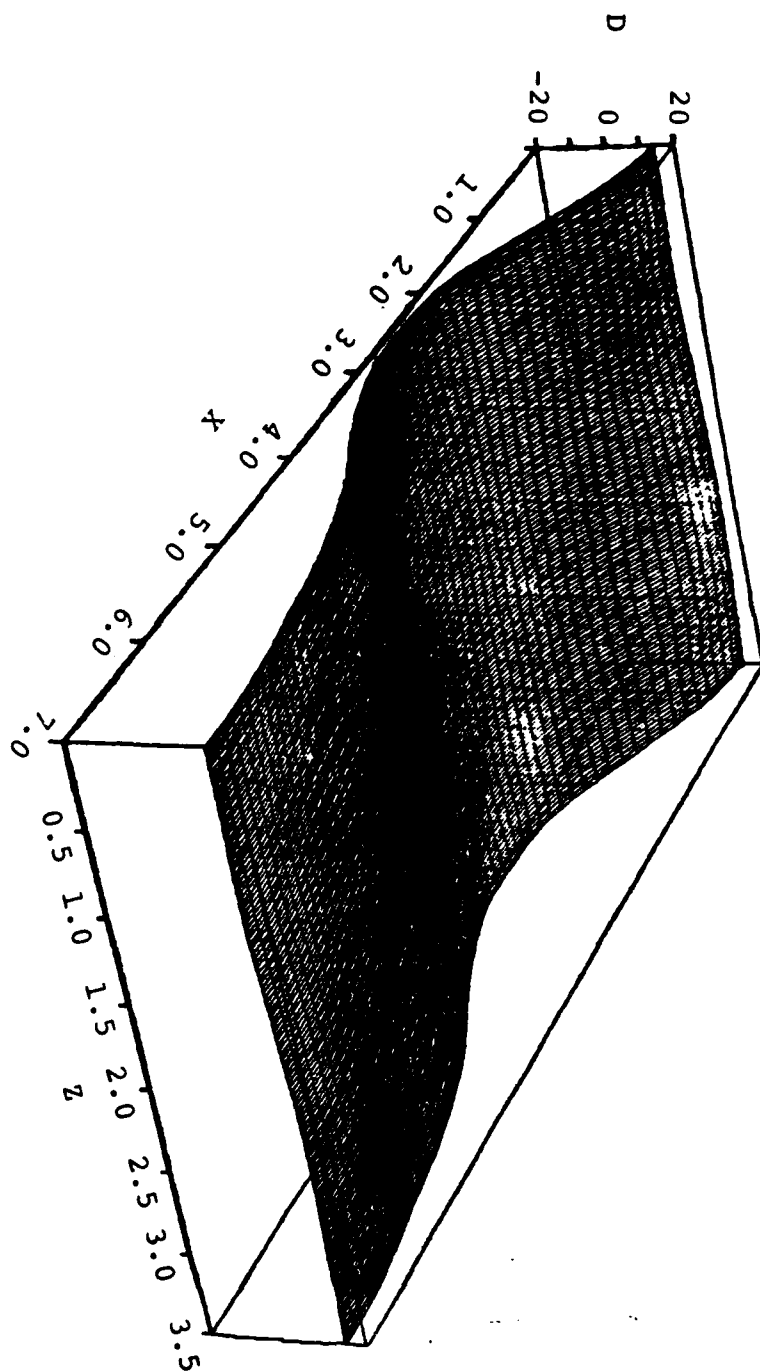
(c)  $t = .45$

Figure 24.- Continued.



(d)  $t = .611$

Figure 24.- Continued.



(e)  $t = .707$

Figure 24.- Concluded.

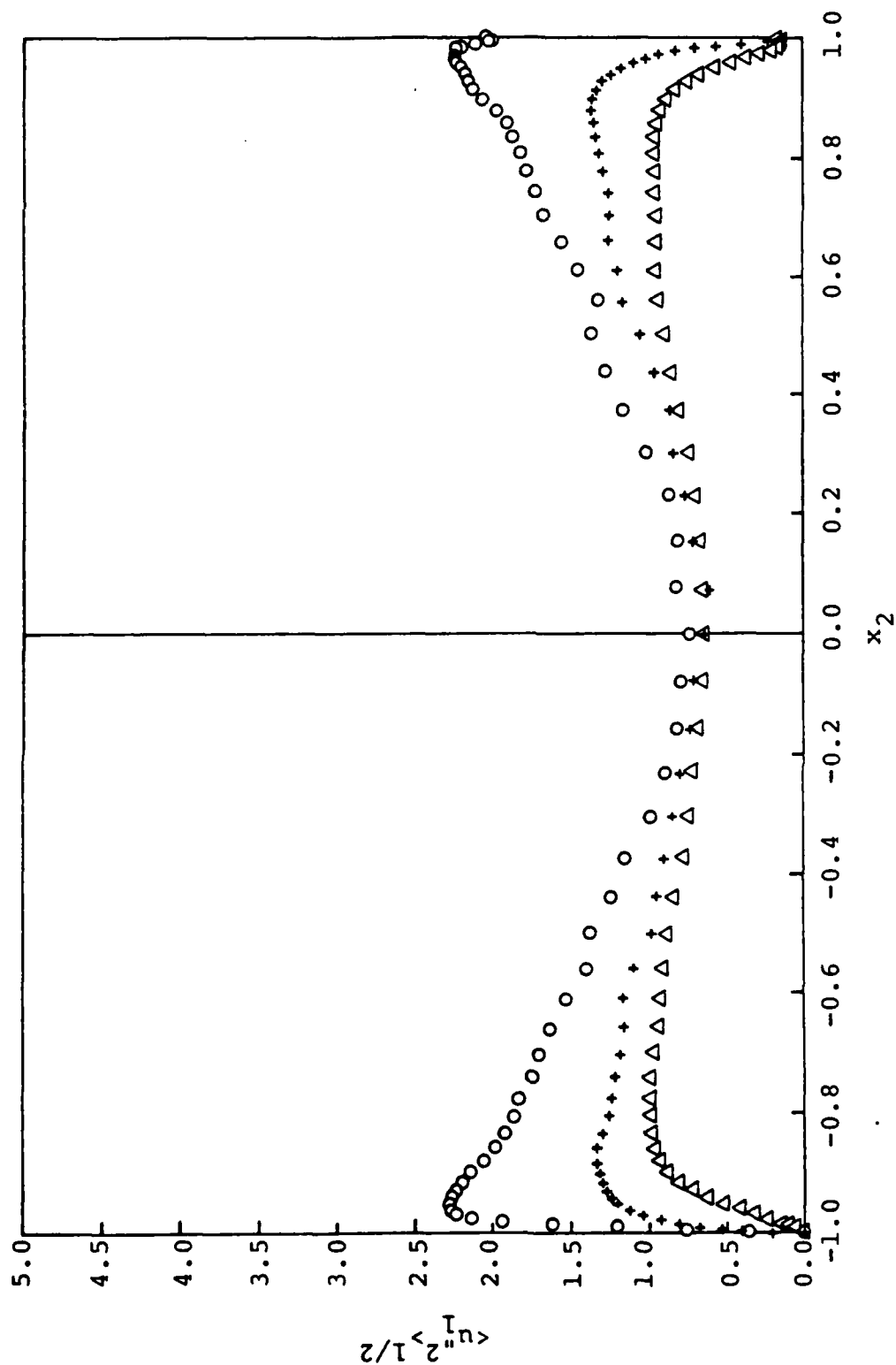


Figure 25.- Turbulence intensities in a channel  
with one compliant wall.



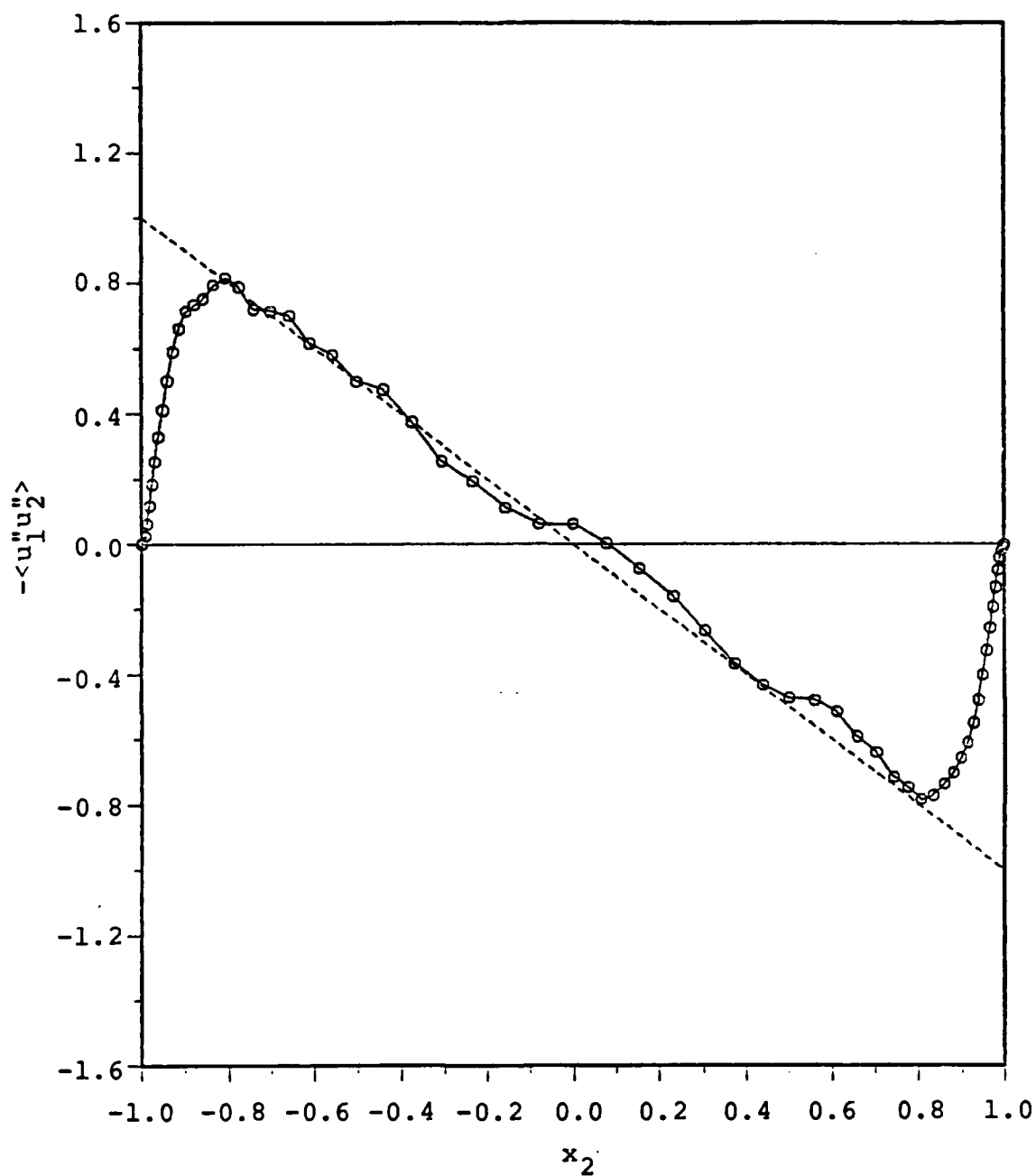
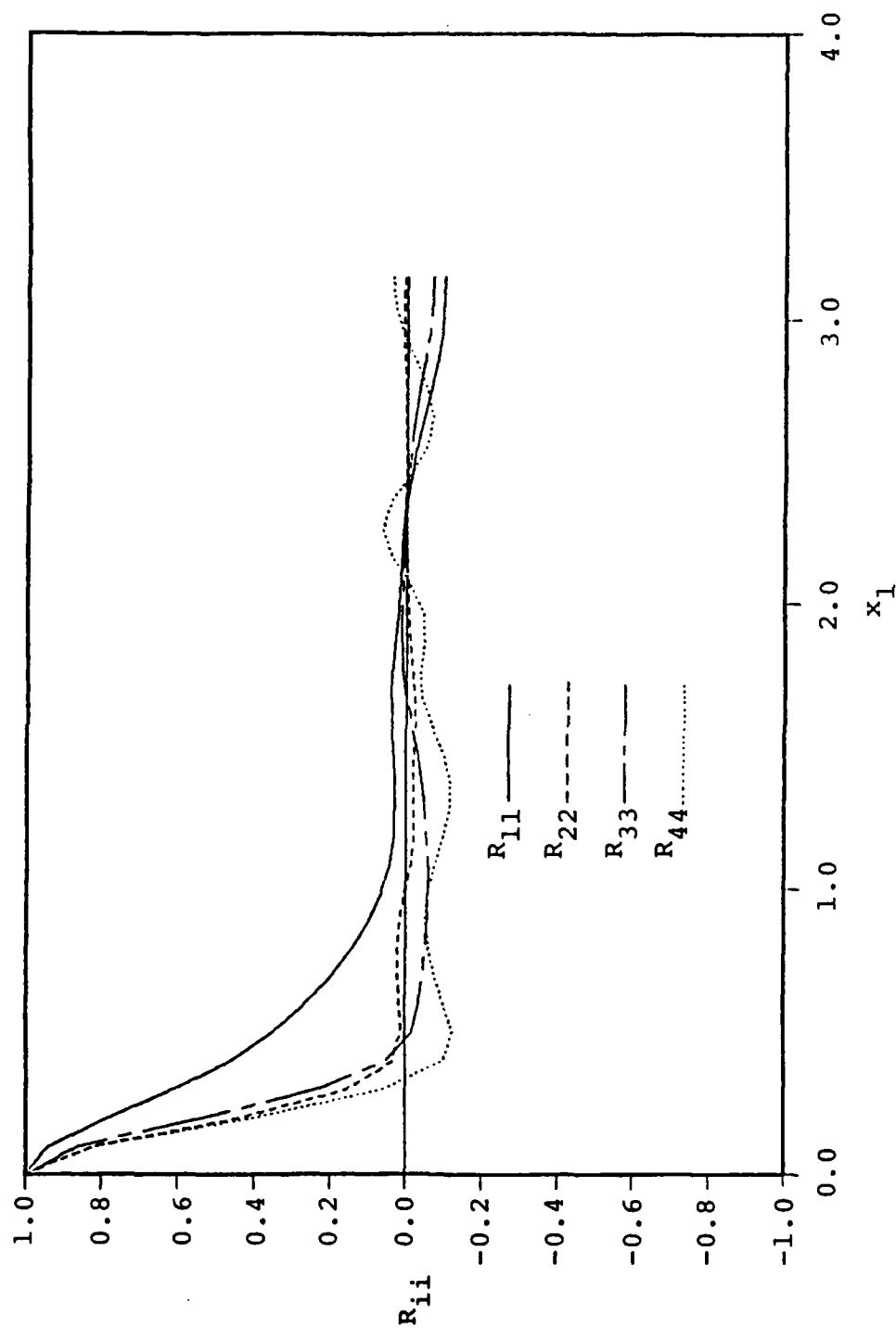
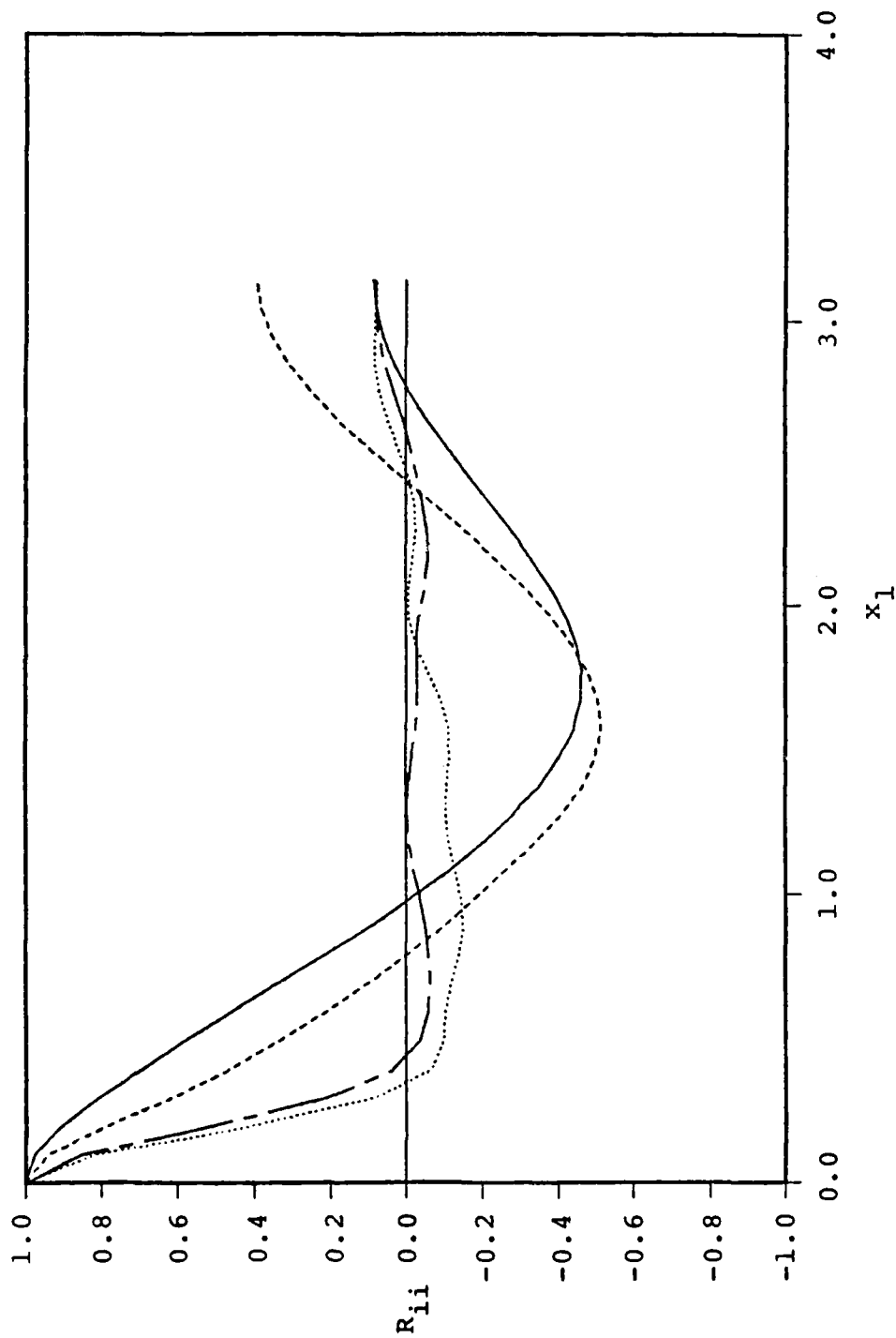


Figure 26.- Turbulent shear stress distribution in a channel with one wall compliant.



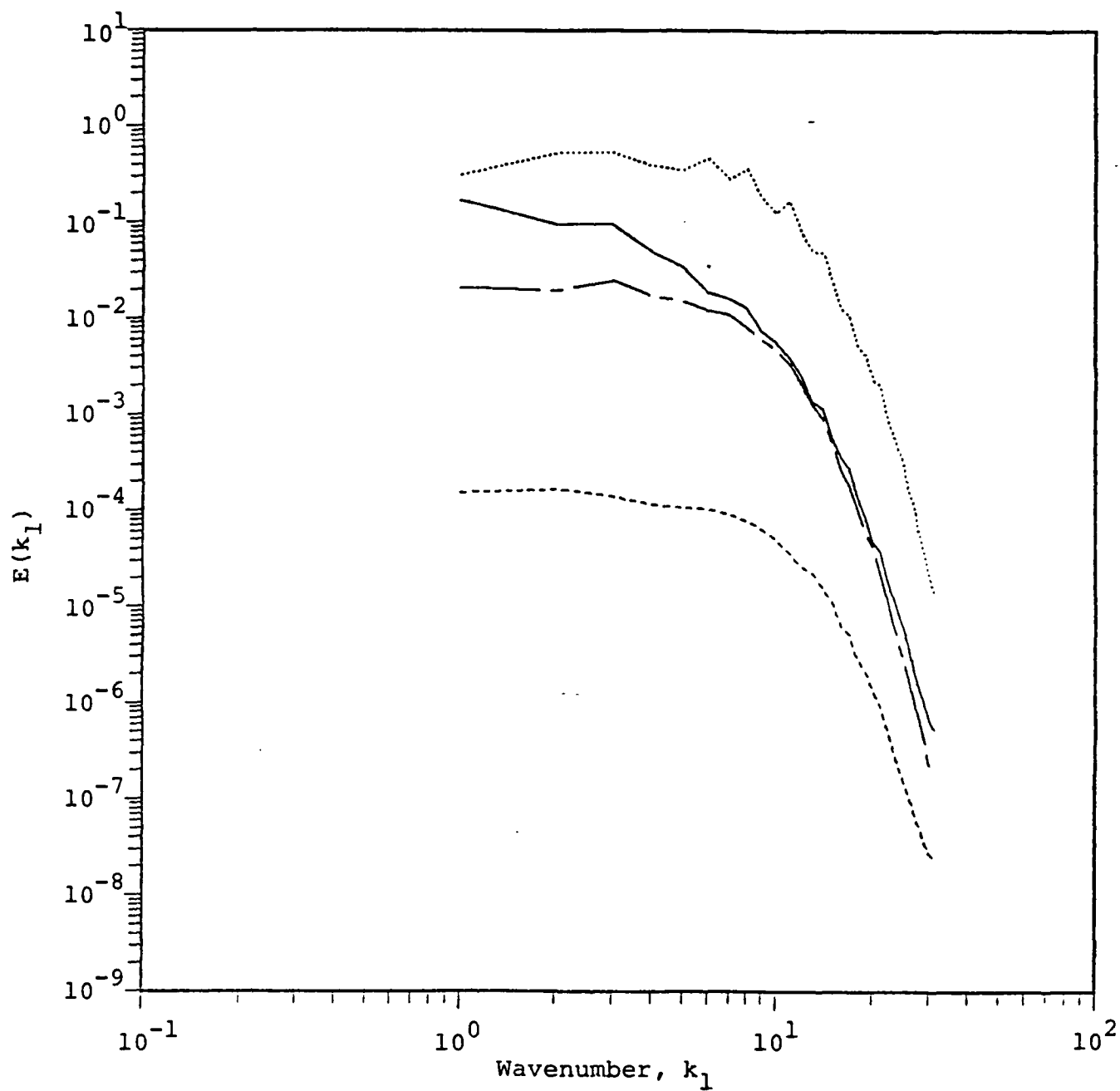
(a)  $Y_w^+ \approx 6.26$  measured from the rigid wall ( $x_2 = -.990$ )

Figure 27.- Streamwise two-point correlation functions in a channel with one wall compliant.



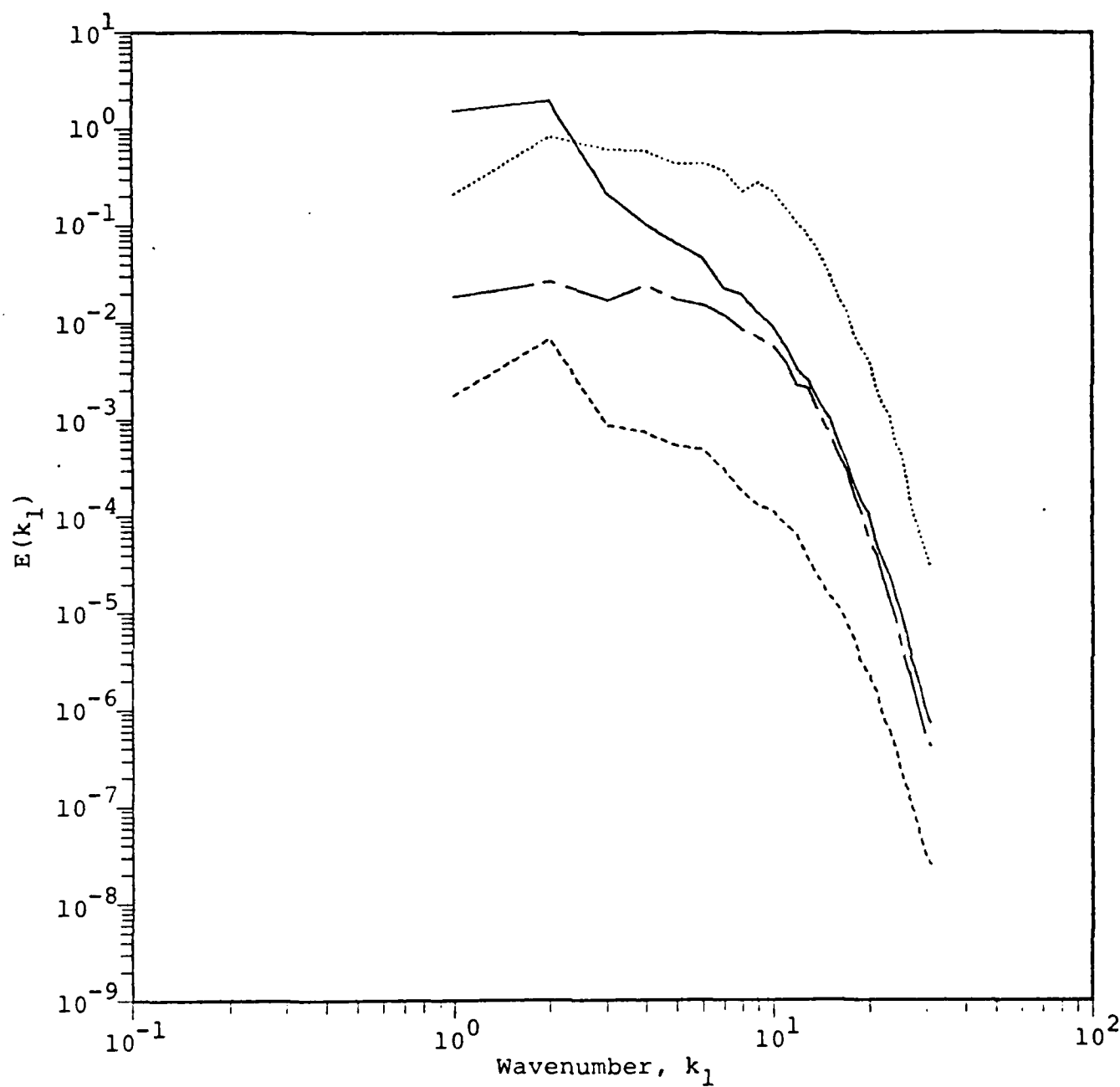
(b)  $y_w^+ \approx 6.26$  measured from the compliant wall ( $x_2 = +.990$ )

Figure 27.- Concluded.



(a)  $y_w^+ \approx 6.26$  measured from the rigid wall ( $x_2 = -.990$ )

Figure 28.- Streamwise energy spectra in a channel with one wall compliant.



(b)  $y_w^+ \approx 6.26$  measured from the compliant wall ( $x_2 = +.990$ )

Figure 28.- Concluded.

**END**

**FILMED**

**2-85**

**DTIC**